7-2015

Static and Dynamical Properties of Ferroelectrics and Related Material in Bulk and Nanostructure Forms

Zhigang Gui
University of Arkansas, Fayetteville

Static and Dynamical Properties of Ferroelectrics and Related Materials in Bulk and Nanostructure Forms

A dissertation submitted in partial fulfillment of
of the requirements for the degree of
Doctor of Philosophy in Physics

by

Zhigang Gui
University of Science and Technology of China
Bachelor of Science in Physics, 2009

July 2015
University of Arkansas

This thesis is approved for recommendation to the Graduate Council.

Professor Laurent Bellaiche
Thesis Director

Professor Huaxiang Fu
Committee Member

Professor Gregory Salamo
Committee Member

Professor Douglas Spearot
Committee Member

Professor Surendra Singh
Committee Member

Abstract

Ferroelectrics (FE) and multiferroics (MFE) have attracted a lot of attentions due to their rich and novel properties. Studies towards FE and MFE are of both fundamental and technological importance. We use a first-principles-based effective Hamiltonian method, conventional *ab-initio* packages and linear-scale three-dimension fragment method to investigate several important issues about FE and MFE.

Tuning the properties of FE and MFE films are essential for miniaturized device applications, which can be realized through epitaxial strain and growth direction. In this dissertation, we use the effective Hamiltonian method to study (i) $BaTiO_3$ films grown along the (110) pseudocubic direction on various substrates, (ii) $BaTiO_3$ films grown on a single substrate along directions varying from [001] to [110] via [111] pseudocubic direction. Optimized physical responses or curie temperatures are found along some special directions or under epitaxial strain of certain range. FE and MFE nanostructures are shown to possess electrical vortices (known as one type topological defect), which have the potential to be used in new memory devices. However, the dynamic mechanism behind them is barely known. We use the effective Hamiltonian method to reveal that there exists a distinct mode which is shown to be responsible for the formation of the electrical vortices and in the THz region.

Spin-canted magnetic structures are commonly seen in MFE, which results in the coexistence of two or more magnetic order parameters in the same structure. Understanding the physics behind such coupled magnetic order parameters is of obvious benefit for the sake of control of the magnetic properties of such systems. We employ both the effective Hamiltonian and *ab-initio* methods to derive and prove there is a universal law that explicitly correlates various magnetic order parameters with the different types of oxygen octahedra rotations.

FE or MFE possessing electrical vortices are experimentally shown to have a much lower critical voltage in current-voltage curves. However, the exact underlying reason is unknown. In this dissertation, we take the advantage of the effective Hamiltonian method and linear-scale three-dimension fragment method to study the electronic properties of electrical vortices. Such combined procedure clearly shows the existence of electrical vortices doesn't decrease the band gap, but increases it instead, which suggests the lower critical voltage in current-voltage curves

is likely to result from the defects inside the vortices.

Contents

Acknowledgements

Going through the whole graduate study has been a wonderful and unique experience for me, from which I have benefited a lot and will certainly be very helpful for my future career. I have been very fortunate to conduct my graduate study here in University of Arkansas. The completion of my doctoral degree would not happen without the participation of a few knowledgeable persons. First, I'd like to greatly thank my advisor Dr. Laurent Bellaiche who has been giving tremendous illuminating guides and professional advices during these years. I have always been inspired by his constant flow of good ideas and enlightened by his rigorous and prudent attitude toward science. Additionally, what I have admired and been learning is how he manages to work extraordinarily efficiently. Particularly, I am truly grateful that he always hands over a good solution whenever I turn to him for help. This dissertation could not be done without his guide. Next, I'd like to thank the other members of my thesis committee, Dr. Fu, Dr. Salamo, Dr. Spearot and Dr. Singh, especially for their precious time that they spare out of their busy schedules to read this dissertation and offer valuable advices. I'd also like to express my sincere gratitude to the present and previous members of our group who all have helped me a lot when I started doing research. It is my privilege to work with and learn from them. And there are many others to whom I'd like to extend my gratitude for their kind help. In the end, I'd like very much to thank my wife, my brother and my parents for their absolute supports along the way.

Dedication

Dedicated to my family.

Citations to Previously Published Work

Large parts of Chapters 3 have appeared in the following two papers:

> Reprinted permission from "Properties of epitaxial (110) BaTiO_3 films from first principles", Zhigang Gui, S. Prosandeev, and L. Bellaiche, *Phys. Rev. B* **84**, 214112 (2011), DOI: 10.1103/PhysRevB.84.214112. Copyright 2011 American Physical Society;
> Reprinted permission from "Tuning and optimizing properties of ferroelectric films grown on a single substrate: A first-principles-based study", Zhigang Gui and L. Bellaiche, *Phys. Rev. B* **91**, 020102(R) (2015), DOI: 10.1103/PhysRevB.91.020102. Copyright 2015 American Physical Society.

Large parts of Chapters 4 have appeared in the following paper:

> Reprinted permission from "Terahertz dynamics of ferroelectric vortices from first principles", Zhigang Gui and L. Bellaiche, *Phys. Rev. B* **89**, 064303 (2014), DOI: 10.1103/PhysRevB.89.064303. Copyright 2014 American Physical Society.

Large parts of Chapter 5 have appeared in the following paper:

> Reprinted permission from "A simple law governing coupled magnetic orders in perovskites", L Bellaiche, Zhigang Gui and Igor A Kornev, *J. Phys.: Condens. Matter* **24**, 312201 (2012), Fast Tract Communication, online at stacks.iop.org/JPhysCM/24/312201. Copyright 2012 Institute of Physics Publishing.

Finally, Chapter 6 appears entirely in the following paper:

> Reprinted permission from "Electronic properties of electrical vortices in ferroelectric nanocomposites from large-scale ab-initio computations", Zhigang Gui, Lin-Wang Wang and L. Bellaiche, submitted to *Nano Letters*. Copyright 2015 American Chemical Society.

Chapter 1

Introduction and summary

Introduction

Ferroelectrics (FE) and multiferroics (MFE) form a large and important class of materials in condensed matter,and are well characterized by some electrical and magnetic order parameters. The existence of electrical and/or magnetical degrees of freedom renders such systems capable of exhibiting rich physical phenomena, ranging from various phases of different electrical and magnetical dipole configurations to substantial magnetoelectric and electro-optic responses. Additionally, the couplings between these degrees of freedom and other structural degrees of freedom lead to many various applications of FE and MFE, such as piezoelectric devices, transducers and sonar devices [1, 2]. Therefore, study towards FE and MFE is of both fundamental and technological importance.

For miniaturized device applications, it is essential to understand FE films under the epitaxial strain arising from the mismatch of lattice constant between the films and the substrate. Because of the couplings between the epitaxial strain and other degrees of freedom such as polarization, epitaxial strain is one of the most efficient ways of FE films' engineering. Conventionally, only films grown along the [001] pseudocubic direction are considered. As a result, the broad effects of growth directions on properties of ferroelectric films remain basically unexplored, but could play as another way of tuning the properties of FE films. As detailed in Chapter 3, $BaTiO_3$ films grown along the [110] pseudocubic direction demonstrate several interesting features that are absent in (001) films. Moreover, there is an inevitable limitation to the magnitude and sign of the epitaxial strain that ferroelectric films can experience due to the fact that there are rather few available substrates. Additionally, some of these substrates are rather

expensive and/or induce high defects' density within the films, which therefore further limit their technological usefulness. One alternative way to overcome such obstacles may be to grow ferroelectric films on a single, amply available and economic substrate (such as $SrTiO_3$), but vary the crystallographic direction (away from the pseudo-cubic [001] direction) of the growth axis. As shown in Chapter 3, this alternative procedure has more advantages than conventional (001) films.

FE and MFE nanostructures are experimentally observed to display dipole configurations of vortex shape which is known as one type of topological defects. FE and MFE films displaying electrical vortices have the potential to be used in new memory devices since they are smaller in volume and probably faster in speed than magnetic vortices. As a result, understanding the dynamical mechanism behind electrical vortices is the crucial first step. In Chapter 4, we use a first-principles-based effective Hamiltonian method to reveal that there exists a distinct mode which is shown to be responsible for the formation of the electrical vortices and in the THz region. Not only the dynamical properties but also the electronic properties of electrical vortices are of great interest. A recent experimental measurement reported that the current–*versus*-voltage (I-V) curve starts to be significant for a voltage of about 1 V in $BiFeO_3$ (BFO) thin films having artificially-created electrical vortices, that is about 2 V lower than the corresponding critical voltage in BFO systems having no topological defect. One important and currently unknown issue to resolve is to determine if such reduction in critical voltage and resulting significant electrical current measured between 1 and 2 V are intrinsic (i.e., if they are associated with a remarkable reduction of the electronic band gap) or are rather extrinsic in nature (e.g., if they are due to the existence of vacancies near the topological defects). As detailed in Chapter 6, we developed and applied a new large-scale *ab-initio* procedure to a nanocomposite made of $BaTiO_3$ (BTO) nanowires inserted in a matrix formed by $SrTiO_3$ (STO). This original numerical procedure consists in combining the effective Hamiltonian technique with the linear-scaling three-dimensional fragment method (that was initially developed for for semiconductor systems), which is able to resolve aforementioned questions.

In MFE, spin-canted structures are commonly seen, which results in the coexistence of two or more magnetic order parameters in the same structure. Understanding the physics behind

such coupled magnetic order parameters is of obvious benefit for the sake of control of the magnetic properties of such systems, since it can dramatically affect magnetic properties and even leads to the occurrence of the so-much-desired magneto-electric effects. Well-known examples of such coexistence are the R3c or Cc states of $BiFeO_3$ (BFO) thin films and bulks that exhibit a spin-canted magnetic structure – which generates a weak ferromagnetic (FM) moment (also known as a F-type magnetic ordering) superimposed on a predominant G-type antiferromagnetic (AFM) vector. This corresponds to a combination of two coupled magnetic order parameters and is receiving a lot of attention from the scientific community. Other examples are the three coupled magnetic orders (to be chosen among the F-, G-, C- and A-types) recently found in the Pnma phase of many magnetic or multiferroic perovskites. We employ both first-principles-based effective Hamiltonian and *ab-initio* methods to derive and prove that there is a universal law that explicitly correlates various magnetic order parameters with the different types of oxygen octahedral rotations.

Structure of this thesis

The main body of this thesis naturally divides itself into five parts, which are fairly independent:

- Methodology (Chapter 2),
- Finite-temperature static properties of $\mathbf{BaTiO_3}$ epitaxial films (Chapter 3),
- Finite-temperature dynamical properties of $\mathbf{(Ba, Sr)TiO_3}$ nanocomposites (Chapter 4),
- A universal law governing coupled magnetic orders in ABO_3 perovskites (Chapter 5), and
- Electronic properties of ferroelectric vortices from large-scale *ab-initio* computations (Chapter 6).

The first part gives detailed introduction of methodologies that will be used in the studies of the later chapters: effective Hamiltonian and density functional theory. The second part presents the detailed studies of static properties (such as structural phase transitions and physical responses) of ferroelectric films under epitaxial strain mainly by the effective Hamiltonian

approach. The third part explores the dynamics of ferroelectric nanocomposites by the effective Hamiltonian approach. The fourth part is devoted to coupled magnetic orders in perovskite multiferroelectrics by analytical derivations and density functional theory approach. The fifth part deals with the electronic properties of electric vortices in ferroelectric nanocomposites. The subject matters and objectives of the five parts are sufficiently different to merit individual introductions and summaries, which are now presented through chapters without further ado.

Chapter 2

Methodology

Effective Hamiltonian

The effective Hamiltonian method used here has been established for two decades [3]. Such effective Hamiltonian possesses several advantages that generally fall into the following aspects: (1) by decomposition of energetic contributions of such Hamiltonian, it provides a broad picture from microscopic views of the properties of investigated ferroelectric systems; (2) by combining such effective Hamiltonian with Monte Carlo (MC) Metropolis algorithm or molecular dynamics simulation, it models finite-temperature-dependent static or dynamical properties of ferroelectric systems; (3) by the great reduction of degrees of freedom used in effective Hamiltonian, it is capable of simulating large supercells, which is quite necessary in studying more complex structures and complicated phenomena. Over the years, effective Hamiltonians have been developed and extended to investigate varieties of ferroelectric and multiferroelectric systems [4, 5, 6], including bulk and nanostructure systems [7, 8, 9, 10].

ABO_3 perovskites have a common high-symmetry structure at high temperature as depicted in Figure 2.1. The existences of some phonons make this cubic phase unstable, which leads to low-symmetry structural phases as temperature drops. These phonons are often referred as *soft modes*, which are thus responsible for the rich varieties of structural phase transitions in this major type of ferroelectrics. For example, the arrows in Figure 2.1 indicate an unstable displacement pattern that corresponds to a well-known Γ_{15} phonon, which is the origin of ferroelectricity in typical $BaTiO_3$ and $PbTiO_3$. As it has been stated in the introduction, effective Hamiltonians are quite effective in simulating displacive phase transitions that involve a few unstable phonons, and ABO_3 perovskite ferroelectrics provide excellent examples that exhibit

varieties of displacive phases and other intriguing phenomena in condensed matter.

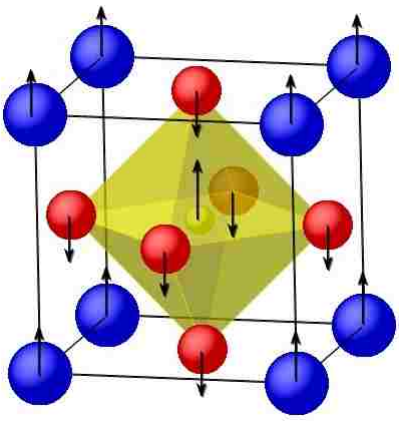

Figure 2.1: ABO_3 ferroelectrics: simple cubic structure with A atoms at corners, B atom (mostly from transition metals) at the body center and oxygen atoms occupying face centers. The arrows show the atomic displacement pattern of a typical Γ_{15} phonon of this structure.

In this thesis, a detailed description of the constituents of such Hamiltonian is given along with underlying physics. To reproduce time-dependent static properties of a system, it is necessary to reproduce the partition function which requires the unpractical full knowledge of internal energy landscape. One option is to approximate it. For this, the lowest energy state that weights most should be at least included in the Hamiltonian. Whether it is crucial or not to add contributions from other higher energy states should depend on the extent of consistency of the outputs. For the systems that are considered here, it is fairly sufficient for our simulating properties (as shown in later chapters) to enclose only the lowest energy state which is related to soft modes, for the investigated temperature window. For this thesis, we will talk about the case of $BaTiO_3$ which will be used in later chapters. To start, a reference structure is needed. The high-temperature cubic structure of Figure 2.1 is a natural choice in the sense that it is where the instability lies, and high symmetry will reduce a great deal of parameters in the energy term expansions. In this structure, five atoms are included. Thus, there are 3 acoustic and 12 optical phonon modes at any k point inside the first Brillouin Zone (BZ). The small displacements of these atoms will be expressed in a linear combination of these phonon modes. As mentioned above, here the most relevant mode is at the zone center (Γ point), the lowest-frequency triply degenerate transverse optical modes, Γ_{15}. The other important mode is the triply degenerate Γ_{15} acoustic mode which accounts for the shape of the unit cell. A displacement vector $\{u_i\}$,

namely local mode, can be constructed from the Γ_{15} soft mode using its eigenvector for every unit cell. For the Γ_{15} acoustic mode, a strain tensor $\{\eta\}$ is added to act for each unit cell. In this way, the number of degrees of freedom is greatly reduced. Note here atomic units are used through this section. Next thing is to map out the energy contributions for these degrees of freedom.

The first contribution should be the energy of local modes at every unit cell [3]. Since the local modes are small displacements with respect to the cubic structure, it is possible to express the self energy in terms of polynomials of local modes. To ensure a double-well energy landscape, at least up to fourth order should be included with odd-order terms absent like

$$E_{self} = \sum_{i}^{N} \kappa {u_i}^2 + \alpha {u_i}^4 + \gamma(u_{ix}^2 u_{iy}^2 + u_{ix}^2 u_{iz}^2 + u_{iy}^2 u_{iz}^2), \tag{2.1}$$

where ${u_i}^2 = u_{ix}^2 + u_{iy}^2 + u_{iz}^2$. $\{\mathbf{u_i}\}$ is proportional to the dipole moment at unit cell i and N is the number of total unit cells. κ, α and γ are coefficients that are determined from first-principles calculations of a five-atom unit cell. Other higher order terms are ignored here as they have little influence on the properties of interest in this thesis.

The second contribution comes from the mutual interactions between local modes at neighbouring sites and therefore characterizes energy away from the Γ point. This kind of interaction shall decompose into two parts, long-range coulomb and short-range interactions. Long-range Coulomb interaction mimics the dipole-dipole interaction between local modes, while short-range interaction takes into account the electronic repulsion and hybridization between neighbouring local modes. For dipole-dipole interactions, the individual dipole moment $\mathbf{d_i}$ of unit cell i is $\mathbf{d_i} = Z^* \mathbf{u_i}$. Z^* is the Born effect charge of the soft mode, which can be calculated by the multiplication between soft mode eigenvector and the five ions' Born effect charges:

$$Z^* = \zeta_A Z_A^* + \zeta_B Z_B^* + \zeta_{O1} Z_{O1}^* + \zeta_{O2} Z_{O2}^* + \zeta_{O3} Z_{O3}^*, \tag{2.2}$$

where $\{\zeta\}$ is the soft mode eigenvector. Under periodic boundary conditions, this long-range-interaction energy can be rewritten as

$$E_{dpl} = \frac{1}{2} \sum_{ij,\alpha\beta}^{N} Q_{ij,\alpha\beta} u_{i\alpha} u_{j\beta}, \tag{2.3}$$

with

$$Q_{ij,\alpha\beta} = \frac{4Z^{*2}}{\varepsilon_\infty}\left[\frac{\pi}{\Omega_c}\sum_{\mathbf{G}\neq 0}\frac{1}{|\mathbf{G}|^2}exp(-\frac{|\mathbf{G}|^2}{4\lambda^2})cos(\mathbf{G}\cdot(\mathbf{R}_i-\mathbf{R}_j))G_\alpha G_\beta - \frac{\lambda^3}{3\sqrt{\pi}}\delta_{\alpha\beta}\delta_{ij})\right]. \tag{2.4}$$

Here $\mathbf{G}$ are reciprocal lattice vectors and Ω_c is the whole cell volume. α and β denote Cartesian components. Because it is long-range, it is very time consuming to calculate it. To avoid this, a simple assumption is taken that the position vectors $\mathbf{R_i}$, $\mathbf{R_j}$ and reciprocal vectors $\mathbf{G}$ are fixed while $Q_{ij,\alpha\beta}$ in Eq.2.4 are calculated once for all. The effect that strains enter into $\mathbf{R_i}$, $\mathbf{R_j}$ of $Q_{ij,\alpha\beta}$ in Eq. 2.4 is of high order and ignored. Now it saves a lot of time by computing $Q_{ij,\alpha\beta}$ first and storing it for later use. For short-range interaction between neighbouring local modes, only up to 3rd nearest neighbours are considered as this type of interaction mimics electronic repulsion and hybridization, and thus decreases very fast with increasing distance. It is written to 2nd order as

$$E_{short} = \frac{1}{2}\sum_{i\neq j}^{N}\sum_{\alpha\beta}J_{ij,\alpha\beta}u_{i\alpha}u_{j\beta}. \tag{2.5}$$

The $J_{ij,\alpha\beta}$ parameters are determined from a series of first-principles calculations. Due to the high symmetry of the reference structure, these parameters have been greatly simplified of which only 7 distinct $J_{ij,\alpha\beta}$ parameters are possible. Details are given in Ref.[3].

The next contribution to the total energy is from elastic energy associated with strain tensors $\{\eta_{il}, l = 1, ..., 6\}$ in Voigt notation that relate to Γ_{15} long wavelength acoustic modes. $\{\eta_{il}, l = 1, ..., 6\}$ tensor at unit cell i is calculated from the dimensionless displacements $\mathbf{v}(\mathbf{R_i})$ located at the corner A atoms from unit cell i and its adjacent unit cells. Reduced by symmetry, it is expressed to 2nd order as

$$\begin{aligned} E_{elastic,I} = \sum_{i}^{N}\Bigg\{ & \frac{B_{11}}{4}[v_x(\mathbf{R}_i) - v_x(\mathbf{R}_i \pm \mathbf{x})]^2 \\ & + \frac{B_{12}}{8}[v_x(\mathbf{R}_i) - v_x(\mathbf{R}_i \pm \mathbf{x})][v_y(\mathbf{R}_i) - v_y(\mathbf{R}_i \pm \mathbf{y})] \\ & + \frac{B_{44}}{8}[v_x(\mathbf{R}_i) - v_x(\mathbf{R}_i \pm \mathbf{y}) + v_y(\mathbf{R}_i) - v_y(\mathbf{R}_i \pm \mathbf{x})]^2 \\ & + \text{cyclic permutation}\Bigg\}. \end{aligned} \tag{2.6}$$

To mimic the long wavelength deformation, a homogeneous part of such deformation is missing in Eq. 2.6. Therefore, an additional homogeneous strain tensor $\{\eta_{H,l}, with\ l = 1, ...6\}$ is

required. Similarly, the deformation homogeneous elastic energy is written as

$$E_{elastic,H} = N\Bigg[\frac{B_{11}}{2}({\eta_{H,l}}^2 + {\eta_{H,2}}^2 + {\eta_{H,3}}^2) + B_{12}(\eta_{H,l}\eta_{H,2} + \eta_{H,l}\eta_{H,3} + \eta_{H,2}\eta_{H,3}) + \frac{B_{44}}{2}({\eta_{H,4}}^2 + {\eta_{H,5}}^2 + {\eta_{H,6}}^2)\Bigg], \tag{2.7}$$

where B_{11}, B_{12} and B_{44} are elastic constants and are determined by first-principles calculations.

The final contribution comes from the interaction between strains and local modes, which accounts for the interaction between soft mode and acoustic mode. To simplify, only on-site interaction is considered. Its expression is written as:

$$E_{elastic-mode} = \frac{1}{2}\sum_{i,l\alpha\beta} B_{l\alpha\beta}\eta_l(\mathbf{R_i})u_{i\alpha}u_{i\beta}. \tag{2.8}$$

Here $\eta_l(\mathbf{R_i})$ is the total strain at unit cell i and thus includes both homogeneous and inhomogeneous parts. $B_{l\alpha\beta}$ are parameters that are determined from first-principles calculations. Due to the high symmetry of the reference structure, only three distinct parameters are obtained:

$$\begin{aligned} &B_{1xx} = B_{2yy} = B_{3zz}, \\ &B_{1yy} = B_{1zz} = B_{2xx} = B_{2zz} = B_{3xx} = B_{3yy}, \\ &B_{4yz} = B_{4zy} = B_{5xz} = B_{5zx} = B_{6xy} = B_{6yx}. \end{aligned} \tag{2.9}$$

More details are given in Ref. [3]. The total energy E is given as a sum of all the energy terms above as:

$$E = E_{self} + E_{dpl} + E_{short} + E_{elastic,I} + E_{elastic,H} + E_{elastic-mode}. \tag{2.10}$$

Outputs from such effective Hamiltonian are local modes and strains from which one can obtain polarization, dipole configurations, dielectric constants and piezoelectric coefficients. The expressions to calculate dielectric constants $\{\chi_{\alpha\beta}, \alpha = 1, ..., 3, \beta = 1, ..., 3\}$ and piezoelectric coefficients $\{d_{\alpha l}, \alpha = 1, ..., 3, l = 1, ..., 6\}$ are given in Refs. [11, 12] as:

$$\begin{aligned} \chi_{\alpha\beta} &= \frac{\beta N(Z^* e a_0)^2}{V}(< u_\alpha u_\beta > - < u_\alpha >< u_\beta >), \\ d_{\alpha l} &= \ \beta N(Z^* e a_0)(< \zeta_l u_\alpha > - < \zeta_l >< u_\alpha >), \end{aligned} \tag{2.11}$$

where

$$u_\alpha = \frac{1}{N}\sum_i^N u_{i\alpha},$$

and $< ... >$ means statistically average.

All above discussions of effective Hamiltonian are for pure systems and it can be extended to some alloy solutions like (A'A")BO_3 or A(B'B")O_3 alloys. Since (Ba,Sr)TiO_3 (BST) systems is of interest to this thesis, A-site alloys are depicted here. These schemes are detailed in Refs. [4, 13]. Such schemes make it possible to explore finite-temperature properties for the full composition range of perovskite alloys or superlattices. The general guide from Ref. [4] is repeated below.

First, the starting composition for BST is chosen to be 50% Ba and 50% Sr, i.e., it corresponds to the ($Ba_{0.5}Sr_{0.5}$)TiO_3 system. Any other composition of BST alloy can be viewed as the composition variation from this averaged system. Thus, the total effective Hamiltonian is written as:

$$E_{total} = E_{ave} + E_{loc},$$

with

$$\begin{aligned} E_{loc} = & \sum_{ij}(Q_{j,i}\sigma_j \hat{\mathbf{e}}_{ji}\cdot\mathbf{u}_i + R_{j,i}\sigma_j \hat{\mathbf{f}}_{ji}\cdot\mathbf{v}_i) \\ & + \tfrac{1}{2}\sum_i\sum_{l,\alpha\beta} B_{l\alpha\beta}\eta_{loc,l}(i)u_{i\alpha}u_{i\beta}, \end{aligned} \tag{2.12}$$

where σ_j denotes Ba $(+1)$ or Sr (-1) ion at the A site of unit cell j. $Q_{j,i}$ and $R_{j,i}$ are parameters that mimic the effects of composition variations from ($Ba_{0.5}Sr_{0.5}$)TiO_3 on local mode $\mathbf{u}_i$ and A-site displacement $\mathbf{v}_i$, and are determined from first-principle calculations. Unit vector $\hat{\mathbf{e}}_{ji}$ is along the direction from A site of unit cell j to B site of unit cell i. And unit vector $\hat{\mathbf{f}}_{ji}$ is along the direction from A site of unit cell j to A site of unit cell i. Usually it is enough to include only first nearest neighbours for $Q_{j,i}$ and up to 3rd nearest neighbours for $R_{j,i}$. $\eta_{loc,l}(i)$ in the second term of E_{locl} is given as:

$$\begin{aligned} &\eta_{loc,1}(i) = \eta_{loc,2}(i) = \eta_{loc,3}(i) = \tfrac{\Delta a}{8a}\sum_j \sigma_j, \\ &\eta_{loc,4}(i) = \eta_{loc,5}(i) = \eta_{loc,6}(i) = 0, \end{aligned} \tag{2.13}$$

where j runs over all eight neighbour unit cells that have A sites nearest to the B site of unit cell i. Δa is the difference between the lattice constants of bulk $BaTiO_3$ and $(Ba_{0.5}Sr_{0.5})TiO_3$ (of which the lattice constant is denoted by a) in their cubic phases extrapolated to 0 K. The value of $\frac{\Delta a}{a}$ is computed to be 0.01087. The potential of A atom used to obtain the 0 K lattice constant of the latter is assigned to the average of Ba and Sr pseudopotentials. Thus the second term in E_{locl} adds the interaction as $E_{elastic-mode}$ in Eq. 2.8 resulting from the strains induced by composition variations of A sites.

So far, the effective Hamiltonians that are used in this thesis have been given an overall description, of which the parameters determined from first-principles calculations can be found in Ref. [4], particularly.

Density Functional Theory

The advantages of effective Hamiltonian method have been concisely summarized in last section. However, this semiclassical type method has its incapabilities when detailed electronic calculations are required. To solve this problem, one has to resort to solving Schrödinger equation, if only non-relativistic frame is considered which is enough for most of cases. For a system that has a unit cell of multiple ions, the time-independent Schrödinger equation is given in position representation as:

$$H\psi(\{\mathbf{R}_n\};\{\mathbf{r}_i\}) = E\psi(\{\mathbf{R}_n\};\{\mathbf{r}_i\}), \tag{2.14}$$

where *H* is the exact Hamiltonian that includes both ions and electrons contributions: kinetic energies, ion-ion Coulomb interactions, electron-electron Coulomb interactions, electron-ion Coulomb interactions and external potentials; $\psi(\{\mathbf{R}_n\};\{\mathbf{r}_i\})$ is the total wavefunction that involves both ions and electrons and gives the state of the system; $\mathbf{R}_n$ is the position vector of the nth ion and $\mathbf{r}_i$ is the position vector of ith electron. *H* is written explicitly as:

$$\begin{aligned} H=&\sum_n -\frac{\hbar^2}{2M_n}\nabla^2_{\mathbf{R}_n} - \sum_i \frac{\hbar^2}{2m_i}\nabla^2_{\mathbf{r}_i} + \frac{1}{2}\sum_{n\neq m}\frac{Z_m Z_n e^2}{|\mathbf{R}_m-\mathbf{R}_n|} \\ &+ \frac{1}{2}\sum_{i\neq j}\frac{e^2}{|\mathbf{r}_j-\mathbf{r}_i|} - \sum_{i,n}\frac{Z_n e^2}{|\mathbf{r}_j-\mathbf{R}_n|}, \end{aligned} \tag{2.15}$$

where Z_n (M_n) is the valence charge (mass) of the nth ion and m_i is the mass of the ith electron. A first glance at Eqs. 2.14 and 2.15 reveals that there are too many degrees of freedom. The

first choice is to separate the motions of ions from that of electrons, which is well known as the Born-Oppenheimer approximation. Basically, due to its much larger masses of ions than electrons, ions are considered to move much slower than electrons. So it is assumed that, at every instant of ionic positions, the electrons are fast enough to reach their equilibrium. In this way, ionic motions can be treated classically, while electrons require quantum mechanic descriptions. Then Eq. 2.15 reduces to

$$H=\sum_i \frac{\hbar^2}{2m_i}\nabla^2_{\mathbf{r}_i} + \frac{1}{2}\sum_{i\neq j}\frac{e^2}{|\mathbf{r}_j-\mathbf{r}_i|} - \sum_{i,n}\frac{Z_n e^2}{|\mathbf{r}_i-\mathbf{R}_n|}, \tag{2.16}$$

where $\{\mathbf{R}_n\}$ are then input parameters when solving Eq. 2.14. For a simple system of only very few electrons, such as H_2, it is not difficult to obtain its ground state by computers. For a system of multiple ions and electrons, solving Eq. 2.14 becomes an overwhelming task to accomplish due to the couplings of electrons: exchange and correlation effects. From Pauli's theory based on quantum electrodynamics, the total wavefunction of a system of multiple electrons must change its sign at the exchange of two electrons' positions; as seen from above, any electron's behavior is affected by other electrons as in typical many-body problem, which is where correlation effect comes from. As a result, further simplifications are needed to make the problem tractable.

The first few approaches are Hartree approximation and Hartree-Fock (HF) approximation as depicted in many textbooks. Both of them started by assuming a specific form of the total wavefunction. And the latter uses a Slater determinant of single-particle orbitals [14]:

$$\Psi(\mathbf{r}_1,\mathbf{r}_2,...,\mathbf{r}_N) = \frac{1}{\sqrt{N!}}\begin{vmatrix} \phi_1(\mathbf{r}_1) & \phi_1(\mathbf{r}_2) & ... & \phi_1(\mathbf{r}_N) \\ \phi_2(\mathbf{r}_1) & \phi_2(\mathbf{r}_2) & ... & \phi_2(\mathbf{r}_N) \\ . & . & ... & . \\ . & . & ... & . \\ \phi_N(\mathbf{r}_1) & \phi_N(\mathbf{r}_2) & ... & \phi_N(\mathbf{r}_N) \end{vmatrix}, \tag{2.17}$$

where N is the number of total electrons. The spin parts are intentionally left out for simplicity and can be included without a problem. Put $\Psi(\mathbf{r}_1,\mathbf{r}_2,...,\mathbf{r}_N)$ into Eq. 2.14, and make a function

variational calculation. Then the single-particle HF equation is obtained as:

$$\big[-\frac{\hbar^2}{2m_e}\nabla^2_{\mathbf{r}}-\sum_n\frac{Z_ne^2}{|\mathbf{r}_i-\mathbf{R}_n|}+\int e^2\frac{\rho(\mathbf{r}')-\rho_i'(\mathbf{r},\mathbf{r}')}{|\mathbf{r}-\mathbf{r}'|}d\mathbf{r}'\big]\phi_i(\mathbf{r})=\epsilon_i\phi_i(\mathbf{r}), \tag{2.18}$$

where

$$\rho_i(\mathbf{r})=\sum_i|\phi_i(\mathbf{r})|^2,\quad \rho_i'(\mathbf{r},\mathbf{r}')=\sum_j\frac{\phi_i^*(\mathbf{r})\phi_i(\mathbf{r}')\phi_j^*(\mathbf{r}')\phi_j(\mathbf{r})}{\phi_i^*(\mathbf{r})\phi_i(\mathbf{r})}. \tag{2.19}$$

The term containing $\rho_i'(\mathbf{r},\mathbf{r}')$ characterizes the exchange effect. The solutions to Eq. 2.18 can be obtained through self-consistent computer iterations.

The other approach is Density Functional Theory (DFT) contributed by Hohenberg, Kohn and Sham [15, 16]. Here only the basic sketch of DFT will be repeated. The critical idea is to express key physics quantities in terms of density $n(\mathbf{r})$ instead of the total wavefunction which is far from being known. First thing, it needs to justify the one-on-one correspondence between density $n(\mathbf{r})$ and the total Hamiltonian (the potential terms combined, to be exact) in Eq. 2.16. Suppose there are two different potentials $V(\mathbf{r})$ and $V'(\mathbf{r})$ corresponding to the same given density $n(\mathbf{r})$. And the ground states and energies of these two systems with $V(\mathbf{r})$ and $V'(\mathbf{r})$ are (Ψ, E) and (Ψ', E'). Then

$$\begin{aligned}
E&<\langle\Psi'|T+V(\mathbf{r})|\Psi'\rangle=\langle\Psi'|T+V'(\mathbf{r})+V(\mathbf{r})-V'(\mathbf{r})|\Psi'\rangle\\
&=E'+\langle\Psi'|V(\mathbf{r})-V'(\mathbf{r})|\Psi'\rangle,\\
E'&<\langle\Psi|T+V'(\mathbf{r})|\Psi\rangle=\langle\Psi|T+V(\mathbf{r})-V(\mathbf{r})+V'(\mathbf{r})|\Psi\rangle\\
&=E+\langle\Psi|-V(\mathbf{r})+V'(\mathbf{r})|\Psi\rangle,
\end{aligned} \tag{2.20}$$

where the two different potentials differ from each other by more than a constant. Adding these two inequalities gives:

$$\begin{aligned}
&E+E'<E+E'+\langle\Psi'|V(\mathbf{r})-V'(\mathbf{r})|\Psi'\rangle-\langle\Psi|V(\mathbf{r})-V'(\mathbf{r})|\Psi\rangle,\\
&E+E'<E+E'+\int n(\mathbf{r})[V(\mathbf{r})-V'(\mathbf{r})]d\mathbf{r}-\int n(\mathbf{r})[V(\mathbf{r})-V'(\mathbf{r})]d\mathbf{r},\\
&E+E'<E+E'.
\end{aligned} \tag{2.21}$$

This inequality is impossible. So the assumption is invalid that two different potentials can correspond to the same given density. In other words, there is one unique density $n(\mathbf{r})$ that

belongs to a given system. Thus, it is natural that the total wavefunction is a functional of density, so are other physical quantities. This conclusion has a very significant consequence which makes it possible to simulate an interacting many-body system by a non-interacting many-body system as long as giving the same charge density, which will finally be subjected to a single-particle description. To include the exchange and correlation effects, an additional energy term, E^{XC}, the exchange-correlation term, is added. From a variation process, Kohn-Sham single-particle equation is obtained as:

$$\big[-\frac{\hbar^2}{2m_e}\nabla^2_{\mathbf{r}} + \int \frac{e^2 n(\mathbf{r}')}{|\mathbf{r}-\mathbf{r}'|} d\mathbf{r}' - \sum_n \frac{Z_n e^2}{|\mathbf{r}-\mathbf{R}_n|} + \frac{\delta E^{XC}[n(\mathbf{r})]}{\delta n(\mathbf{r})} \big] \phi_i(\mathbf{r}) = \varepsilon_i \phi_i(\mathbf{r}), \tag{2.22}$$

where $\{\phi_i(\mathbf{r})\}$ are called Kohn-Sham orbitals that can be calculated through self-consistent computer iterations. However, the exact form of $E^{XC}[n(\mathbf{r})]$ has been a mystery up to today. There are a lot of works that have been devoted to this issue. A couple of approximated expressions are well known and three of them are mentioned here. The first type of exchange-correlation functions depends on the local density $n(\mathbf{r})$, which is a sole function of position $\mathbf{r}$. Thus, this type is now termed as local density approximation (LDA) [17, 18, 19]. The second type of E^{XC} depends on not only the local density $n(\mathbf{r})$, but also its gradient, which is termed as the generalized-gradient approximation (GGA) [20, 21, 22, 23]. The third type is a combined functional consisting of Hartree-Fock exchange functional and LDA or GGA functional [24, 25].

The above exchange-correlation functionals LDA and GGA are approximations and/or corrections based on homogeneous electron gas. Therefore, they have severe consequences when dealing with strongly localized and correlated electron states, e.g., d and f electrons in transition metal oxides and rare-earth compounds. Such consequences include underestimated band gap and incorrect magnetic configurations. The possible reason behind these consequences is that neither LDA or GGA doesn't suffice to correct the non-physical self interaction in their exchange-correlation functionals. An efficient technique to resolve this insufficiency is called LDA + U [26, 27, 28, 29]. The "U" in "LDA + U" stands for the Hubbard-like on-site repulsion correction added to the exchange-correlation functionals, which can be evaluated by

constrained DFT calculations or fitting to experimental results.

As it is mentioned above, the incorporations of spin components inside those single-particle aforementioned equations are straightforward [30]. The key part is to express the exchange-correlation functional in terms of spin-up and spin-down electron densities for collinear spin arrangements. However, for non-collinear spin arrangements, it is effective to introduce an exchange-correlation magnetic field $\mathbf{B}_{xc}$ [31]:

$$\mathbf{B}_{xc} = -\frac{\delta E_{xc}[n(\mathbf{r}), \mathbf{m}(\mathbf{r})]}{\delta \mathbf{m}(\mathbf{r})}, \tag{2.23}$$

where $\mathbf{m}(\mathbf{r})$ ($= \sum_i \phi_i(\mathbf{r})\sigma\phi_i(\mathbf{r})$) is the magnetization density. σ is the Pauli spin matrix. Generally, these single-particle orbital wavefunctions $\{\phi_i(\mathbf{r})\}$ contain a two-component spinor.

The last issue remaining in this subsection is the pseudopotential method that has been excellently reviewed in details in Ref. [32]. Its main purpose is to use an effective smooth ionic potential that acts on the valence electrons and combines all the effects from the nucleus and the tightly bound core electrons. Two commonly used type of pseudopotentials are norm-conserving and ultrasoft pseudopotentials [32]. Here the generalization procedures will not be repeated here. Details of them can be found in Ref. [32] and references therein.

So far, the main methods used in calculations presented in later chapters have been introduced here. Other employed techniques will be described along when necessary.

Chapter 3

Finite-temperature static properties of $BaTiO_3$ epitaxial films

Background

Ferroelectric (FE) materials have been of great interest because of their desirable properties that can be used in devices design, such as high-frequency capacitors and ferroelectric random access memories [1, 2]. A lot of efforts have been devoted to optimize their properties, such as growing superlattices and solid solutions. One particular way to achieve this goal is epitaxial growth utilizing the misfit strain between the host films and substrates because of the fact that there exists a strong interaction between strain and other degrees of freedom. These have been shown in a lot of calculations and experimental works devoted to epitaxial thin films [33, 34, 35, 36, 37, 38, 39, 40]. As a result, novel features have been reported in these nanostructures made of the prototype $BaTiO_3$ (BTO) ferroelectrics. For instance, FE thin films under short-circuit-like electrical boundary conditions (for which the depolarizing field vanishes or is rather small, as a result of a large screening of the polarization-induced surface charges) exhibit different directions for the spontaneous polarization and different resulting crystallographic phases, depending on the misfit strain. Another example is the tuning of the Curie temperature through misfit strains in BTO ferroelectric films. All these interesting features are found in FE films grown along the [001] pseudo-cubic direction. Interestingly, there is still at least another variable in this strain engineering, which is the growth direction. The variation of growth directions may lead to altered properties of FE films. Unfortunately, there have been very few experimental or theoretical works regarding this topic [41, 42, 43, 44]. In this chapter, we will present several studies of BTO films: (i) BTO films grown along a high symmetric direction, i.e., [110]; (ii) BTO films grown along a continuous path varying from [001] to [110]

on a single substrate. These studies have been originally reported in Refs. [46, 47].

Method

In the studies here, the effective Hamiltonian given in Chapter 2 implemented in the Monte Carlo (MC) Metropolis algorithm is used. MC simulations are very effective in simulating finite-temperature properties of a variety of systems. The detailed procedures of a MC simulation can be found in many textbooks. Here only the critical principles will be given here.

Markov chains. Suppose there is a system with a series of states $\{\phi_i, with\ i = 1, 2, 3...\}$ and a consecutive flow of discrete times denoted by $\{t_n, with\ n = 1, 2, 3...\}$. $\phi_i(t_n)$ represents the system in state ϕ_i at time t_n. So at time t_{n+1}, the probability of the system in state ϕ_j will only depend on the state ϕ_i at time t_n. This chain consisting of such states is called a Markov chain. The probability of the system transiting into the state $\phi_j(t_{n+1})$ from residing in the state $\phi_i(t_n)$ is W_{ij}. The probability of the system in the state $\phi_i(t)$ is denoted as $P(\phi_i, t)$. So when the system is in equilibrium at time t, the probability of system transiting into the state $\phi_j(t)$ shall cancel out the probability of system transiting out of the state $\phi_j(t)$. This is the detailed balance of the probability $P_{eq}(\phi_j)$ (i.e., the probability of the system in state ϕ_j at equilibrium which is of course independent of time) written as:

$$W_{ji}P_{eq}(\phi_j) = W_{ij}P_{eq}(\phi_i). \tag{3.1}$$

According to classical statistical mechanics, the probability of the system in state ϕ_j at equilibrium is given as:

$$P_{eq}(\phi_j) = e^{-E_j\beta}/Z, \tag{3.2}$$

where Z is the associated partition function. In a Markov process, from Eq. 3.1, one obtains

$$W_{ij} = \frac{W_{ji}P_{eq}(\phi_j)}{P_{eq}(\phi_i)} = e^{-(E_j-E_i)\beta}W_{ji}. \tag{3.3}$$

Clearly, there is still freedom to assign W_{ji}. A algorithm proposed by Metropolis is

$$W_{ij} = e^{-(E_j - E_i)\beta},\ if\ E_j - E_i > 0; \tag{3.4}$$

$$= 1, \qquad if\ E_j - E_i \leq 0. \tag{3.5}$$

Apparently, this choice satisfies detailed balance in Eq. 3.1. And it is also very easy to implement in MC simulations. The equilibrium properties of the system will be collected statistically after the MC simulation reaches equilibrium. For the calculations in our study, 300000 MC steps are used, of which the last 200000 steps are collected for the statistical results.

In the current Monte-Carlo (MC) simulations, three-dimensionally periodic 12 $\times$ 12 $\times$ 12 supercells (8,640 atoms) are used. As it is commonly done in many previous calculations (see, e.g. Refs.[33, 45, 36]), such periodic boundary conditions presume that the effect of the surface on the films' properties is intentionally left out in order that the combined effects of the strain and growth direction on these properties can be isolated from surface effects. To start, there are two different coordinate systems used here [46, 47]: (1) the "usual" (xyz) system for which the x-, y- and z-axes coincide with the pseudo-cubic [100], [010], [001] directions, respectively; and (2) the other coordinate system (x'y'z') in which the z'-axis corresponds to the growth direction of the film and in which the x'-, y'- and z'-axes are practically chosen to be along the pseudo-cubic [$\bar{1}$10], [*mmn*], and [hhk] directions, respectively, with *m*=-cos(θ)/$\sqrt{2}$, *n*=sin(θ), *h*=sin(θ)/$\sqrt{2}$ and *k*=cos(θ), where θ is the angle between the z'- and z-axes and will be referred to as the growth angle afterwards. Note that when θ is set to 0^o, 90^o and 54.7^o, it corresponds to the pseudo-cubic [001], [110] and [111] growth direction, respectively. Then the mimicking of finite-temperature properties of BTO films that are *epitaxially* grown along the z'-axis is accomplished by imposing the following conditions for the homogeneous strain tensor (in Voigt notation): $\eta_{1'} = \eta_{2'} = (a_{sub}\text{-}a_{lat})/a_{lat} = \delta$ and $\eta_{6'} = 0$, while $\eta_{3'}$, $\eta_{4'}$ and $\eta_{5'}$ can fully relax during the simulations [46, 47]. Here, the prime ' is used to denote properties computed in the (x'y'z') coordinate system. a_{sub} is the in-plane lattice constant of the substrate and a_{lat} is the lattice parameter of the BTO paraelectric bulk at the Curie temperature, T_c ($\simeq$ 395K). δ then characterizes the misfit strain experienced by the epitaxial films. Note that the interface between BTO and STO, beyond the strain effect that is taken into account in our simulations,

is known to have rather minor effects on properties of BTO films, especially if these films have a thickness being large enough (but smaller than the critical thickness associated with the full strain relaxation of the films) [48, 49]. Its effect beyond the mediation of the strain is thus neglected here. Note that also several studies (see, e.g., Refs. [40, 50, 51]) demonstrated that (for a given growth direction) one of the most important aspects of ferroelectric thin films is the amount of strain experienced by these films and arising from the lattice mismatch between the materials forming the film and the substrate. In other words, effects, such as surface reconstruction, film's thickness or precise morphology or stoichiometry of the substrate, have typically much less consequence on physical properties of these films than the epitaxial strain.

BTO films grown along pseudo-cubic [110] direction

First, let us focus on BTO films grown along pseudo-cubic [110] direction. To begin, some commonly used notations shall be clarified for FE phase transitions. Suppose the x-, y- and z-components (in the usual pseudo-cubic frame) of the polarization in a state are denoted as u_x, u_y and u_z, respectively. Then the category follows this way [33, 37]: (1) all the three components are all zero, which is termed as p phase, i.e., paraelectric phase (PE); (2) only one of the three components is non-zero, which is termed as c phase; (3) two of the three components are non-zero and equal, which is termed as aa phase; (4) two of the three components are non-zero and not equal, which is termed as ab phase; (5) all the three components are non-zero and equal to each other, which is termed as r phase; (6) all the three components are non-zero and only two are equal, which is called either r_{aa} (if the magnitude of the third one is smaller than the two of equal magnitude) or r_c (if the magnitude of the third one is larger than the two of equal magnitude); (7) all the three are non-zero and not equal, which is termed as abc phase. The epitaxial strain range under this study is from -3.6% (in compressive strain region) to 2.9% (in tensile strain region).

Fig. 3.1 gives a detailed and rich temperature-misfit-strain phase diagram. At low temperature, e.g., 5K, the system goes from aa phase in the large compressive strain region, to r_{aa} phase in the smaller compressive strain region, and to r_c phase in the tensile strain region. Such phase sequence lasts up to 250K. This is totally different from (001) BTO films which is just

the opposite case (r_{aa} and aa phases in the tensile strain region and r_c phase in the compressive strain region). This discrepancy is easily understood using the fact that large compressive strain

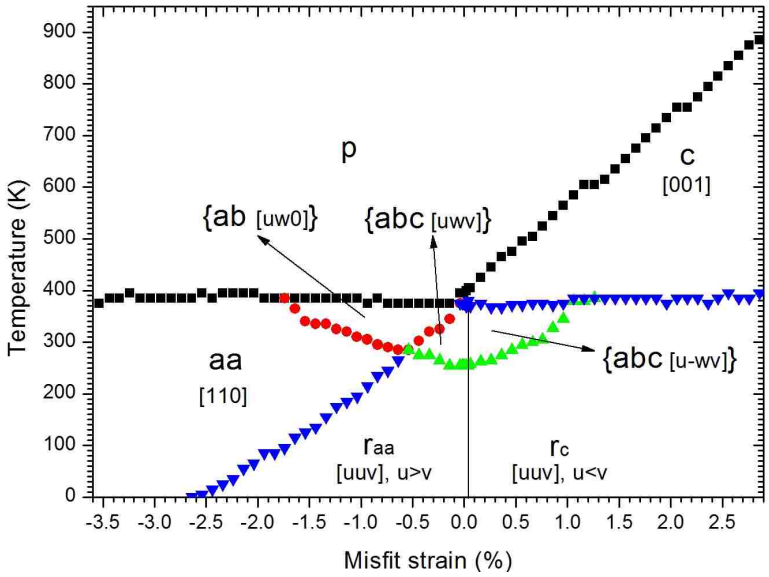

Figure 3.1: The predicted temperature-versus-misfit strain phase diagram of (110) BTO films: The phases displayed in the diagram are explained and discussed in the text. The direction of their polarization is further indicated in the (xyz) coordinate frame near the phases' names.

favors the out-of-plane component of the polarization and large tensile strain favors the in-plane component of the polarization. In this case, the out-of-plane is the [110] instead of the [001] pseudo-cubic direction. Around zero strain where the boundary lies between r_{aa} and r_c phase, the polarization lies exactly along the pseudo-cubic $[1\bar{1}1]$, coincident with one of the eight $\langle 111 \rangle$ minimums of bulk BTO in its ground state. To better understand this, Fig. 3.2 shows the evolutions of the polarization with respect to misfit strain in (xyz) frame (Fig. 3.2a) and (x'y'z') frame (Fig. 3.2b). The polarization vector rotates from $[uu0]$ (coinciding with [110]

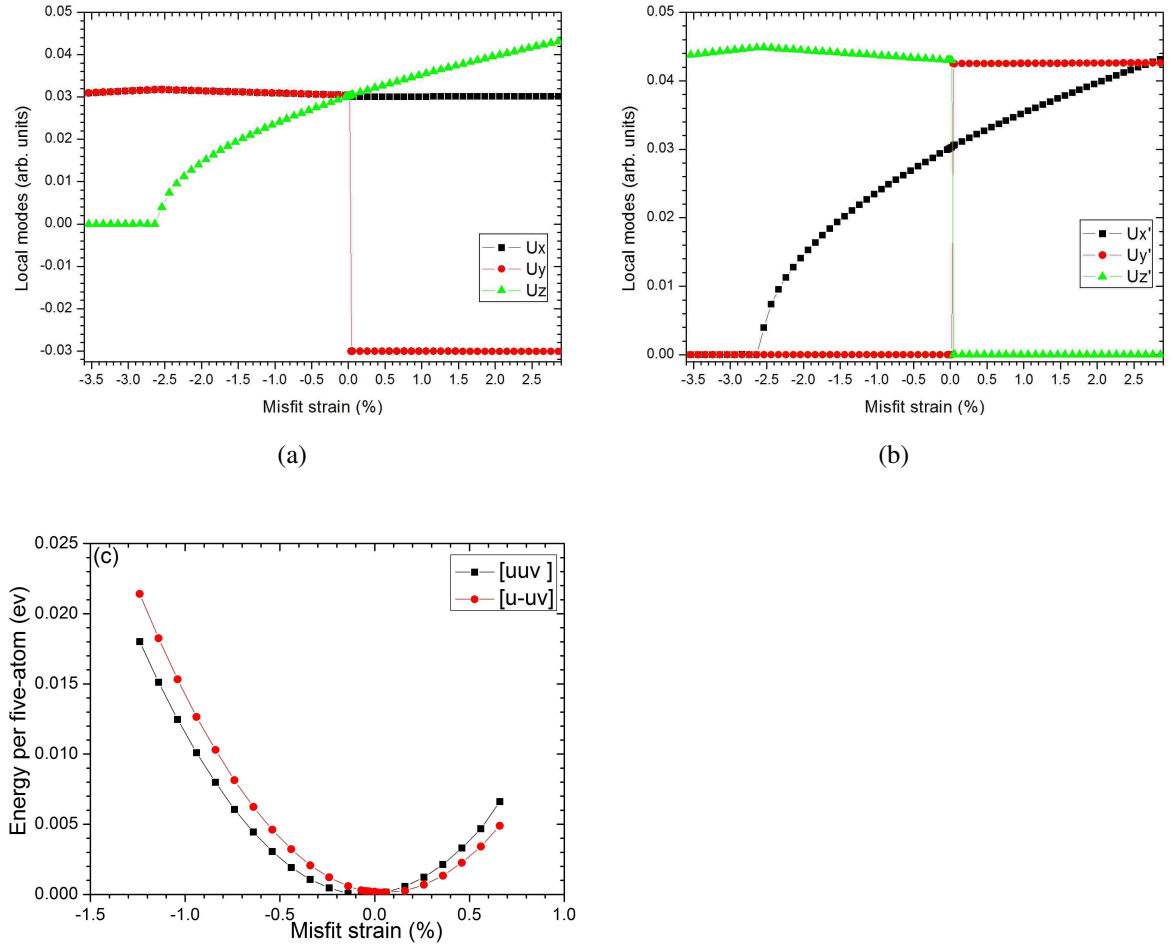

Figure 3.2: Dependency of properties on epitaxial strain in the (110) BTO film at 5K. Panels (a) and (b) show the local modes in the (xyz) and (x'y'z') coordinate frame, respectively. Panel (c) displays the total energy for the two stable phases having a polarization lying along $[uuv]$ and $[u\bar{u}v]$. The zero in energy corresponds to the energy associated with the zero misfit strain.

pseudo-cubic direction) to $[uuv]$, and suddenly to $[u\bar{u}v]$ when the misfit strain varies from the compressive strain region to the tensile strain region. Around zero strain, there is a sudden jump of the y-component of the polarization from a positive value to a negative value (i.e., a first-order transition occurs). To confirm it, Fig. 3.2c gives the energy comparison between the polarization in the $[uuv]$ configuration and the $[u\bar{u}v]$ configuration, which indeed shows that the $[uuv]$ configuration is more energetically favorable in the compressive strain region and that the $[u\bar{u}v]$ configuration is more energetically favorable in the tensile strain region. When seen in the (x'y'z') frame, Fig. 3.2b shows clearly that the polarization is totally out of plane at large compressive strain, and that the polarization is totally in plane in the tensile strain region.

This is consistent with the fact that large compressive strain favors out-of-plane component of the polarization and large tensile strain favors in-plane component of the polarization. Since the two configurations are so close in energy for a certain range of strain, simple application of a small external electric field along the out-of-plane direction (easily seen in Fig. 3.2b) in the tensile strain region can change the system into the metastable state in which the polarization lies along the $[uuv]$ direction and the out-of-plane component occurs. Applying an in-plane electric field will get the system back into its ground state with the polarization relaxing to the $[u\bar{u}v]$ configuration, which results in the vanishing of the out-of-plane component of the polarization. Such simply and efficiently controlled hopping between two states offers a novel scheme to realize memory engineering with the occurring and vanishing of the out-of-plane component of polarization corresponding to 1 and 0. The similar scheme can be used in the compressive region except that the order of the directions of applied electric field will have to be changed.

Let us now look at a higher temperature, e.g., one between 255K and 285K. The system varies from the aa phase to r_{aa} phase, abc phase (with the polarization having a $[uwv]$ configuration which is a triclinic phase), abc phase (with the polarization being along a $[u\bar{w}v]$ direction which is also a triclinic phase), and r_c phase. These low-symmetric triclinic phases are quite rare and not existing in (001) BTO films. When the temperature is between 285K and 385K, e.g., 300K, the system undergoes another series of phase transitions, from aa to ab, abc (with the polarization along a $[uwv]$ direction), abc (with the polarization along a $[u\bar{w}v]$ direction) and r_c phase. The last four phases are all low-symmetric states, which manifest themselves by the fast rotation of the polarization vector shown in Figs. 3.3a and 3.3b. Around -0.5% strain and 0.5% strain, the polarization vector rotates very fast, which results in enormously large dielectric responses and piezoelectric coefficients as shown in Figs. 3.3c and 3.3d. At around -0.65% and 0.5% strains, the x- and y-components of the polarization change very fast, which gives large responses from dielectric susceptibilities χ_{11}, χ_{22} and piezoelectric coefficients d_{11} and d_{22}; at around -0.45% strain, the fast variation of the z-component leads to exceptionally large response from dielectric susceptibility χ_{33} and considerable response from the piezoelectric coefficient d_{35}. Between -0.65% and 0.5% strains, the dielectric susceptibility χ_{22} stays

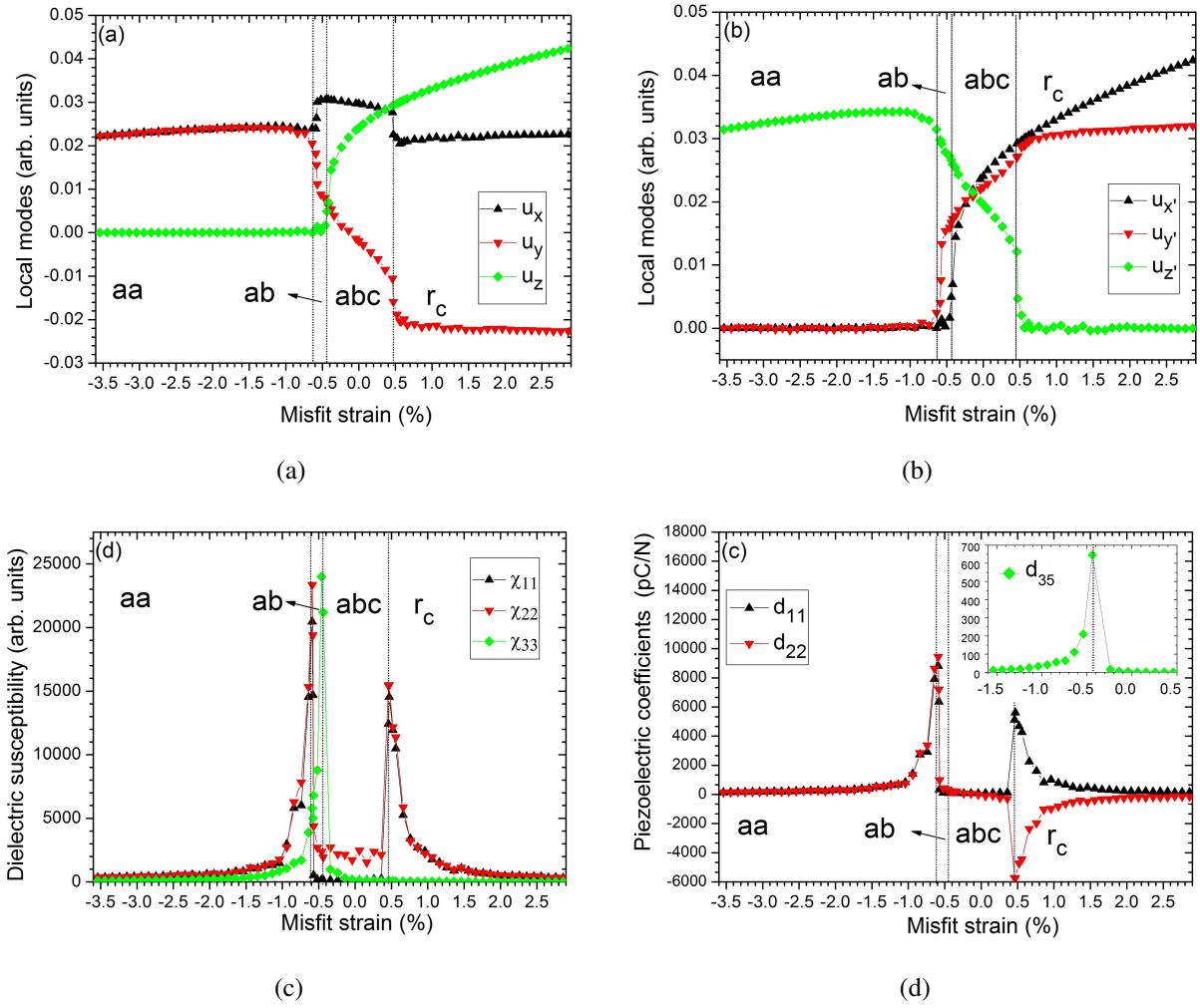

Figure 3.3: Dependency of properties on epitaxial strain in the (110) BTO film at 300K. Panels (a) and (b) show the local modes in the (xyz) and (x'y'z') coordinate frame, respectively. Panels (c) and (d) display the largest piezoelectric and dielectric coefficients, respectively — with the notation for subscript referring to the (xyz) frame (e.g., the 2 subscript corresponds to the pseudo-cubic [010] direction).

above 2000 for the whole range due to the fast change of the y-component of the polarization. These features are promising, and may be used in devices of specific functions, especially when these desirable properties happen for a large range of temperature window around room temperature (from 255K to 385K) and around zero strain. As the temperature goes even higher than 395K, the system will stay in p phase for the compressive strain region and c phase for the tensile strain region. One more unusual feature about this phase diagram is that the transition temperatures remain constant at around 385K from p phase to aa phase, p phase to ab phase, c phase to abc phase and c phase to r_c phase. This temperature is exactly our predicted

Curie temperature T_c of bulk BTO. To understand this unusual feature, one simple way is to resort to the ϕ^4 model which correlates the Curie temperature to the magnitude of the polarization at 0K through a simple proportionality [52, 53]. As we shall see from Figs. 3.2a and 3.2b, the magnitudes of the x- and y-components of the polarization stay more or less constant across the studied strain range. And the transitions above involve the emergences of these two components at low temperature, as consistent with the ϕ^4 model. To further understand the atomistic origin behind it, a phenomenological derivation similar to that in Ref. [39] is carried out to our situation. It shows that the independence of the local mode (that is proportional to the polarization) with respect to the misfit strain mainly comes from the balanced competition between various elasticity-local mode interactions and the anharmonic part of the local mode self-energy in our films. To be specific, in p-to-aa transition, the interactions between the local modes and "diagonal" strains (i.e., η_1, η_2, and η_3) will favor the increase of the magnitude of the x- and y-components of the local modes when increasing the magnitude of the compressive misfit strain, while the interaction between the local modes and shear strain (i.e., η_6) will depress them in an almost opposite way. This is also true for the c-to-r_c transition in the tensile strain region.

To further verify our predictions, direct DFT calculations are performed for epitaxial (110) BTO films using the Vienna Ab-initio Simulation Package (VASP). Ba $5s5p6s$, Ti $4s3d$ and O $2s2p$ electrons are treated as valence electrons. It confirms several interesting properties discussed above at low temperature: (1) the first-order transition between r_{aa} and r_c around zero strain; (ii) the same transition sequence, i.e., aa, r_{aa} and r_c as strain varies; (iii) a similar energy hierarchy as in Fig. 3.2c. In summary, the finite-temperature properties of epitaxial (110) BTO films have been studied using the effective Hamiltonian combined with Monte Carlo (MC) simulations. Several interesting features are found for this growth direction of high symmetry: (i) the existence of low-symmetry phases including three monoclinic ones (e.g., ab, r_{aa} and r_c) and an unusual triclinic phase (e.g., abc); (ii) near room temperature, there are a series of novel phase transitions: starting from an aa state (orthorhombic phase) in the far compressive strain region, then passing through an ab state (monoclinic phase) and an abc state (triclinic phase) by second order transitions in the near region of 0% strain, and finally turning into a r_c state (which

is another different monoclinic phase) by a first order transition; (iii) that the fast strain-induced rotation of the polarization associated with these latter transitions results in huge dielectric and piezoelectric responses, which is very promising to design efficient miniaturized lead-free devices; (iv) that one can easily switch between different polarized states by applying in-plane and out-of-plane electric fields, which is promising for the design of novel memory devices; and (v) that the Curie temperature in the compressive strain region is nearly independent of the epitaxial strain.

BTO films grown on a single substrate

As it is shown in last section, the growth direction plays an important role in shaping the properties of BTO epitaxial films. Either epitaxial (001) or (110) BTO presents a lot of novel properties that are absent in bulk BTO. However, there is an inevitable limitation on the number and magnitudes of epitaxial strains arising from available substrates. For example, the typical substrates for perovskite ferroelectrics are rather rare, e.g., $SrTiO_3$ and MgO. Sometimes, some of the novel properties pose a strong restriction on the lattice constant of the substrate which is not available. Moreover, it is very hard to grow coherent FE films on some substrates. In light of these limitations, a novel way to circumvent them is practically required. In Ref. [54], the authors proposed a interesting way to overcome such difficulty by exploiting the relation between the effective strain and the film thickness. Besides, there are few studies available about the effects of low-symmetric growth directions on properties of FE films, which contrasts with the case of semiconductors [55]. In this study, we will present an alternative in which only a single substrate is required. The basic idea here is to continuously rotate the growth direction through growing films on the high index atomic planes or different atomic facets of the substrate. To maintain the minimum destruction and the maximum coherence of the object film, a similar unit-cell structure of the substrate as the object film is desirable. We will discuss properties of BTO films grown on STO along a continuous set of rotating directions.

Specifically, BTO films will be grown along a direction varying from the pseudo-cubic [001] to [110] direction via the [111] direction, which is sketched in Fig. 3.4. At position 1, the growth direction is the conventionally used pseudo-cubic [001]; at position 2, the growth direc-

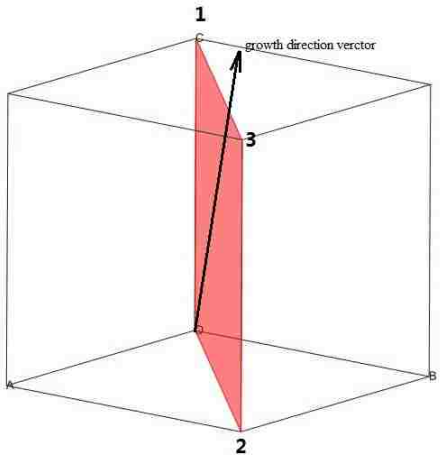

Figure 3.4: The schematic diagram of the rotational path of the growth direction. The growth direction vector is restricted inside the colored plane and rotates along the path 1-3-2.

tion is pseudo-cubic [110]; at the position 3, the growth direction corresponds to pseudo-cubic [111]. As the growth direction vector varies along path 1-3-2, the growth angle θ introduced in the Method part changes from 0^o to 90^o accordingly. For each chosen growth angle θ, we cool down the system from high to low temperature with a 5K step. The δ value is selected to correspond to the growth of the BTO films on the well-known and used STO substrate, therefore yielding $\delta = -2.2\%$.

Fig. 3.5 gives the temperature-*versus*-growth angle phase diagram of BTO films grown on a STO substrate as a function of the growth angle. This diagram displays several intriguing features. First, let us take a look at the phase transitions occurring in the phase diagram in Fig. 3.5. For small growth angle (near 0^o), the system makes a simple transition from p (paraelectric) phase to c phase (i.e., the polarization lies along the z direction) at around 755K, which is consistent with previous works [33, 37, 56]. Note that the experimental work in Ref. [56] gives a value of around 700K, which is fewer by around 50K. This discrepancy most likely arises from the strain relaxation present in the films, as indicated in their x-ray diffraction data. Note that we numerically check that when the misfit strain δ is set to -1.9%, our MC simulation gives a T_c of 705K which is very close to their measured T_c. This is in line with the fact that

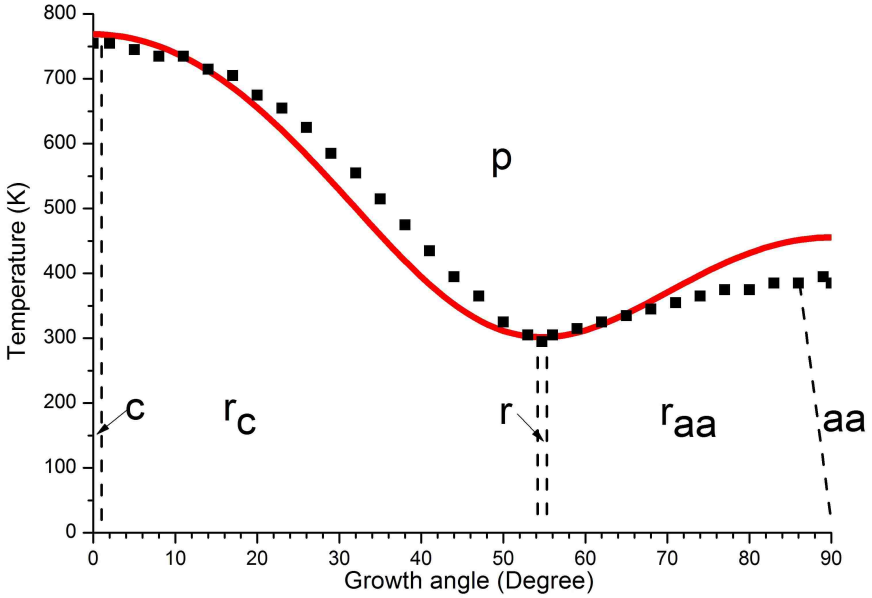

Figure 3.5: The temperature-*versus*-growth angle phase diagram of BTO films grown on a STO substrate as a function of the growth angle. The solid red line represents the fitting of T_c by Eq. 3.8, with the parameters of this fitting being: $M = 1022.83$, $N = 1754.88$, $\alpha_e = 1.04$, when assuming $\gamma_e = -1.00$. The dashed lines are approximate boundaries between phases and are a guide for the eyes.

the strain relaxation in the measured films is behind the discrepancy between measurements and calculations for T_c. Other reasons may also contribute to such discrepancy, e.g., the presence of defects in the grown films, or from the effective Hamiltonian method used here that neglects the finite thickness of the films. When the growth angle increases from 2^o to 54.7^o, BTO films undergo a transition from p phase to r_c phase (in which the polarization has a non-zero z-component and smaller equal x- and y-components as the temperature decreases). The resultant T_c ranges from 755K to 295K that is a decrease by 460K, which indicates a quite large tuning of T_c by changing the growth angle from 0^o to 54.7^o. When the growth angle increases from 54.7^o to 87^o, BTO films undergo a transition from p phase to r_{aa} phase (in which the polarization has a non-zero and equal x- and y-components and a smaller z-component) as the temperature decreases. The resultant T_c increases from 295K to 385K. Finally, when the growth angle rotates from 87^o to 90^o (that is near the pseudo-cubic [110] direction), a p-to-aa-to-r_{aa} phase transition sequence occurs as the temperature decreases as similar to the case of (110) BTO films.

One interesting feature about this phase diagram is that there is a r phase below 295K at

exactly $\theta = 54.7^o$, where the growth direction coincides with the pseudo-cubic [111] direction. The polarization also lies along the pseudo-cubic [111] direction as in the ground state of bulk BTO. At this special growth direction, Tc reaches its minimum at 295K (near room temperature), which can be, e.g., put into use to design devices having large dielectric tunability near room temperature (see, e.g., Ref. [57] and references therein).

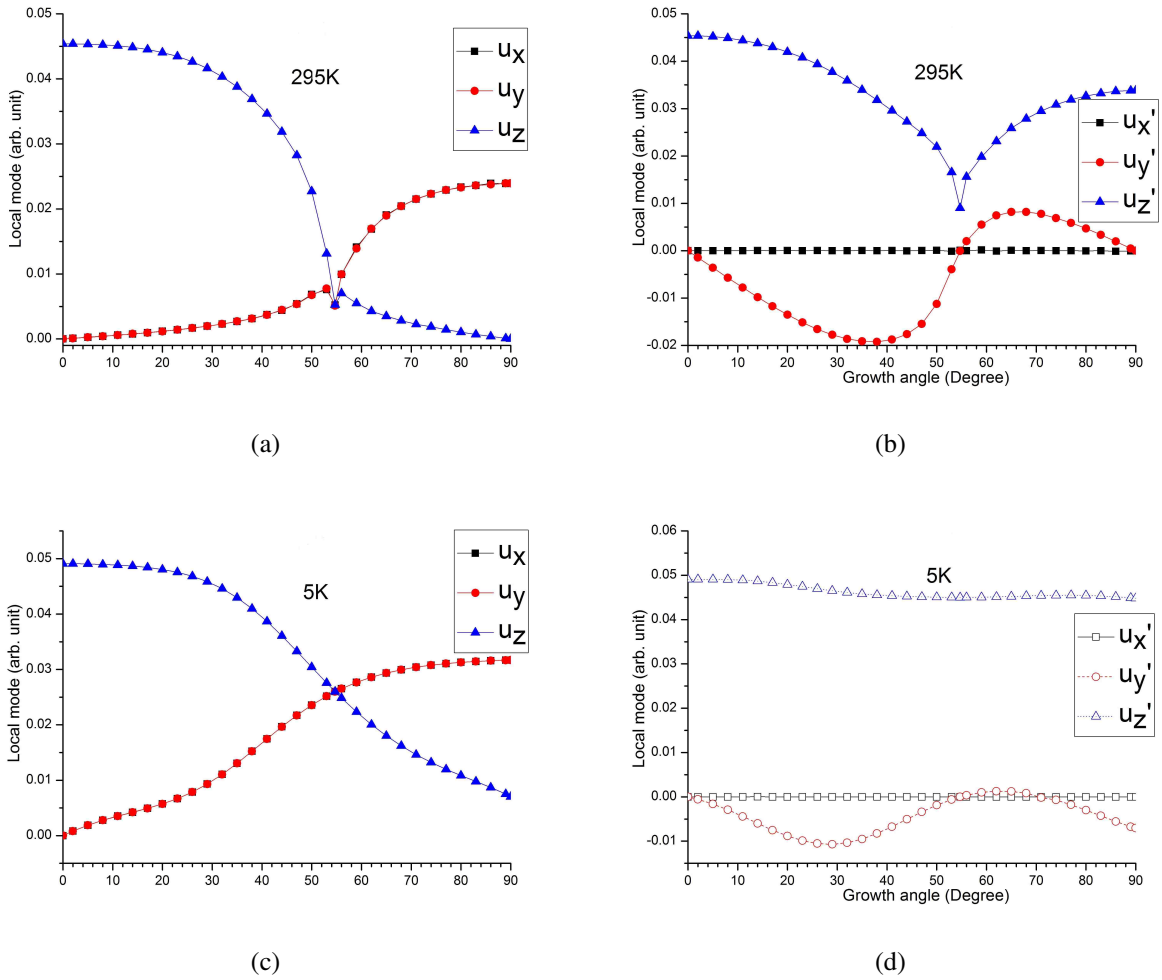

Figure 3.6: Structural properties of BTO films grown on a STO substrate as a function of the growth angle. Panels (a) and (b) display the components of the supercell average of the local mode in the (xyz) and (x'y'z') coordinate frame, respectively, at 295K. Panels (c) and (d) provide similar data than Panels (a) and (b), respectively, but for a temperature of 5K.

Then let us study the behavior of the polarization at this minimum Tc which are displayed in Figs. 3.6a (in the (xyz) frame) and 3.6b (in the (x'y'z') frame). When the growth angle starts at 0^o, only the z-component is there and the polarization is totally out of plane (see Fig.

3.6b). Then x- and y-components appear and rise slowly in equal magnitudes, meanwhile the z-component similarly decreases slowly, which leads to the r_c phase. This is shown in the (x'y'z') frame by the rising of an in-plane component and decreasing of the out-of-plane component until the growth angle of 38^o. From 38^o to 54.7^o, both the in-plane components decrease fast to zero, which lefts only the out-of-plane component of the polarization. When the growth angle increases from 54.7^o to 90^0, the x- and y-components continue to increase, while the z-component decreases further. At 90^o, the z-component disappears and the in-plane y'-component again disappears. Notice that the x'-component of the polarization remains zero during the whole range. This is in line with the geometry of the epitaxial growth direction as a manifestation of the strong interaction between the polarization and strain. The polarization at 5K shows similar behaviors. If we describe these behaviors in terms of the rotation of the polarization vector, the polarization first rotates away from the growth direction, then back toward the growth direction, then away from the growth direction, and then back towards the growth direction, which manifests as large responses between around 40^o to 60^o from all normal components of the dielectric constants and relevant components of piezoelectric coefficients as shown in Figs. 3.7. For instance, $d_{33}^{'}$ and $d_{24}^{'}$ peak and adopt rather large values when θ is close

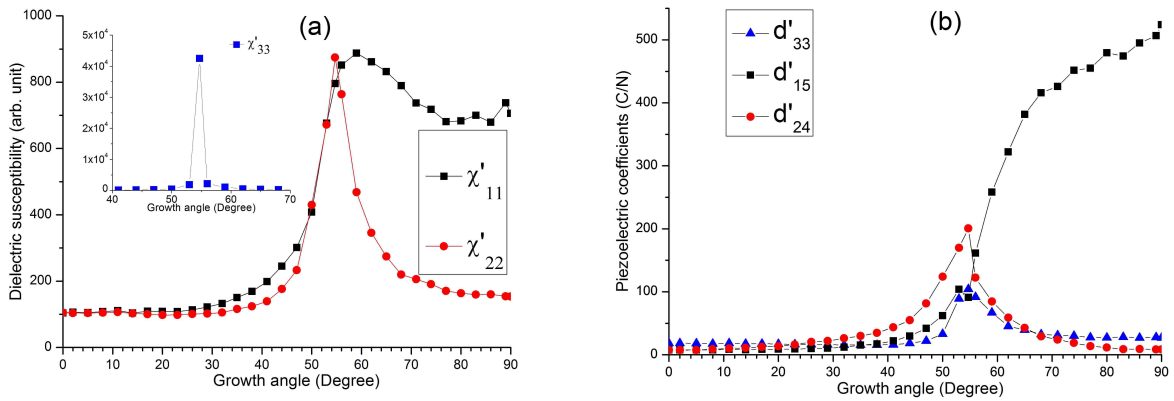

(a) (b)

Figure 3.7: Physical responses of BTO films grown on a STO substrate as a function of the growth angle, at a temperature of 295K and within the (x'y'z') coordinate frame. Panel (a) reports the $\chi_{11}^{'}$ and $\chi_{22}^{'}$ components of the dielectric susceptibility, with its inset giving $\chi_{33}^{'}$. Panel (b) displays the $d_{33}^{'}$, $d_{15}^{'}$ and $d_{24}^{'}$ piezoelectric coefficients.

to 54.7^o. And $\chi_{33}^{'}$ is larger than 10,000 and $d_{24}^{'}$ is bigger than 200 pC/N when $\theta = 54.7^o$. Such

behaviors are very promising to design efficient miniaturized devices at room temperature. However, the large and unusual tails in χ'_{11} (i.e., values larger than 700) and d'_{15} (as large as 500 pC/N) when the growth angle is increased above 54.7^o and up to 90^o near room temperature, remain to be further explained. In fact, such technologically-relevant and striking features arise from the easiness of the spontaneous polarization to rotate within the (x', z') plane via, e.g., the application of external electric field or stress [13, 58]. Such easiness is consistent with the fact that Ref. [46] predicted that (110) BTO films experiencing a misfit strain of around -2.2% lie, at 295K, near the edge of a phase transition towards the ab phase, for which the polarization vector is in-between our x'- and z'- directions, that is in-between the pseudo-cubic $[\bar{1}10]$ and [110] directions (see Fig. 3.1).

After all the discussions above, it will be illuminating to do a short comparison of the phase diagram in Fig. 3.5 and in Fig. 3.8 (corresponding to (001) BTO films as a function of misfit strain obtained by the same effective Hamiltonian). Clearly, they bear a lot of resemblances. First, T_c can be tuned, although variation of growth directions acts more efficiently in the turning. Second, low-symmetric phases emerge at low temperature. Thus, one can conclude that

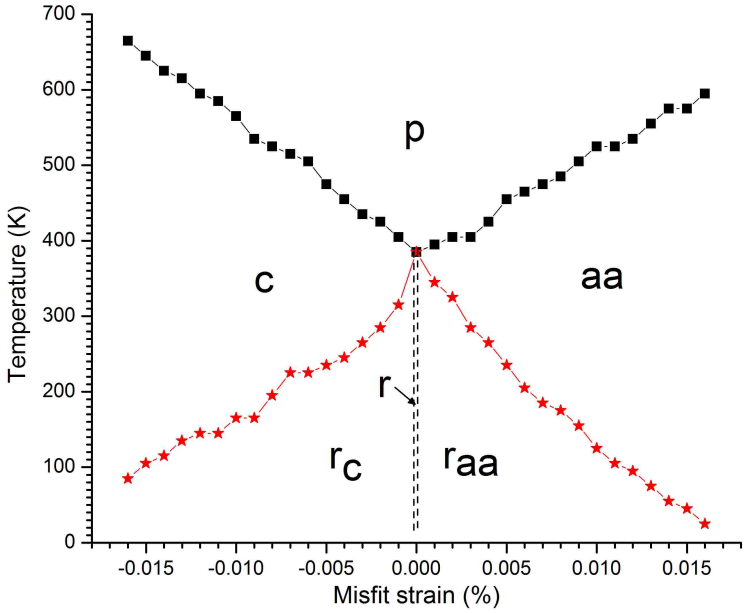

Figure 3.8: The predicted temperature-versus-misfit strain phase diagram of (001) BTO: The phases displayed in the diagram are explained in the text.

the method proposed here demonstrates its equivalence of the conventional growth method of BTO films, i.e., (001) epitaxial BTO films. In other words, by "continuously" varying the growth direction, we may get a specifically targeted Tc, which is mostly beyond the capability of the conventional way (since the number of suitable substrates are limited).

Finally, there is still one issue that remains to be addressed: it is the T_C behavior in Fig. 3.5. As indicated above, there is a strong interaction between the polarization and epitaxial strain, meanwhile the polarization is related to Tc (according to the ϕ^4 model mentioned in last section), and the geometry of the growth direction affects the epitaxial strain. So there is a link between the geometry of the growth direction and T_c. One may wonder whether this directional minimization of Tc (i.e., lowest Tc for the pseudo-cubic [111] direction) is more likely material-dependent or geometry-dependent. To check this, similar calculations are performed on another typical ferroelectrics, $PbTiO_3$ (PTO). The phase diagram of PTO is shown in Fig. 3.9. Clearly, PTO films also gains its T_c minimum when the growth direction aligns with the pseudo-cubic [111] direction. PTO is totally different from BTO in many ways. For example, PTO adopts a single ferroelectric phase, c phase below 765K, while BTO undergoes a series of

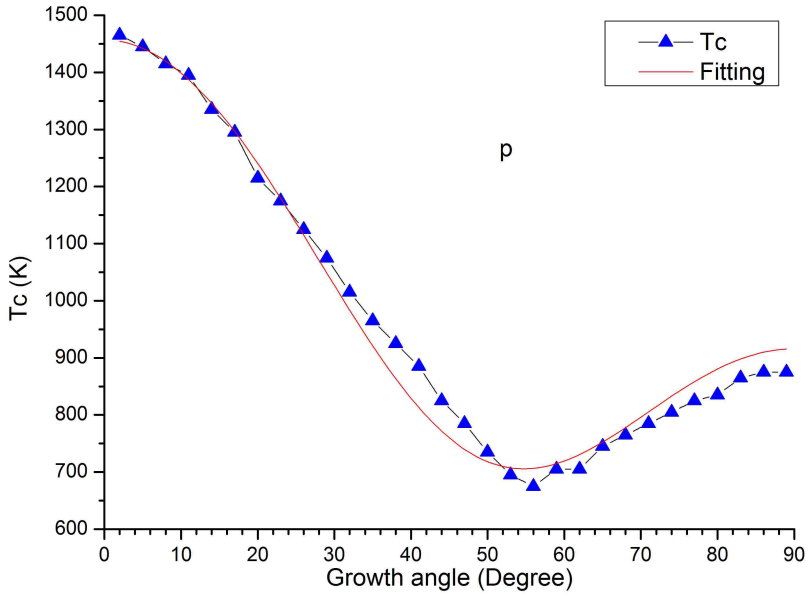

Figure 3.9: The temperature-*versus*-growth angle phase diagram of PTO films grown on a substrate at a -1.6% compressive strain as a function of the growth angle. The solid red line represents the fitting of T_c by Eq. 3.8.

phase transitions, p-to-c-to-aa-to-r, when the temperature is reduced below 405K. Given such differences, still both T_c of these two ferroelectrics reach their minima at the pseudo-cubic [111] direction. Therefore, it appears that the directional minimum of T_c is material independent. To check it, a phenomenological model is developed. The internal energy provided by the effective Hamiltonian of BTO systems can be expressed as a sole function of the z'-component of the supercell average of the local modes, $u_{z'}$, which is the dominant component. In other words, we neglect, in a first approximation, the other $u_{x'}$ and $u_{y'}$ components of the local modes (as rather consistent with Figs. 3.6c and 3.6d), and the magnitude of local modes simply reduces to $u_{z'}$. We found that the analytical expression of the energy of this H_{eff}, as well as the values of its parameters, allows to rewrite the total internal energy as:

$$E_{tot} = \kappa {u_{z'}}^2 + \beta {u_{z'}}^2 + \alpha_e {u_{z'}}^4 + \gamma_e (sin(\theta)^2 - \frac{3}{4} sin(\theta)^4) {u_{z'}}^4, \tag{3.6}$$

where κ is the quadratic coefficient solely associated with the polarization and that is independent of θ. The β coefficient includes (1) the effective parameters quantifying the interaction between strains and local modes, and thus depends on both θ and the epitaxial strain, and (2) the effective parameters capturing the dipole-dipole interactions which are independent of θ and of the epitaxial strain. Practically, β is found to be of the form:

$$\beta = sin(\theta)^2 (4 - 3sin(\theta)^2) L + K, \tag{3.7}$$

where L and K adopt complicated expressions that contain the epitaxial strain but have rather minor dependences on the growth angle. The α_e and γ_e coefficients of Eq. 3.6 are found to be positive and negative, respectively, and almost independent of θ for the BTO system. Minimizing Eq. 3.6 with respect to $u_{z'}$ and assuming that T_c is proportional to the square of $u_{z'}$ (as consistent with the Φ^4 model) therefore results in:

$$T_c \simeq \frac{M}{\alpha_e + \gamma_e (\sin(\theta)^2 - \frac{3}{4} \sin(\theta)^4)} + N, \tag{3.8}$$

where M and N only weakly depend on θ and are both positive. Then both T_c of BTO and PTO are fitted to the Eq. 3.8. As shown by red solid lines in Figs. 3.5 and 3.9, the fittings are actually quite good. However, in Eq. 3.8 several parameters are material dependent, e.g., the relative signs of α_e, γ_e and M. These parameters combine to render a minimum of T_c at the

pseudo-cubic [111] direction. For ferroelectrics that have polarization as the single long-range order parameter like BTO and PTO here, it is thus likely to be universal that a minimum of T_c occurs at the pseudo-cubic [111] direction as consistent with Eq. 3.8.

So far, the effects of the growth direction on the static properties of ferroelectric BTO films have been presented throughout this chapter. First, it has been shown in (110) BTO films (i) the existence of low-symmetry phases (including three monoclinic ones and an unusual triclinic phase); (ii) that, near room temperature, there are a series of novel phase transitions: starting from an aa state (orthorhombic phase) in the far compressive strain region, then passing through an ab state (monoclinic phase) and an abc state (triclinic phase) by second order transitions in the near region of 0.0% strain, and finally turning into a r_c state (which is another different monoclinic phase) by a first order transition; (iii) that the fast strain-induced rotation of the polarization associated with these latter transitions results in huge dielectric and piezoelectric responses, which is very promising to design efficient miniaturized lead-free devices; (iv) that one can easily switch between different polarized states by applying in-plane and out-of-plane electric fields, which is promising for the design of novel memory devices; and (v) that the Curie temperature in the compressive strain region is nearly independent of the epitaxial strain. Items (i)-(v) all differ from features previously seen in (001) BTO films, and are obviously of fundamental and technological importance. Next, another study was devoted to films made of the most famous ferroelectric system (namely, $BaTiO_3$) grown on the most famous *single* substrate (i.e., $SrTiO_3$) by varying the crystallographic direction (away from the pseudo-cubic [001] direction) of the growth axis. This method is proposed to overcome an inevitable limitation that arises from the fact that there are few available substrates and therefore the magnitude and sign of the epitaxial strain that ferroelectric films can experience are scarce. Our findings include: (i) an original temperature-versus-growth angle phase diagram possessing different structural states; (ii) a tuning of the Curie temperature, T_c, by more than 450K; (iii) a minimal value of T_c being *near room temperature*; (iv) optimization of important physical responses at room temperature, such as dielectric and piezoelectric coefficients, for some specific growth directions; (v) explanations of the origin of these features, including the finding of a simple law correlating T_c with the growth direction (see Eq. 3.8). Items (i) clearly shows the alterna-

tive procedure offered by our proposed method with respect to the usual way of growing (001) films on top of *various* substrates, by equivalently offering a phase diagram possessing different structural states. Items (ii)-(v) demonstrate the advantages of our proposed method by offering a rather "continuous" tuning of T_c (including near room temperature) and other properties (e.g., substantial *room-temperature* dielectric and piezoelectric responses), which are also obviously of technological importance. Moreover, our first-principles-based approach provides a deep microscopic understanding of these novel features.

Chapter 4

Finite-temperature dynamical properties of (Ba, Sr)TiO_3 nanocomposites

Background

Ferroelectrics (FE) exhibit an abundant variety of phenomena ranging from rich structural phase transitions to complex magnetic configurations and topological defects. Although *ferroelectric* vortices, or related flux-closure configurations, have been predicted to exist ten years ago [59], they have been only observed more recently [60, 61, 62, 63, 64, 65, 66, 67, 68, 69, 70]. On the other hand, vortices in superconductors and superfluids are still very active topics that have been studied since the middle of last century [71, 72]. In particular, magnetic vortices have been investigated a lot during the past two decades (see Refs. [73, 74] and references therein). Unlike dynamics of magnetic vortices, studies about *dynamics* of ferroelectric (FE) vortices are quite rare. One may expect that FE vortices have the potential to be more advantageous than magnetic vortices for ultrafast and high-density storage devices, due to the facts that their dynamics may be in the THz regime (since phonons' frequencies are typically in this regime) and that they are smaller in size compared to magnetic vortices which dynamics is known to be mainly restricted to the GHz regime [75, 76, 77, 78]. A lot of questions remains therefore unknown about this electric topological defect. For instance, what are the relations between dynamics of an electric vortex as a whole and (dielectric) dynamics of the individual electric dipoles forming such vortex? In particular, is there any mode operating in the THz regime that is associated with the formation of FE vortex and that softens with temperature, as similar to the soft or central mode for the polarization dynamics of typical ferroelectrics [79, 80, 81, 82]? If yes, what kind of mode is that? In light of these issues, we use a first-principles-based effective Hamiltonian to reveal dynamics of $BaTiO_3$ nanowires embedded in a less polar matrix, which

has been originally reported in Ref. [92]. This nanocomposite undergoes a series of complex phases. When the temperature drops below a critical temperature that we denote as T_t, electric vortices form and a spontaneous electrical toroidal moment appears.

Method and System

The method used in this study is the effective Hamiltonian for BST systems implemented in a Molecular Dynamics (MD) algorithm. MD has been vastly applied in many different systems in Physics, Chemistry and Biology. It has proven to be very efficient in modeling the dynamical properties of a many-body system within classical mechanics description. The details procedures of MD algorithm can be found in many reviews and books (e.g., Ref. [83]). Its outline is simply presented here.

As an introduction, we will present it with a case with one type of degree of freedom. Of course, it is very straightforward to extend it to multiple types of degrees of freedom depending on what the simulations are aimed at. Suppose the model system contains N particles with their displacements given by $\{\mathbf{u}_i$, i=1,...N$\}$. The next thing needed is an accurate description of the particle-particle interaction H($\{\mathbf{u}_i, i = 1, ...N\}$). The consecutive discrete times are denoted by $\{$t=0, 1, 2, ..., t, ...$\}$. Initially (at time $t = 0$), the displacements of all the particles are given. The choice of the initial configuration is trivial but cannot be arbitrary, especially if the simulation is carried out within NVE ensembles of which the total particle number, the whole volume and the total energy are constant. Precisely, the chosen initial configuration shall be compatible with the desirable macrostate that is studied. Now what is required is the dynamical equations that govern their motions with respect to time. Generally, the dynamics equations will follow Newton's law in classical mechanics:

$$m_i \frac{d^2 u_{i,\alpha}}{dt^2} = -\frac{\partial H}{\partial u_{i,\alpha}}, i = 1, ...N, \tag{4.1}$$

where m_i is the assigned mass for particle i and α denotes Cartesian components. From this, the velocity $\dot{\mathbf{u}}_i$ and acceleration $\ddot{\mathbf{u}}_i$ of particle i are obtained numerically at each time. Based on the velocities and accelerations at time t, the displacements at the next time $(t + 1)$ are readily calculated through some numerical integration techniques. This process should continue

for time long enough with respect to the characteristic time scale of the targeted dynamical properties. At the end, the macroscopic quantities of interests are obtained through statistical mechanics. At each step, the produced configuration is one microstate in the phase space of the system. As it is shown in Hamiltonian mechanics, the total energy here is conserved. So, the discussion above corresponds to NVE ensemble. However, in most cases, instead of fixed energy E or fixed volume V, the temperature T or pressure P is kept fixed which are more realistic in experiments and called NVT (canonical) or NPT (isothermal-isobaric) ensembles. However, the temperature T or pressure P isn't naturally conserved from the equation of motion. Therefore, additional modifications of Eq. 4.1 should be included. Such modifications are referred as thermostat (for NVT ensemble) and barostat (for NPT ensemble). One famous thermostat is the Nosé-Hoover algorithm. One barostat can be found in Ref. [84].

In our study, the system under investigation is four equisized BTO nanowires embedded equispacedly in a large STO matrix. A recent study shows that below T_t (330K) this nanocomposite makes a transition from paraelectric and paratoroidic phase to paraelectric and toroidic phase as indicated by a vanishing net polarization and non-trivial vortex-pattern dipole configurations inside BTO wires [85]. The toroidic phase is characterized by a spontaneous electrical toroidal moment of each wire calculated as in Refs. [59, 86]:

$$\boldsymbol{G} = \frac{1}{2N_w} \sum_{i=1}^{N_w} \boldsymbol{r}_i \times \boldsymbol{d}_i, \tag{4.2}$$

where $\boldsymbol{r}_i$ is the position vector (with respect to a chosen origin) and $\boldsymbol{d}_i = Z^* \boldsymbol{u}_i$ is the dipole moment of the 5-atom cell *i*, with Z^* being the Born effective charge. N_w is the total number of cells within each associated wire. A non-vanishing z-component of $\boldsymbol{G}$ appears below T_t as a result of the formation of electric vortices in the (x,y) planes of each wire (see Fig. 4.1).

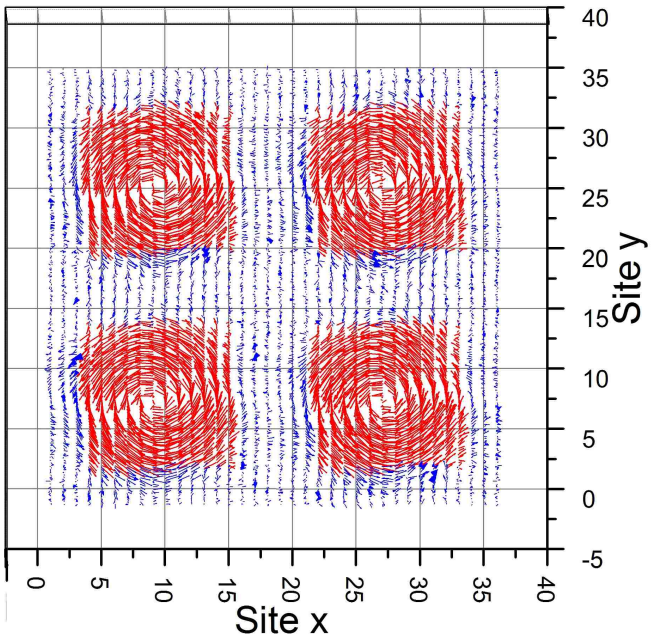

Figure 4.1: This figure shows the dipolar configuration (averaged over 50 snapshots at the same temperature) occurring in the (x,y) plane of the investigated nanocomposite for any temperature ranging between $T_C \simeq$ 240K and $T_t \simeq$ 330K. The areas in red and blue are BTO wires and STO matrix, respectively.

Technically, we first run $3.0\times\ 10^5$ MD steps of NPT (isothermal-isobaric ensemble) simulations on a $36 \times 36 \times 6$ supercell (38,880 atoms) to equilibrate the system and then another equilibration within the NVE (microcanonical) ensemble is done through $3.0\times\ 10^5$ MD steps. Finally, additional $8.2\times\ 10^6$ MD steps are performed within this NVE ensemble to collect time-resolved properties of the system. Typical outputs, at any MD step, are the local modes and the electric toroidal moment defined in Eq. 4.2. To extract the dynamic properties, the approach similar to that used in Refs. [79, 87, 88] is employed to compute two different complex responses *versus* frequency, ν, for each investigated temperature and in any of the four nanowires. One response is the dielectric permittivity, which is calculated via:

$$\varepsilon_{\alpha\beta}(\nu) = 1 + \frac{1}{\varepsilon_0\, V_w k_B\, T} \int_0^\infty [d_\alpha(t) d_\beta(t) + i2\pi\nu e^{i2\pi\nu t} < d_\alpha(t) d_\beta(0) >] dt,$$
$$d_\alpha = \frac{1}{4} \sum_i Z^* u_{i,\alpha}, \quad \text{with } i \text{ running over all sites in the wires,} \tag{4.3}$$

where α and β denote Cartesian components. $\boldsymbol{d}(t)$ is the average total dipole moment of the wires at time t and $< d_\alpha(t) d_\beta(0) >$ is the autocorrelation function associated with dipole

moment [83, 87]. V_w is the volume of each wire within this supercell, T is the temperature and ε_0 is the vacuum permittivity. The other is the response function of the toroidal moment to its conjugate field (that is, a curled electric field [89, 90, 91, 9]) and is defined as:

$$\varepsilon_{t,\alpha\beta}(\nu) = 1 + \frac{1}{\varepsilon_0 V_w k_B T} \int_0^\infty [G_\alpha(t) G_\beta(t) + i2\pi\nu e^{i2\pi\nu t} < G_\alpha(t) G_\beta(0) >] dt, \tag{4.4}$$

where $\boldsymbol{G}(t)$ is the electric toroidal moment vector averaged over all the four wires at time t and $< G_\alpha(t) G_\beta(0) >$ is the autocorrelation function associated with that toroidal moment. α and β denote Cartesian components. The computed spectra of $\varepsilon_{\alpha\beta}(\nu)$ and $\varepsilon_{t,\alpha\beta}(\nu)$ are then fitted by classical damped harmonic oscillators $\frac{S\nu_r^2}{\nu_r^2 - \nu^2 + i\nu\gamma}$, where ν_r, γ and S are the resonant frequency, damping constant and strength of the oscillator, respectively. $S{\nu_r}^2$ gives the spectral weight. The details of this work is reported in Ref. [92].

Dynamics of electric vortices formation

First, let us take a look at the complex spectra of two dielectric tensor components, $\varepsilon_{xx}(\nu)$ and $\varepsilon_{t_{zz}}(\nu)$ at two different temperatures. One is at 750K in the high temperature region and the other is 450K closer to the transition temperature T_t. As shown in Ref. [85], the four wires behave in phase and the inter-wire interactions are weak. Thus, it is reasonable to use the average of all the four wires for $\mathbf{d}(t)$ and $\mathbf{G}(t)$. Fig. 4.2a shows that there is a single mode at 750K, while there are two apparent modes at 450K. And this crossover from one mode to two modes regime occurs at around 670K. A similar crossover was reported in the paraelectric phase of bulk BTO [79]. The high frequency mode was referred to be the soft mode, while the low frequency branch was identified as the central mode. One more thing worth mentioning is that the high frequency modes in $\varepsilon_{zz}(\nu)$ and $\varepsilon_{t_{xx}}(\nu)$ occur at close frequencies. However, the low frequency modes at 450K behave differently. To understand it, we will turn to Fig. 4.3, which shows the temperature evolution of the resonant frequencies extracted from $\varepsilon_{zz}(\nu)$ and

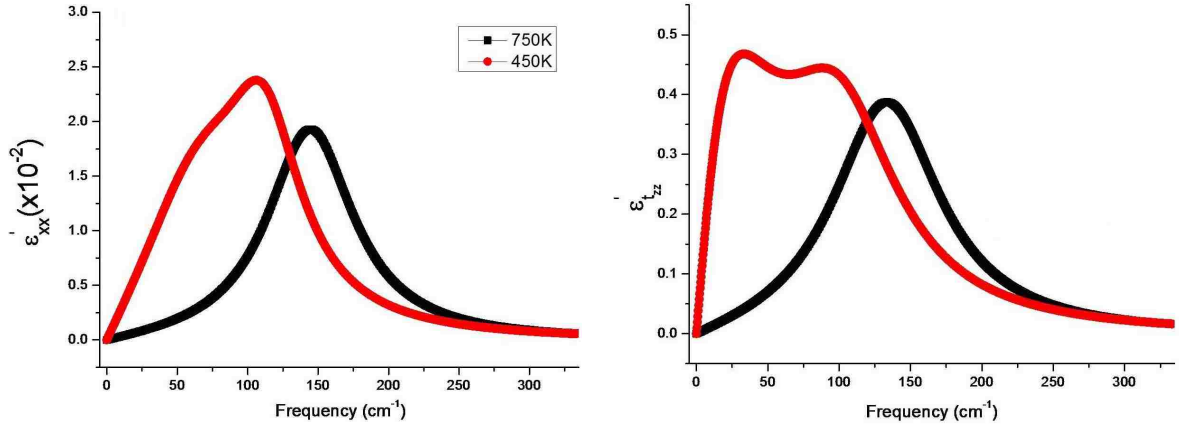

(a) (b)

Figure 4.2: Imaginary parts of the responses of the x-component of the averaged dipole moment (Panel a) and the z-component of the electric toroidal moment (Panel b) inside the wires, as a function of frequency and as fitted by classical harmonic oscillators, for 450K and 750K.

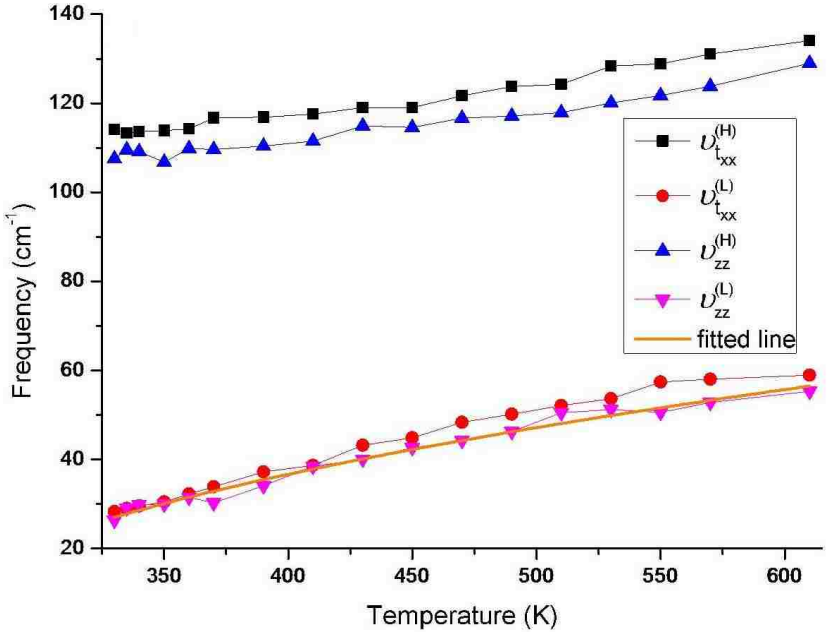

(a)

Figure 4.3: Characteristic dynamical properties of the studied nanocomposite as a function of temperature: the resonant frequencies of the complex responses of both the x-component of the toroidal moment and of the z-component of the averaged dipole moment inside the wires. The thicker solid line shows the fit of some data by square-root laws that are indicated in the text.

$\varepsilon_{t_{xx}}(\nu)$ by fitting to classical damped harmonic oscillators. In the whole temperature window, each of the spectra has two modes at present, a high frequency one labelled by "H" and a low

frequency one labelled by "L". The high frequency branch of $\varepsilon_{zz}(\nu)$ (to be denoted as $\nu_{zz}^{(H)}$) smoothly softens when temperature decreases from 630K to T_t ($\simeq$ 330K) up to which no net polarization or toroidal moment has formed. Compared to the two modes in the paraelectric phase of bulk BTO, this high frequency branch $\nu_{zz}^{(H)}$ corresponds to soft mode, thus it characterizes dipole moments' oscillating. The low frequency branch of $\varepsilon_{zz}(\nu)$ (to be denoted as $\nu_{zz}^{(L)}$), however, softens much faster, which is identified as the central mode. It captures the motion of the dipole moment fluctuation between energetic wells that are close enough. The existence of these two modes is associated with an order/disorder type of transition and is well explained by a Comes-Guinier-Lambert model [80, 93]. And it fits well to a square-root law of the form $C(T - T_{FE})^{1/2}$, where T_{FE} is fitted to be around 247 K. Such result is consistent with the formation of a net *spontaneous polarization lying along the z-axis* for a critical temperature $T_C \simeq$ 240 K [85]. Meanwhile, the two modes from $\varepsilon_{t_{xx}}(\nu)$ are displayed together, and are denoted as $\nu_{t_{xx}}^{(H)}$ and as $\nu_{t_{xx}}^{(L)}$, respectively. For the temperature range here, the high frequency branch $\nu_{t_{xx}}^{(H)}$ from the x-component of the toroidal moment follows the high frequency branch $\nu_{zz}^{(H)}$ from the z-component of the dipole moment, and the low frequency branch $\nu_{t_{xx}}^{(H)}$ from the x-component of the toroidal moment follows the low frequency branch $\nu_{zz}^{(H)}$ from the z-component of the dipole moment. If we take a look at Eq. 4.2, this can be easily understood through the fact that the x- component of the toroidal moment involves the y- and z- components of the dipole moment. Therefore, when there is no formation of toroidal moment (i.e., G_x here), the two modes from $\varepsilon_{t_{xx}}(\nu)$ result from the conventional dynamical modes of the involved component of the total dipole moment, i.e., the soft mode and central mode. In other words, there is no significant individual mode that solely belongs to the toroidal moment. Now let us see what happens when there is formation of a net toroidal moment below T_t.

Figure 4.4a shows the resonant frequencies of the complex responses of the z-component of the toroidal moment and of the x-component of the averaged dipole moment inside the wires. The resonant frequencies of $\varepsilon_{yy}(\nu)$ are not shown here since the spectra from $\varepsilon_{yy}(\nu)$ is identical to that of $\varepsilon_{xx}(\nu)$. The high frequency branch of $\varepsilon_{xx}(\nu)$ (denoted as $\nu_{xx}^{(H)}$)) shares the same temperature evolution as $\nu_{zz}^{(H)}$ discussed above, only with a difference in their magnitudes (such difference is due to the nonequivalency between the x- and z-components of the dipole

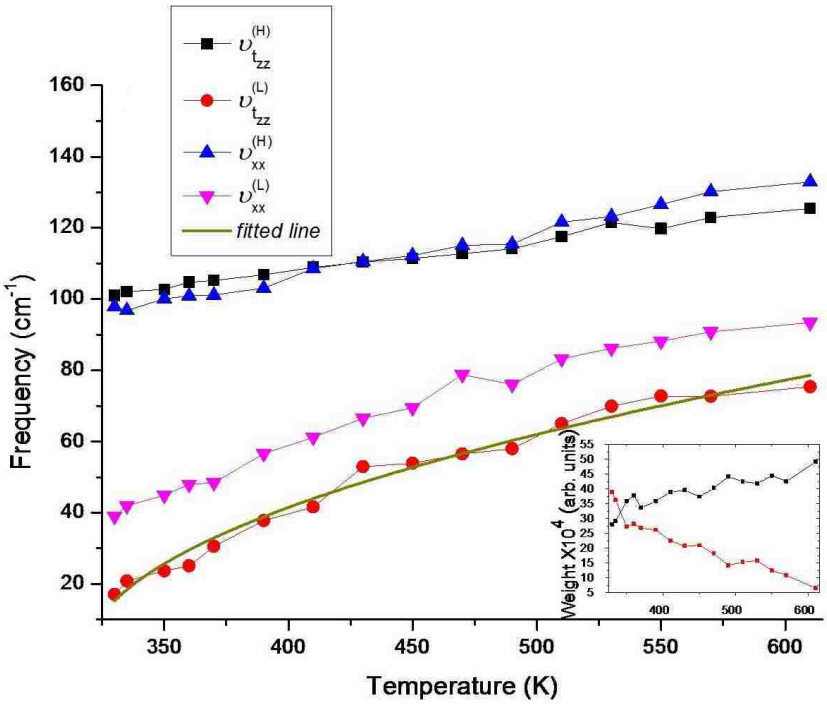

(a)

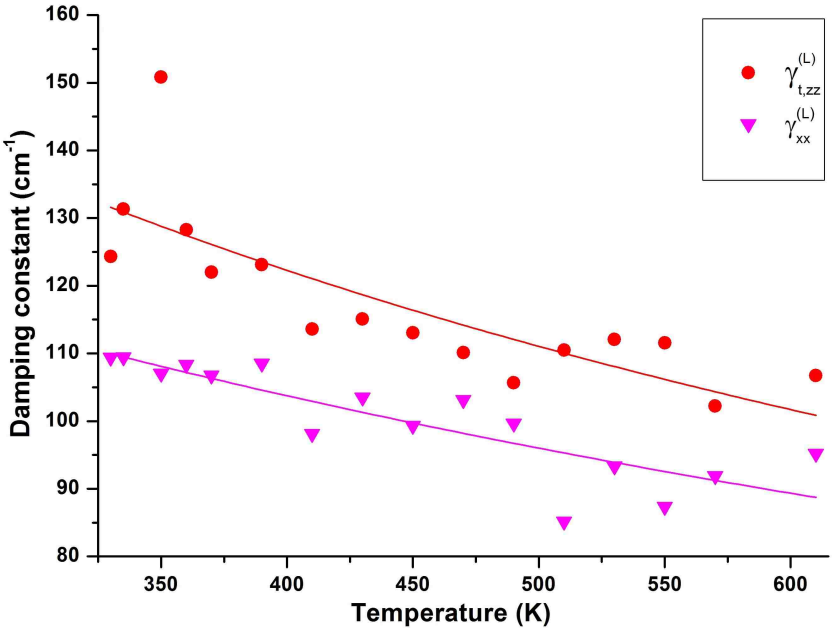

(b)

Figure 4.4: Characteristic dynamical properties of the studied nanocomposite as a function of temperature: Panel (a) displays the resonant frequencies of the complex responses of the z-component of the toroidal moment and of the x-component of the averaged dipole moment inside the wires. The inset of Panel (a) represents the spectral weight of the low-frequency and high-frequency modes associated with the fluctuation of the z-component of the toroidal moment, while Panel (b) displays the damping coefficients of these two latter modes. The thicker solid line of Panel (a) shows the fit of some data by the square-root law that is indicated in the text. The solid lines of Panel (b) are guides for the eyes.

moment). Just like $\nu_{zz}^{(H)}$ and $\nu_{t_{xx}}^{(H)}$, the high frequency branch $\nu_{t_{zz}}^{(H)}$ follows closely $\nu_{xx}^{(H)}$ due to the fact that the x-component of the dipole moment enters the z-component of the toroidal moment through Eq. 4.2. Since this high frequency mode $\nu_{xx}^{(H)}$ corresponds to the oscillation of the dipole moment along the x-direction, the high frequency mode $\nu_{t_{zz}}^{(H)}$ captures the oscillations of the z-component of the toroidal moment due to the oscillation of the dipole moment along the x- and y-directions. However, unlike $\nu_{zz}^{(L)}$ and $\nu_{t_{xx}}^{(L)}$, the low frequency branches $\nu_{xx}^{(L)}$ and $\nu_{t_{zz}}^{(L)}$ soften faster while they significantly differ from each other when the temperature decreases towards T_t. The gap between $\nu_{xx}^{(L)}$ and $\nu_{t_{zz}}^{(L)}$ is around 20 cm^{-1}, which is beyond a statistical error. Besides, the damping constants for these two low frequency branches are displayed in Fig. 4.4b, which shows the large difference between them. Clearly, the damping constant of the toroidic mode is larger, which means the relevant motion of the toroidal moment damps faster and there exists large anharmoncity in it. This is easily understood considering the fact that toroidal moment involves a large portion of dipole moments which will result in larger anharmonicity. On the other hand, we also numerically found (not shown here) that the damping coefficients of the low-frequency (and also high-frequency) toroidic and dielectric modes, whose resonant frequencies are shown in Fig. 4.3, are basically identical. All of these suggest that this low frequency $\nu_{t_{zz}}^{(L)}$ is a distinct mode solely associated with the toroidal moment. The thicker solid line represents the fitting of $\nu_{t_{zz}}^{(L)}$ to the square-root law of the form $C(T-T_{tor})^{1/2}$. T_{tor} is fitted to be around 319K here, which is very close to T_t ($\simeq 330K$). The difference between this critical temperature T_{tor} and the reported T_t in Ref. [85] is within the typical error of transition temperatures when going from Monte-Carlo simulations (as done in Ref. [85]) to MD calculations (as used here). Further, the inset of Fig. 4.4b gives the spectral weights of the two modes of $\varepsilon_{t_{zz}}(\nu)$. With the temperature decreasing toward T_t, the spectral weight of the high frequency mode decreases, and the spectral weight of the low frequency mode increases and becomes increasingly important. Therefore, this low frequency mode $\nu_{t_{zz}}^{(L)}$ should be responsible for the transition from paratoroidic phase to ferrotoroidic phase, which also confirms that the z-component of toroidal moment is a good order parameter in this transition.

As we discussed earlier, the low frequency dielectric modes $\nu_{xx}^{(L)}$ and $\nu_{zz}^{(L)}$ are identified as the central modes which characterizes the hopping of the dipole moment between energetic

wells. Then what kind of motion is the low frequency toroidic mode $\nu_{t_{zz}}^{(L)}$ related to? To answer this question, let us first turn back to Eq. 4.2. In the definition, the toroidal moment consists of the cross product of the individual dipole moments and the position vector. Since we collect our complex dielectric spectra in micro-canonical (NVE) ensemble, it means that the position vectors are held fixed at this stage of simulations. The oscillation of the magnitude of the dipole moment has already entered into the toroidic spectra as exhibited by the high frequency branch $\nu_{t_{zz}}^{(H)}$. Then what are left of the cross product of the individual dipole moments and the position vectors are the individual angles between the individual dipole moments and their position vectors. So the angular fluctuation in the cross product is expected to be the origin of the low frequency toroidic mode $\nu_{t_{zz}}^{(L)}$. To confirm it, we performed another set of calculations of which the results are shown in Fig. 4.5. In this set of calculations, we computed the average of the projected local electric dipole at each site i onto its *azimuthal* direction. These azimuthal directions are displayed for several unit cells in the inset of Fig. 4.5. Let us now sum these azimuthal components over all the sites belonging to a wire, and denote the resulting quantity as $d_{azi}(t)$ for any time step, t, of the MD procedure. One is then able to compute an "azimuthal" response given by:

$$\varepsilon_{azi}(\nu) = 1 + \frac{1}{\varepsilon_0 V_w k_B T} \int_0^\infty [d_{azi}(t) d_{azi}(t) + i 2\pi\nu e^{i2\pi\nu t} < d_{azi}(t) d_{azi}(0) >] \, dt. \quad (4.5)$$

This latter response is thus deduced from the "traditional" dielectric response of Eq. 4.3 by replacing the Cartesian components of the local electric dipoles by their azimuthal components. This azimuthal response is then fitted by classical damped harmonic oscillators. The resulting resonant frequency, $\nu_{azi}^{(L)}$, of the lowest-in-frequency azimuthal mode is then plotted as a function of temperature in Fig. 4.5, along with the resonant frequency $\nu_{t_{zz}}^{(L)}$ that is associated with the fluctuation of the z-component of the toroidal moment. These two frequencies coincide well for any investigated temperature. One can thus safely conclude that the dynamics of the low-frequency toroidic mode displayed in Fig. 4.4a corresponds to fluctuation of the (collectively organized) azimuthal components of the local electric dipoles. This low-frequency toroidal mode can be thought as being analogous to a *pendulum* and *rotational* displacements, rather than classical springs that are associated with translational displacements (as the other investigated toroidic and dielectric modes correspond to) [94]. This azimuthal oscillation also

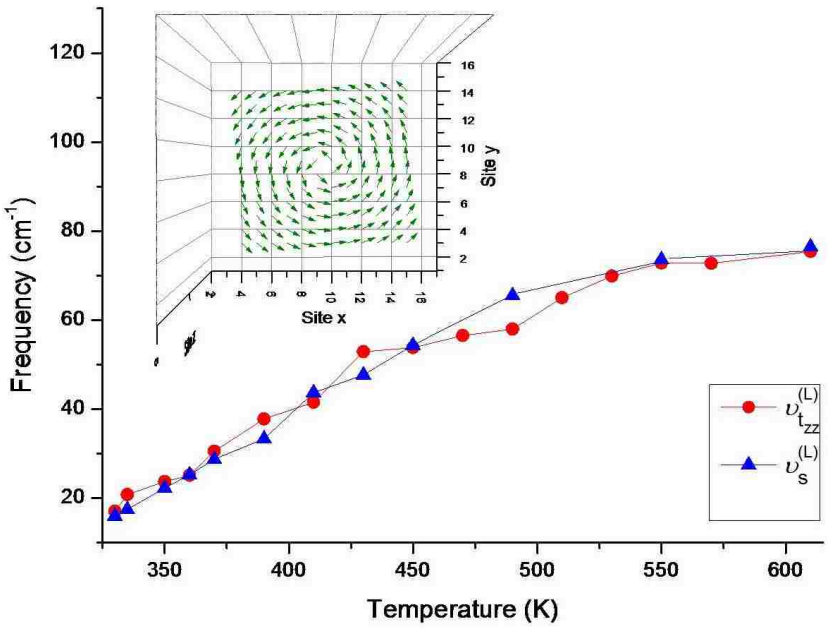

(a)

Figure 4.5: Temperature evolution of the resonant frequency of the low-frequency mode associated with the azimuthal response defined by Eq. 4.5, along with that of the low-frequency mode of the response of the z-component of the toroidal moment. The inset illustrates the azimuthal direction (which the arrows point towards) of each site position (where the tail of each arrow is located at) in a wire.

bears resemblance with the azimuthal motions of spin waves associated with magnetic vortices [78]. We also plot the probability distribution of the three components of the toroidal moment at 325K near the transition temperature T_t. Clearly, three is only one peak for G_x and G_y around zero, while there are two large peaks around ± 0.025 from G_z, which suggests a significant oscillation of the rotational displacement between energetic wells when there is a net toroidal moment component (G_z) going to form. This is captured in the lowest frequency mode $\nu^{(L)}_{t_{zz}}$.

In summary, this chapter presents a study of the dynamical mechanisms of the toroidal moment in a electrotoroidic system which consists of BTO wires embedded in STO matrix by the method of effective Hamiltonian implemented in MD algorithm. We have shown that there is one particular toroidic mode whose dynamical characteristics significantly differ from those of the dielectric modes, despite their interconnection reflected through Eq. 4.3. This toroidic mode softens via a square-root law when the temperature approaches T_t – implying that the toroidal moment is the right order parameter to characterize the formation of electric vortices.

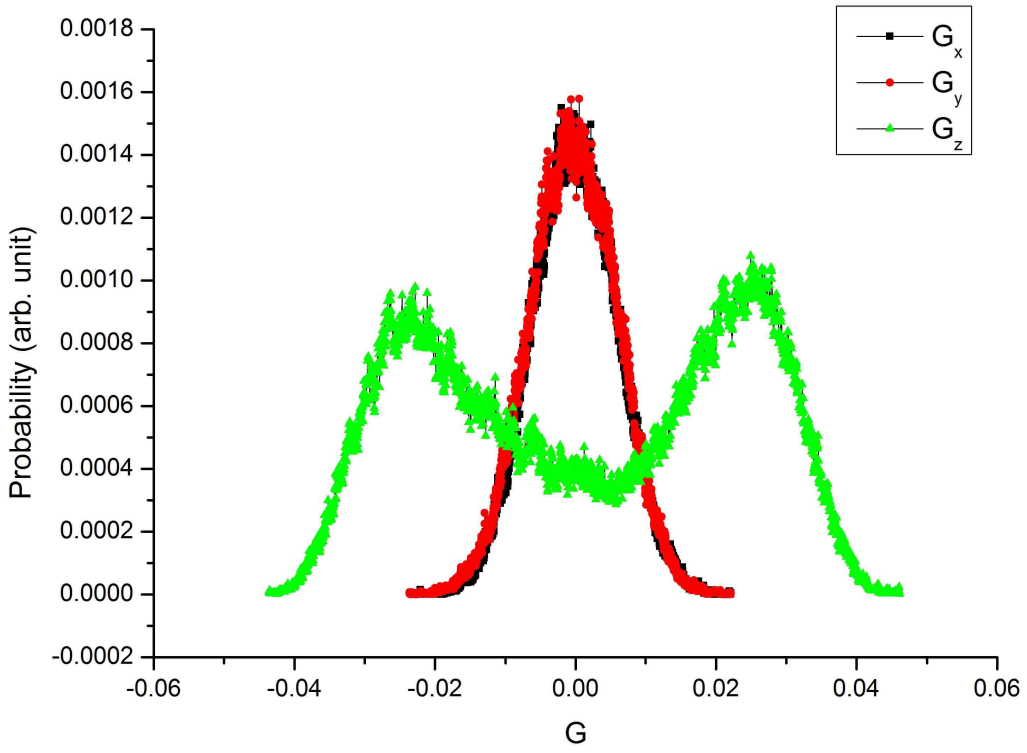

(a)

Figure 4.6: The probability distribution of the three components of the toroidal moment at 325K.

Our work further demonstrates that the dynamics of this toroidic mode originates from the fluctuation of the collectively-organized azimuthal component of electric dipoles. Finally, let us suggest some possibilities to capture the predicted toroidic modes in experiments. Raman and infrared spectroscopies are likely relevant tools to observe the toroidic modes in electrotoroidic systems, based on the fact that magnons have been seen in Raman spectra of multiferroics [95]. Application of a curled external electric field in measurement may also lead to a confirmation of our predictions [9].

Chapter 5

A universal law governing coupled magnetic orders in ABO_3 perovskites

Background

As seen in previous chapters, perovskites form an important class of materials that display not only a rich ensemble of structural phase transitions related to electric dipole moments, but also magnetism, multiferroicity, charge and orbital orderings and superconductivity, which are of great interest for technological applications and for fundamental reasons [96, 97, 98, 99, 100, 101, 102]. In particular, multiferroics have attracted a huge attention in the past decade and still are, because of the existence of magnetic order parameter in addition to an electrical polarization. This extra degree of freedom can lead to many interesting magnetic configurations due to its interaction with other structural degrees of freedom. As a result, many structural phases in various magnetic and multiferroic perovskites display a complex spin arrangement that involves not only one but also different coexisting magnetic order parameters. Well-known examples of such coexistence are the $R3c$ or Cc state of $BiFeO_3$ (BFO) bulks and thin films that exhibit a spin-canted magnetic structure – which generates a weak ferromagnetic (FM) moment (also known as a F-type magnetic ordering) superimposed on a predominant G-type antiferromagnetic (AFM) vector [103, 104, 105, 106, 107]. This corresponds to a combination of two coupled magnetic order parameters. Other examples are the three coupled magnetic orders (to be chosen among the F-, G-, C- and A- types) abundantly found in the $Pnma$ phase of any magnetic or multiferroic perovskite (e.g., orthoferrites) [108, 109, 110, 111, 112]. Understanding such coexistence of coupled magnetic orders is of fundamental but also technological importance, since it can dramatically affect magnetic properties and even leads to the occurrence of the so-much-desired magneto-electric effects. Then many important questions arise: What

are the microscopic origins of these coupled magnetic orders? Can coupled magnetic orders occur in any crystallographic phase? Can one optimize the magnitude of the magnetization in a system that is predominantly antiferromagnetic through the coupling between different magnetic order parameters? Is it possible to have more complex combination than those presently reported, such as those possessing four different magnetic order parameters, in a given crystallographic phase in a perovskite? If it is true, what will be the combination and what are the resulting directions of the different vectors representing the different magnetic order parameters in such combination?

Method

To answer these problems above, group theory seems to be an option, which has been developed in Refs. [111, 113, 114, 115]. Group theory is able to give all the compatible combinations of multiple magnetic orders and the directions along which the corresponding magnetic vectors lie for a given structure. But, it cannot provide any information about the relative magnitudes of coupled magnetic orders or their connections to other structural degrees of freedom. Additionally, it is by no means easy to apply group theory to determine which magnetic orders are coupled, and along which directions the FM and/or AFM vectors are oriented, when choosing a *low-symmetry direction* for the primary magnetic order in, e.g., $R3c$, Cc, $Pnma$ or $Pmc2_1$ states. As a result, a more simpler predictive tool is required in which only structural degrees of freedom are explicitly and straightforwardly involved. Considering the coupled magnetic orders in the $R3c$ and Cc states of $BiFeO_3$ [104, 105, 106] and in the $Pnma$ and/or $Pmc2_1$ phases of $YFeO_3$, RMO_3 (where R^{3+} is a rare-earth ion or yttrium and M^{3+}= Fe^{3+} or Cr^{3+}) and $CaMnO_3$ [109, 110, 111, 112], it seems that the oxygen octahedral tilting is one strongly relevant structural degree of freedom. To start with, let us define the octahedral tilting in perovskites, ω_i (also called the "antiferrodistortive" (AFD) quantity) which is is centered at the B-site of the cell i. The direction of this pseudovector is the axis about which the oxygen octahedra tilt and its magnitude is the angle of the rotation [5]. For example, let us choose $\omega_i = 0.1(\mathbf{x} + \mathbf{y} + \mathbf{z})$,when $\mathbf{x}$, $\mathbf{y}$ and $\mathbf{z}$ are the unit vectors along the [100], [010] and [001] pseudo-cubic directions, respectively. Then it corresponds to a rotation of $0.1\sqrt{3}\ rad$ of

the octahedron at cell i about the pseudocubic [111] direction. As introduced in the effective Hamiltonian in Ref. [105], the main energetic term of our interest is

$$\Delta E = K \sum_{i,j} (\omega_{\mathbf{i}} - \omega_{\mathbf{j}}) \cdot (\mathbf{m_i} \times \mathbf{m_j}), \tag{5.1}$$

where $\mathbf{m}_i$ denotes the magnetic dipole centered on the B-atom of i site and the sum over i runs over all the B-atoms of the perovskite structure while the sum over j only runs over the B-atoms that are *first-nearest* neighbors of the B-site i. K is a parameter that characterizes the strength of this energetic interaction and is therefore material-dependent. Note that Eq. (5.1) can be considered as a particular case of the so-called Dzyaloshinksy-Moriya interaction [116, 117] – that is analytically given by $\mathbf{D}' \cdot (\mathbf{m_i} \times \mathbf{m_j})$ – for which the "mysterious" $\mathbf{D}'$ vector is here simply the difference between the AFD pseudo-vectors at sites i and j. It is important to realize that several remarkable works [111, 113, 114, 115] have derived important properties of the $\mathbf{D}'$ vector, but that none of these works have explicitly connected it with the magnitude and direction of oxygen octahedra tilting, as done in Eq. (5.1). Such connection, which is consistent with some symmetry considerations done in these previous works, is the key to the general formula to be indicated below (in Eq. (5.4)). Then what is left is to connect these quantities to the possible magnetic order parameters and AFD quantities. Since these order parameters are associated with a few discrete commensurate k-points of the first Brillouin zone (BZ) of the cubic reference structure introduced in previous chapters, it is a natural choice to rewrite Eq. (5.1) in k space instead of r space, i.e., expressing the local quantities $\omega_{i,j}$ and $\mathbf{m}_{i,j}$ in terms of k-dependent quantities (e.g., $\omega_{\mathbf{k}}$ and $\mathbf{m_k}$).

First, for the AFD motion, there are two types of AFD motion under our consideration, anti-phase and in-phase tiltings, which are common in perovskite structures. The anti-phase tilting is related to the R-point of of the cubic first BZ. If only the anti-phase tilting is present in the system, then ω_i can be written as $(-1)^{n_x(i)+n_y(i)+n_z(i)}\omega_{\mathbf{R}}$, where $\omega_{\mathbf{R}}$ is constant, site-independent vector and n_x(i), n_y(i) and n_z(i) are the integers indexing the center of the cell i (to be more specific, in the ideal perovskite structure and when denoting as a_{lat} the 5-atom cubic lattice constant, this cell i is centered at $a_{lat}(n_x(i)\mathbf{x} + n_y(i)\mathbf{y} + n_z(i)\mathbf{z})$ with respect to a chosen origin). The in-phase tilting is related to the M-point of the cubic first BZ. If only the in-phase tilting is present, then ω_i is simply written as $(-1)^{n_x(i)+n_y(i)}\omega_{\mathbf{M}}$, where $\omega_{\mathbf{M}}$ is another

homogeneous vector. The k vector at R- and M- point are given as $\mathbf{q_R} = \frac{2\pi}{a_{lat}}(\mathbf{x}+\mathbf{y}+\mathbf{z})$ and $\mathbf{q_{M,xy}} = \frac{2\pi}{a_{lat}}(\mathbf{x}+\mathbf{y})$, respectively. In a general case, ω_i is simply decomposed into the sum of the two previous terms, that is:

$$\omega_i = (-1)^{n_x(i)+n_y(i)+n_z(i)}\omega_{\mathbf{R}} + (-1)^{n_x(i)+n_y(i)}\omega_{\mathbf{M}}, \tag{5.2}$$

where both the anti-phase and in-phase tiltings are present. To better understand it, let us choose the particular case for which $\omega_{\mathbf{R}} = 0.01(\mathbf{x}+\mathbf{y})$ and $\omega_{\mathbf{M}} = 0.04\mathbf{z}$. Such example corresponds to a $a^-a^-c^+$ tilting system (using Glazer notations [118]) with the angle of anti-phase tilting (about [110]) being $\sqrt{2}\times 0.01$ radian and the angle of in-phase tilting (about [001]) being 0.04 radian. Note also that structural constraints associated with the rotation of the oxygen octahedra imply that, for any Cartesian component of $\omega_{\mathbf{M}}$ that is nonzero, that component of $\omega_{\mathbf{R}}$ must be zero, and *vice versa* [119].

For magnetic moments, four common magnetic order parameters are considered here. They are F-, G-, C- and A- type. The F-type is characterized by the ferromagnetic vector denoted by $\mathbf{F}$ and associated with the Γ-point in the cubic first BZ; the G-, C- and A- types are shown as the antiferromagnetic vectors denoted as $\mathbf{G}$ (associated with the R-point in the cubic first BZ), $\mathbf{C}$ (associated with the M-point in the cubic first BZ) and $\mathbf{A}$ (associated with the X-point in the cubic first BZ), respectively. The X-point vector is given as $\mathbf{q_{X,z}} = \frac{2\pi}{a_{lat}}\mathbf{z}$. In case of a general magnetic structure, the magnetic dipole moment at site i is numerically decomposed into a sum of all the four type magnetic vectors as

$$\mathbf{m_i} = \mathbf{F} + (-1)^{n_x(i)+n_y(i)+n_z(i)}\mathbf{G} + (-1)^{n_x(i)+n_y(i)}\mathbf{C} + (-1)^{n_z(i)}\mathbf{A}, \tag{5.3}$$

where all the vectors $\mathbf{F}$, $\mathbf{G}$, $\mathbf{C}$ and $\mathbf{A}$ are presumed to be homogeneous. Note that the magnetic moments are located in the B sublattice of the ABO_3 perovskite structure.

Now put Eqs. (5.2) and (5.3) into Eq. (5.1), and sum first over the six first-nearest neighbors of site i and then over all sites i. After some algebraic work, we arrive at

$$\begin{aligned}\Delta E = {} & 24NK\omega_R\cdot(\mathbf{G}\times\mathbf{F}) \;+\; 16NK\omega_M\cdot(\mathbf{C}\times\mathbf{F}) \\ & +16NK\omega_M\cdot(\mathbf{G}\times\mathbf{A}) \;+\; 8NK\omega_R\cdot(\mathbf{C}\times\mathbf{A}),\end{aligned} \tag{5.4}$$

where N is the total number of sites in the system. There are a few things about Eq. (5.4) worth mentioning. First, it is very simple in terms of explicit expressions of oxygen octahedra

tilting and magnetic vectors. Second, it applies to ABO_3 perovskite structures of which the magnetism comes from the B sublattice. For the case that the magnetism comes from both the A and B sublattices (e.g., as in $NdFeO_3$), it should work for the magnetic structures of Fe ions only.

In order to test such simple yet powerful equation, the comparison of its predictions is given and discussed not only with existing data in the literature, but also with the results of first-principles calculations [120]. In these calculations, a given material (namely, BFO bulk) is chosen and considered in different crystallographic phases. Spin-orbit and non-collinear magnetism are included in these calculations (we numerically found that omitting them will not lead to any coupled magnetism, as consistent with Refs. [104, 105, 112]). Technically, we use the Local Spin Density Approximation and a Hubbard U parameter [29] equal to 3.8 eV for Fe ions, as in Refs. [105, 6, 121]. The 5-atom cubic lattice constant, a_{lat}, is chosen to be 3.85 Å. In each of these calculations, only one magnetic order among the four discussed above is initially chosen with a selected direction of its corresponding order parameter vector. However, while the ions and lattice vectors are kept frozen, the system is then allowed to relax its magnetic structure, and can thus adopt secondary magnetic orders in order to minimize its total energy (the initially chosen magnetic order is referred to as the primary magnetic order, while the other magnetic vectors are termed as secondary). This work has been originally reported in Ref. [122].

Paraelectric cases

In this section, we perform first-principles calculations in the paraelectric phases on various magnetic structures, which are indicated in Tables 5.1 and 5.2 and are now discussed and compared to the predictions of Eq. (5.4).

Anti-phase tiltings within a 10-atom unit cell: to start, we consider the cases for which only anti-phase tilting of the oxygen octahedron exists. A 10-atom unit cell is chosen with the following lattice vectors: $\mathbf{a}_1 = a_{lat}(\mathbf{y}+\mathbf{z})$, $\mathbf{a}_2 = a_{lat}(\mathbf{x}+\mathbf{z})$ and $\mathbf{a}_3 = a_{lat}(\mathbf{x}+\mathbf{y})$. This unit cell is compatible only with the coexistence/existence of a ferromagnetism or a G-type antiferromag-

netism, which reduces Eq. (5.4) to its first term, $24NK\omega_R \cdot (\mathbf{G} \times \mathbf{F})$ ($= 24NK(\omega_R \times \mathbf{G}) \cdot \mathbf{F} = 24NK(\mathbf{F} \times \omega_R) \cdot \mathbf{G}$). The minimization of this energetic term implies that an initially pure G-type AFM structure will have its spins canted via the creation of a magnetization that is parallel or antiparallel to $\omega_R \times \mathbf{G}$ because of the existence of anti-phase tilting. As shown in cases 1-4 of Table 5.1, the predominant G-type AFM vectors are chosen along various directions. For all of the four cases, the first-principles calculations agree with the prediction from the aforementioned energetic term. In case 1, due to the vanishing of the cross product of ω_R and $\mathbf{G}$, the resultant magnetization is zero. In cases 2-4, the calculated magnetization vectors $\mathbf{F}$ lie exactly perpendicular to the predominant $\mathbf{G}$ vectors as from the minimization of Eq. (5.4). On the other hand, in case 5, the predominant magnetic vector is chosen to be the magnetization vector along the x-direction. Then the $\mathbf{G}$ vector is found to lie along the minus y-direction as predicted from Eq. (5.4). Therefore, predictions from Eq. (5.1) indeed hold when performing first-principles calculations, *independently of the chosen direction of the G-type AFM vector and independently of the arrangement of anti-phase oxygen octahedra tilting (and therefore independently of the corresponding crystallographic phase)!* As a matter of fact, it is valid for a $a^0a^0c^-$ tilting configuration (see cases 1-4, that corresponds to a $I4/mcm$ space group) but also for a $a^-a^-a^-$ arrangement (see cases 6-8, for which the space group is $R\bar{3}c$). In particular, (i) no weak magnetization exists when $\mathbf{G}$ lies along $\omega_{\mathbf{R}}$ – as evidenced by cases 1 and 6 of Table 5.1; (ii) the *magnitude* of the magnetization, for a given anti-phase tilting angle, should be the largest when $\omega_{\mathbf{R}}$ and $\mathbf{G}$ are *perpendicular* to each other – which is indeed verified in Table 5.1 (see cases 2 and 3 for $a^0a^0c^-$, and case 8 for $a^-a^-a^-$). Moreover, starting from a free-energy expansion for which the energetic terms involving the magnetization are simply a term proportional to F^2 and the presently proposed $24NK\omega_R \cdot (\mathbf{G} \times \mathbf{F})$ term, one can prove that, for a given $\mathbf{G}$ vector, the magnitude of the magnetization should be directly proportional to the magnitude of $\omega_{\mathbf{R}}$ – that is to the anti-phase tilting angle. Fig. 5.1 indeed confirms the linear relationship between the magnitude of the magnetization and tilting angle, up to quite large magnitude of $\omega_{\mathbf{R}}$.

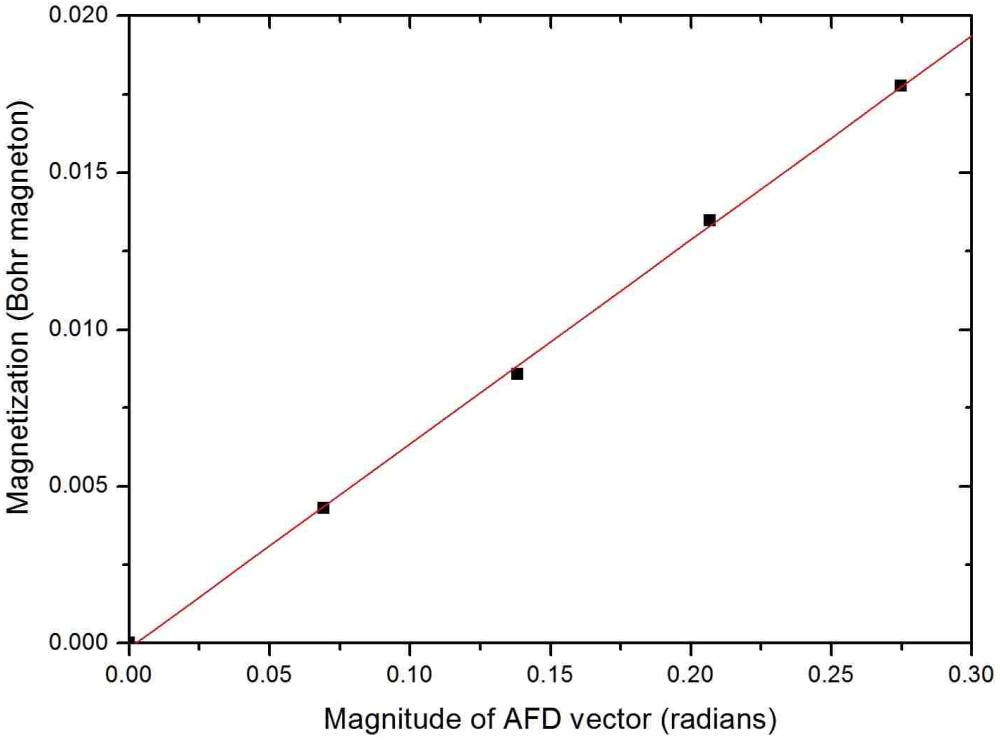

Figure 5.1: This figure shows the magnitude of the magnetization as a function of the angle of tilting of the oxygen octahedra in the $R\bar{3}c$ phase of $BiFeO_3$ bulk, as predicted by first principles. The primary G-type AFM vector is aligned along [101], while ω_R is chosen to be along the $[\bar{1}\bar{1}1]$ pseudo-cubic direction.

The first term of Eq. (5.4) can therefore be practically used to design materials in which a large G-type AFM vector will coexist with a significant magnetization, by searching for a structure in which the G-type AFM vector is perpendicular to a large ω_R. Note also that, if we assume that the magnetic anisotropy only arises from the first term of Eq. (5.4) in a primarily G-type structure, then the minimization of the total magnetic energy should result in a **G** vector and a magnetization that should not only be perpendicular to each other but also should be both perpendicular to $\omega_{\mathbf{R}}$. This is indeed the case in $BiFeO_3$ films [104, 105]. The first term of Eq. (5.4) further implies that a material being primarily ferromagnetic and possessing anti-phase oxygen octahedra tilting will also exhibit a secondary G-type AFM order for which the AFM vector will be parallel or antiparallel to $\mathbf{F} \times \omega_R$. Case 5 in Table 5.1 confirms such prediction.

Table 5.1: Ferromagnetic, **F**, and antiferromagnetic (**G**, **C** and **A**) vectors for different oxygen octahedra tilting arrangements and different resulting *paraelectric* phases in $BiFeO_3$ bulks, as predicted by first principles. The chosen ω_R and ω_M AFD vectors are provided in the first two columns. The asterix symbol indicates the primary magnetic vector. Each different case is referred to by an integer that is indicated at the beginning of each row. The magnetic vectors are expressed in unit of Bohr magneton per Fe ion. The AFD vectors are indicated in radians. The integers in parenthesis indicate the energetic term (first, second, third or fourth) of Eq. (5.4) that are consistent with the direction of the magnetic vectors found by first principles. Glazer notations [118] are used for describing the oxygen octahedra tilting arrangements.

$a^0a^0c^-$		I4/mcm			
$\omega_\mathbf{R}$	$\omega_\mathbf{M}$	**G**	**F**	**C**	**A**
1: 0.16**z**	**0**	4.04**z***	**0** (1)	N/A	N/A
2: 0.16**z**	**0**	4.04**x***	-0.011**y** (1)	N/A	N/A
3: 0.16**z**	**0**	2.86(**x+y**)*	0.008(**x-y**) (1)	N/A	N/A
4: 0.16**z**	**0**	2.86(**x+z**)*	-0.007 **y** (1)	N/A	N/A
5: 0.16**z**	**0**	-0.024**y** (1)	4.14**x***	N/A	N/A
$a^-a^-a^-$		$R\bar{3}c$			
$\omega_\mathbf{R}$	$\omega_\mathbf{M}$	**G**	**F**	**C**	**A**
6: 0.16(-**x-y+z**)	**0**	2.33(-**x-y+z**)*	**0** (1)	N/A	N/A
7: 0.16(-**x-y+z**)	**0**	2.34(**x+y+z**)*	0.012(**x-y**) (1)	N/A	N/A
8: 0.16(-**x-y+z**)	**0**	2.87(**x+z**)*	0.008(**x**-2**y**-**z**) (1)	N/A	N/A
$a^0a^0c^+$		P4/mbm			
$\omega_\mathbf{R}$	$\omega_\mathbf{M}$	**G**	**F**	**C**	**A**
9: **0**	0.16**z**	N/A	**0** (2)	4.10**z***	N/A
10: **0**	0.16**z**	N/A	-0.007**x** (2)	4.11**y***	N/A
11: **0**	0.16**z**	N/A	4.18**x***	-0.012**y** (2)	N/A
$a^-a^-c^+$		Pnma			
$\omega_\mathbf{R}$	$\omega_\mathbf{M}$	**G**	**F**	**C**	**A**
12: 0.16(**x+y**)	0.16**z**	4.05**z***	0.010(-**x+y**) (1)	-0.040(**x+y**) (2)	**0** (3,4)
13: 0.16(**x+y**)	0.16**z**	2.34(**x+y+z**)*	0.006(-**x+y**) (1)	0.015(-**x-y+2z**) (2,4)	0.001(**x-y**) (3)
14: 0.16(**x+y**)	0.16**z**	2.34(**x-y+z**)*	0.005(-**x+y+2z**) (1)	-0.019(**x+y**) (2)	-0.001(**x+y**) (3)
15: 0.16(**x+y**)	0.16**z**	2.87(**x-y**)*	0.012**z** (1)	**0** (2,4)	-0.002(**x+y**) (3)
16: 0.16(**x+y**)	0.16**z**	2.87(**x+y**)*	**0** (1,2)	0.043**z** (4)	0.002(**x-y**) (3)
17: 0.16(**x+y**)	0.16**z**	2.60(-**x+y**+2/3 **z**)*	0.002(-**x+y**-3 **z**) (1)	-0.008(**x+y**) (2)	0.001(**x+y**) (3)
18: 0.16(**x+y**)	0.16**z**	**0** (1,3)	-0.032(**x+y**) (2)	+0.017(-**x+y**) (4)	4.15**z***
19: 0.16(**x+y**)	0.16**z**	-0.007(**x+y**) (3)	**0** (1,2)	0.030**z** (4)	2.94(**x-y**)*
20: 0.16(**x+y**)	0.16**z**	0.007(**x-y**) (3)	0.022**z** (1)	**0** (2,4)	2.94(**x+y**)*
21: 0.16(**x+y**)	0.16**z**	0.005(**x-y**) (3)	0.012(-**x-y+2z**) (1,2)	0.009(-**x+y**) (4)	2.40(**x+y+z**)*
22: 0.16(**x+y**)	0.16**z**	0.015(-**x+y**) (1)	4.23**z***	**0** (2,4)	-0.014(**x+y**) (3)

In-phase tiltings within a 10-atom unit cell: now we consider the cases for which only in-phase oxygen octahedra tiltings exist. For this, another unit cell is chosen that is spanned by the following lattice vectors: $\mathbf{a'}_1 = a_{lat}(\mathbf{x} - \mathbf{y})$, $\mathbf{a'}_2 = a_{lat}(\mathbf{x} + \mathbf{y})$ and $\mathbf{a'}_3 = a_{lat}\mathbf{z}$. This unit cell is compatible with the existence of ferromagnetization and/or C-type AFM. As a result, Eq. (5.4) reduces to the second term alone, that is $\Delta E = 16NK\omega_M \cdot (\mathbf{C} \times \mathbf{F})$ $(= 16NK(\omega_M \times \mathbf{C}) \cdot \mathbf{F} = 16NK(\mathbf{F} \times \omega_M) \cdot \mathbf{C})$. This simple term predicts that (i) with a primarily C-type AFM structure, *in-phase* tiltings will create a magnetization aligned along $\omega_M \times \mathbf{C}$; (ii) with a primarily ferromagnetic structure, *in-phase* tiltings will create a C-type AFM vector aligned along $\mathbf{F} \times \omega_M$. Cases 9-11 in Table 5.1 also confirm these predictions. For instance, in case 10, the primary magnetic vector **C** is chosen to lie along the y-direction. With the in-phase tilting around the z-direction, the magnetic dipoles cant to give a magnetization along the minus x-direction, which is the direction of the cross product of $(\omega_M \times \mathbf{C})$. One can easily verify case 11 when the primary magnetic vector is chosen to be ferromagnetic.

Complex oxygen octahedra tiltings: let us now investigate more complex cases for which *both* in-phase and anti-phase oxygen octahedra tiltings exist. An example of such arrangement is the $a^-a^-c^+$ configuration, that can be tackled by first principles by choosing a 20-atom supercell that is generated by the following lattice vectors: $\mathbf{a'_1} = a_{lat}(\mathbf{x} - \mathbf{y})$, $\mathbf{a'_2} = a_{lat}(\mathbf{x} + \mathbf{y})$ and $\mathbf{a''_3} = 2a_{lat}\mathbf{z}$. Such supercell is compatible with the existence and coexistence of a magnetization, as well as G-, C- and A-types of antiferromagnetism [112]. Consequently, all the four terms of Eq. (5.4) can be activated and play a role in the creation of coupled magnetic orders. Cases 12-22 of Table 5.1 display first-principles results for the $Pnma$ phase of BFO, when initially choosing different primary magnetic orders and different directions of the corresponding FM/AFM vectors. Once again, *all* these results are in-line with Eq. (5.4). Let us provide details on a couple of them to fully exhibit its predictive power.

For instance, in case 15, with both anti-phase and in-phase octahedra tiltings, an initial **G** primary magnetic vector along $[1\bar{1}0]$ leads to the creation of (i) a magnetization along the z-axis as a result of the first term of Eq. (5.4), since the corresponding $\omega_{\mathbf{R}}$ is along [110]; and (ii) a **A** vector that is aligned along $[\bar{1}\bar{1}0]$ because of the third term of Eq. (5.4) in which $\omega_{\mathbf{M}}$ is parallel to [001]. In such case, there is no **C**-type AFM ordering because the second and fourth

terms of Eq. (5.4) vanish (since $\mathbf{F}$ is parallel to $\omega_{\mathbf{M}}$ and $\mathbf{A}$ is parallel to $\omega_{\mathbf{R}}$, respectively). More importantly, cases 12, 15 and 16 in Table 5.1 are fully consistent with the experimental results for the $Pnma$ phase of $YFeO_3$ [109, 110]. Similarly, the measurements for $LaMnO_3$ [108] are consistent with our Case 20, and those for $LuCrO_3$ [123] and $LuFeO_3$ [124] fully match the predictions expressed in Cases 12 and 15, respectively. The observed temperature-induced reorientation of the primary and secondary coupled magnetic orders in the Fe sublattice of $NdFeO_3$ [125] is also covered by Eq. 5.4: it corresponds to Cases 15, 14 and 12 as the temperature is reduced. Moreover, Cases 12, 15, 16, 18, 19, 20 and 22 fully agree with the analysis based on group theory [112] for the $Pnma$ structure (actually for *any* perovskite, including $CaMnO_3$. Note that the x-, y- and z-axes in Refs. [109, 110, 111] are chosen along the $[1\bar{1}0]$, [110] and [001] pseudo-cubic directions, respectively, while they are along the [110], [001] and $[1\bar{1}0]$ directions, respectively, in Ref. [112]. Such choices contrast with ours, for which the x-, y- and z-axes are along the [100], [010] and [001] pseudo-cubic directions). It is thus interesting to realize that our predictions are consistent with pure symmetry analysis associated with the B sites of the ABO_3 perovskite structure while no symmetry argument was used to derive Eq. (5.4)!

It is also important to point out that Eq. (5.4) is more informative than group theory by indicating the microscopic reasons responsible for the coupled magnetic orders and the corresponding directions of their FM/AFM vectors. Another interesting issue that was not addressed in Refs. [109, 110, 112] is the possibility that *all* the four aforementioned magnetic orderings simultaneously exist within a structure. Table 5.1 reveals that this indeed can occur, see cases 13, 14, 17 and 21. Let us try to take advantage of Eq. (5.4) to understand why it happens for the sole Case 21, in which the primary AFM vector is of A-type and is aligned along [111]. This specific $\mathbf{A}$ vector generates (i) a $\mathbf{G}$ vector aligned along $[1\bar{1}0]$ because of the third term of Eq. (5.4), and (ii) a $\mathbf{C}$ vector aligned along $[1\bar{1}0]$ because of the fourth term of Eq. (5.4). The first and second terms of Eq. (5.4) then imply that a $\mathbf{F}$ vector should be created with the preferred energetic choice of having a component along $\omega_{\mathbf{R}} \times \mathbf{G}$ (that is, along [001]) and also having a component along $\omega_{\mathbf{M}} \times \mathbf{C}$ (that is along $[\bar{1}\bar{1}0]$). The system does follow such energetic requirements by choosing a FM vector that is along $[\bar{1}\bar{1}2]$, which also allows it to be

perpendicular to the primary **A** vector. Moreover, Eq. (5.4) is general in the sense that it is also valid for low-symmetry directions. For instance, in a $a^-a^-c^+$ tilting system, choosing **G** along the $[\bar{3}32]$ direction should lead to a magnetization along $[\bar{1}1\bar{3}]$ via the first term of Eq. (5.4), and to the formation of **C** and **A** vectors along [110] via the second and third terms of Eq. (5.4) (the fourth term of Eq. (5.4) vanishes because **C** and **A** are along the same direction). Case 17 in Table 5.1 confirms the predictive power of Eq. (5.4) even for these low-symmetry directions of **G** and **F**. In this case, the predominate magnetic vector is chosen to lie along $[\bar{3}32]$. With the anti-phase tilting around [110] and in-phase tilting around [001], it displays a magnetization along $[\bar{1}1\bar{3}]$ (as permitted by the first term of Eq. (5.4), i.e., $(\omega_R \times \mathbf{G}) \cdot \mathbf{F}$), a A-type AFM along [110] (as permitted by the third term of Eq. (5.4), i.e., $(\omega_M \times \mathbf{G}) \cdot \mathbf{A}$) and a C-type AFM along [110] (as permitted by the second term of Eq. (5.4), i.e., $(\mathbf{F} \times \omega_M) \cdot \mathbf{C}$).

Ferroelectric cases

Interestingly, none of the terms of Eq. (5.4) explicitly involves electric dipoles, which implies that the direction of the resulting coupled magnetic orders should *not* depend on the electric polarization. In other words, what matter are "only" the primary magnetic vector and the oxygen octahedra tilting arrangement. As detailed in Table 5.2, *ab-initio* calculations on phases possessing a polarization (in addition to oxygen octahedra tilting) indeed confirm such surprising prediction. For instance, the secondary FM vector is still along the y-axis when the primary **G** vector lies along [100] for a $a^0a^0c^-$ tilting configuration, independently of the fact that the polarization is along the z-axis (case 2 of Table 5.2, with a $I4cm$ polar space group) or along the x-axis (case 5 of Table 5.2, with a $Fmm2$ polar space group) – exactly as in case 2 of the Table 5.1 (for which the space group is non-polar $I4/mcm$). As demonstrated by the comparison of these two Tables, the insensitivity of the direction of the coupled magnetic orders on the existence and direction of the polarization even holds for complex cases, such as those involving $a^-a^-c^+$ tilting configuration and a primary **A** vector aligned along the [111] direction (see case 21 of Table 5.1 and case 19 of Table 5.2). This insensitivity is a general feature of magnetic perovskites, as demonstrated by the fact that it also explains an interesting result of Ref. [112], namely why the directions of the **G**, **F**, **C** and **A** vectors do not vary (for

Table 5.2: Same as Table 5.1 but for different *ferroelectric* phases. The polarization is expressed in C/m^2.

$a^0a^0c^-$		**P**=0.38**z**		I4cm	
$\omega_{\mathbf{R}}$	$\omega_{\mathbf{M}}$	**G**	**F**	**C**	**A**
1: 0.16**z**	**0**	4.04**z***	**0**	N/A	N/A
2: 0.16**z**	**0**	4.04**x***	-0.007**y**	N/A	N/A
3: 0.16**z**	**0**	2.86(**x+z**)*	-0.005**y**	N/A	N/A
$a^0a^0c^-$		**P**=0.38**x**		Fmm2	
$\omega_{\mathbf{R}}$	$\omega_{\mathbf{M}}$	**G**	**F**	**C**	**A**
4: 0.16**z**	**0**	4.04**z***	**0**	N/A	N/A
5: 0.16**z**	**0**	4.04**x***	-0.012**y**	N/A	N/A
6: 0.16**z**	**0**	2.86(**x+z**)*	-0.009**y**	N/A	N/A
$a^-a^-a^-$		**P**=0.38(-**x**-**y**+**z**)		R3c	
$\omega_{\mathbf{R}}$	$\omega_{\mathbf{M}}$	**G**	**F**	**C**	**A**
7: 0.16(-**x**-**y**+**z**)	**0**	2.33(-**x**-**y**+**z**)*	**0**	N/A	N/A
8: 0.16(-**x**-**y**+**z**)	**0**	2.33(**x+y+z**)*	0.012(**x**-**y**)	N/A	N/A
9: 0.16(-**x**-**y**+**z**)	**0**	2.85(**x+z**)*	0.008(**x**-2**y**-**z**)	N/A	N/A
$a^-a^-c^+$		**P**=0.38**z**		$Pna2_1$	
$\omega_{\mathbf{R}}$	$\omega_{\mathbf{M}}$	**G**	**F**	**C**	**A**
10: 0.16(**x+y**)	0.16**z**	4.05**z***	0.009 (-**x+y**)	-0.034(**x+y**)	**0**
11: 0.16(**x+y**)	0.16**z**	2.34(**x+y+z**)*	0.005 (-**x+y**)	-0.009(-**x**-**y**+2**z**)	0.001(-**x+y**)
12: 0.16(**x+y**)	0.16**z**	2.34(**x**-**y+z**)*	0.005 (-**x+y**+2**z**)	-0.016(**x+y**)	-0.001(**x+y**)
13: 0.16(**x+y**)	0.16**z**	2.86(**x**-**y**)*	0.011**z**	**0**	-0.001(**x+y**)
14: 0.16(**x+y**)	0.16**z**	2.86(**x+y**)*	**0**	0.03 **z**	**0**
15: 0.16(**x+y**)	0.16**z**	2.59(-**x+y**+2/3 **z**)*	0.003(-**x+y**-3 **z**) (1)	-0.009(**x+y**) (2)	0.001(**x+y**)
16: 0.16(**x+y**)	0.16**z**	**0**	-0.019(**x+y**)	+0.031(-**x+y**)	4.15**z***
17: 0.16(**x+y**)	0.16**z**	-0.006(**x+y**)	**0**	0.015**z** (4)	2.94(**x**-**y**)*
18: 0.16(**x+y**)	0.16**z**	0.011(-**x+y**)	0.003 **z**	**0**	2.94(**x+y**)*
19: 0.16(**x+y**)	0.16**z**	0.004(**x**-**y**)	0.009(-**x**-**y**+2**z**)	0.008(-**x+y**)	2.40(**x+y+z**)*
20: 0.16(**x+y**)	0.16**z**	0.012(-**x+y**)	4.22**z***	**0**	-0.011(**x+y**)

a given primary vector aligned a specific direction) when going from a non-polar $Pnma$ phase to a polar $Pmc2_1$ phase. As also nicely emphasized in Ref. [112], knowing such insensitivity

is of large importance to design materials with non-zero linear magneto-electric coefficients. Note, however, that the polarization does have a small effect on coupled magnetic orders: it can slightly modify the magnitude of the secondary magnetic orders, see, e.g., the magnetization in case 4 of Table 5.1 *versus* cases 3 and 6 of Table 5.2. In other words, one can think of the effect of polarization on Eq. (5.4) as to weakly renormalize the strength of the K parameter.

In summary, this work reveals the existence (and its oxygen octahedra tiltings origins) of a "universal" law (i.e., Eq. (5.4)) that governs coupled magnetic orders in perovskites. This "universal" law adopts a shockingly simple analytic form. First-principles calculations confirm its validity for any tested structural paraelectric and even ferroelectric phase, and for any chosen direction of any selected predominant magnetic vector. Examples of many important findings resulting from this proposed law are: (i) the coupled magnetic orders microscopically originate from anti-phase and/or in-phase oxygen ocathedra tiltings; (ii) when anti-phase oxygen octahedral tiltings only exist, a magnetization can be generated through spin canting of a predominant G-type AFM structure and is maximized in magnitude if the predominant G-type AFM vector is perpendicular to the axis about which the oxygen octahedra tilt and vice versa; and for a given G vector, the magnitude of the magnetization is directly proportional to the magnitude of the anti-phase tilting angle; (iii) when there is only in-phase oxygen octahedral tiltings, a magnetization can be also created by a predominant C-type AFM structure and can be maximized if the predominant C-type AFM vector is perpendicular to the axis about which the oxygen octahedral tilt and vice versa; (iv) when both anti-phase and in-phase oxygen octahedral tiltings exist in a given paraelectric phase, there is a possibility that A-type, C-type, F-type and G-type magnetic orders can ALL coexist in a structure and their corresponding vectors lie along restrained directions that are all given by the proposed "universal" law; (v) for polar phase, the existence of the polarization has no effect on the direction of the coupled magnetic orders, but do weakly alter the strength of the secondary magnetic order parameters. Such insensitivity is of large importance to design materials with non-zero linear magneto-electric coefficients. This "universal" law is straightforward and easy to manipulate to search for novel multiferroics. It can also be easily generalized to derive novel energetic expressions, in case of coupled magnetic orders that are different and even more complicated than F-, G-, A- and C-types. It should

also be noted that the work here does not exclude the possibility that other energetic terms, such as the Dzyaloshinksy-Moriya interaction [116, 117] or spin-current-induction model [126], involving the electrical polarization [127] or other structural degrees of freedom (rather than AFD distortions) can also possibly govern coupled magnetic orders in materials.

Chapter 6

Electronic properties of ferroelectric vortices from large-scale *ab-initio* computations

Background

Topological defects exist in several areas of science, e.g., particle physics and condensed matter physics. Along with their special topologies, topological defects exhibit many unique properties, which renders them of great interest to the scientific community [128]. Such interest includes *electrical* vortices, or related flux-closure configurations, that have been predicted to exist about ten years ago [59] and that have been more recently observed [60, 61, 70, 66, 65, 62, 63, 64, 67, 68, 69]. During the past decade, several works have been aimed at investigating electrical properties of topological defects for possible applications in electronic devices (see, e.g., Refs. [129, 130, 131, 60] and references therein). In particular, Ref. [60] observed that the current–*versus*-voltage (I-V) curve starts to be significant for a voltage of about 1 V in $BiFeO_3$ (BFO) thin films having artificially-created electrical vortices, that is about 2 V *lower* than the corresponding critical voltage in BFO systems having no topological defect. One fundamentally- and technologically-important issue to resolve is the origin of such reduction in critical voltage and resulting significant electrical current measured between 1 and 2V. For instance, is it an intrinsic effect, i.e., is it associated with a remarkable reduction of the electronic band gap, since the I-V curve shown in Ref. [60] resembles that of a p-n junction and the I-V curve in p-n junctions does naturally depend on the electronic band-gap [132]? Or is such origin extrinsic in nature, i.e. is it due, e.g., to the existence of vacancies near the topological defects? Such issue is not easy to address for several reasons. First of all, on an experimental level, it is by no means trivial to separate intrinsic *versus* extrinsic effects on I-V curves in systems possessing topological defects [60]. Secondly, electrical vortices are rather

large in size which makes the calculation of their electronic properties by standard numerical codes rather challenging. For instance, the computational scheme that has been used in Ref. [59] to predict the existence of electrical vortices, that is the effective Hamiltonian technique, can lead to the prediction of the relaxed positions of the thousands of atoms forming an electrical vortex but can not yield its electronic properties because electrons are not included as degrees of freedom in this scheme. Conversely, traditional first-principles codes can mimic well both the atomic and electronic structures of materials, but "only" providing that the system's size is well below the typical size of electrical vortices (otherwise the computations are too memory- and time-intensive and thus become practically unfeasible) [120, 134, 133]. As a result of this conundrum, it is presently unknown if electric topological defect can intrinsically and significantly modify electronic properties.

Moreover, ferroelectric nanocomposites, that are nanostructures made of two different ferroelectric materials, have been recently predicted to possess electrical vortices below a certain critical temperature [85, 135]. It is thus legitimate to also wonder what type of band alignment these systems adopt, i.e. is it type-I for which both the valence band maximum (VBM) and conduction band minimum (CBM) are localized within the same material or type-II for which one band-edge state is localized in one material while the other is localized in the second material forming the nanocomposite? One may even ask if the formation of electrical vortices in these nanocomposites can change the type of the band alignment, which will constitute a novel effect of fundamental and technological interest. This work has been originally reported in Ref. [136].

Method

Motivated to resolve the aforementioned issues, we employ a new *ab-initio* procedure and apply it to a nanocomposite made of $BaTiO_3$ (BTO) nanowires inserted in a matrix formed by $SrTiO_3$ (STO). This procedure consists in combining the effective Hamiltonian technique with the linear-scaling three-dimensional fragment method (LS3DF) that was initially developed in Ref. [137] for semiconductor systems. The first technique allows to obtain the relaxed atomic configuration associated with topological defects in ferroelectrics, that is then used as inputs of

the second tool to predict the corresponding electronic structure.

Here, the investigated system is a stress-free nanocomposite made of a periodic squared array of $BaTiO_3$ (BTO) nanowires embedded in $SrTiO_3$ (STO). This type of nanocomposite is chosen because it has been recently shown to exhibit electrical vortices below a certain critical temperature [85, 135]. The nanowires have a long axis oriented along the pseudo-cubic [001] direction (chosen to be the z-axis) and possess a squared cross-section of 6×6 in lattice constant units (i.e., 2.4×2.4 nm^2 area) in the (x,y) plane, where the x- and y-axes are along the pseudo-cubic [100] and [010] directions, respectively. The whole nanocomposite is mimicked by a $12 \times 12 \times 4$ supercell, that is periodic along the x, y and z axes and that contains a single nanowire. To explore properties of such system, we employ two different numerical methods: (1) the effective Hamiltonian ($H_{\rm eff}$) method developed in Ref. [4] for (Ba,Sr)TiO_3 (BST) compounds, in order to obtain the relaxed atomic configuration at different temperatures; and the (2) linear-scaling three-dimensional fragment method (LS3DF) developed in Ref. [137], in order to compute the electronic structure of such atomic configurations. Regarding $H_{\rm eff}$, its total internal energy consists of two main terms:

$$\begin{aligned} E_{\rm tot} = & E_{\rm ave}\left(\{\mathbf{u}_i\},\{\mathbf{v}_i\},\{\eta_H\}\right) \\ & + E_{\rm loc}\left(\{\mathbf{u_i}\},\{\mathbf{v}_i\},\{\sigma_j\},\{\eta_{\rm loc}\}\right), \end{aligned} \tag{6.1}$$

where $\mathbf{u}_i$ denotes the local soft mode that is centered on the Ti-sites of the 5-atom unit cell *i* ($\mathbf{u}_i$ is directly proportional to the electric dipole moment of that cell, and represents the collective motion of the Ba/Sr, Ti and oxygen atoms inside the cell i [3]); $\{\mathbf{v}_i\}$ are the dimensionless displacement variables defined at the cell corners and are used to calculate inhomogeneous strain tensor components of the cell *i* [3]; $\{\eta_H\}$ is the homogeneous strain tensor, which allows the simulation supercell to vary in size and shape [3]; σ_j characterizes the atomic distribution of of the mixed A-sublattice [13], with σ_j=+1 or -1 corresponding to the presence of a Ba or Sr atom, respectively, at the A-lattice site *j*; and $\{\eta_{\rm loc}\}$ represents the local strain resulting from the difference in ionic size between Ba and Sr atoms, which is relatively large ($\simeq$2%). The first energy term, $E_{\rm ave}$, contains a local mode self-energy, a long-range dipole-dipole inter-

action, a short-range interaction between local soft modes, an elastic energy, and interactions between local modes and strains [3] within the application of the virtual crystal approximation [138, 139] to model $(Ba_{0.5}Sr_{0.5})TiO_3$ solid solutions. On the other hand, $E_{\rm loc}$ can be thought of as a perturbative term due to the fact that BST systems possess real Ba and Sr atoms on the A-sites rather than a virtual, compositional-dependent $\langle A \rangle$ atom. To be specific and as detailed in Ref. [4], energetic terms in $E_{\rm loc}$ model how the presence of real Ba and Sr ions inside the system affects the local soft modes and the inhomogenuous strain tensor, as well as take into account the strain that is induced by the size difference between Ba and Sr ions and its effect on physical properties. The parameters entering the total internal energy of this $H_{\rm eff}$ are derived from first principles. Previous calculations [140, 4, 141, 80, 142] using this $H_{\rm eff}$ for various disordered or ordered BST systems demonstrated its accuracy. Note that the nanocomposite investigated in the present manuscript is stress-free, and, as a result, the matrix, interface and wires adopt different lattice constants – implying that the strain is inhomogeneous, as it should be in most nanostructures. This $H_{\rm eff}$ is employed here within Monte-Carlo simulations to obtain the (temperature-dependent) positions of all the Ba, Sr, Ti and oxygen ions belonging to the supercell used to mimic the studied nanocomposite.

As aforementioned, electronic properties associated with the resulting atomic configurations are then calculated by the LS3DF method. The LS3DF method is a linear scaling method to self-consistently solve problems in the frame of density functional theory (DFT) [15, 16]. It (1) divides the system into overlapping fragments; (2) solves the fragment wave functions, and obtains the fragment charge densities; (3) patches the fragment charge densities together to yield the global charge density of the whole system, which is realized here by using a partition function to obtain only the central part of the fragment charge density; (4) solves the Poisson equation of the whole system based on the global charge density. Note that the LS3DF "only" gets the total charge density, hence the potential of the system, but not the eigenwave functions of the whole system. The eigenwave functions and eigenenergies of the whole system are obtained using the folded spectrum method [143] with the potential provided by the LS3DF calculations. The LS3DF method can solve systems with tens of thousands of atoms, and has been shown to yield results being almost identical to those obtained by the conventional full

system DFT [144]. It has been used to study various type of problems and materials, including: ZnTe:O alloy [145], ZnO nanorod [146], MoS_2/$MoSe_2$ Moirres pattern [147], and organic hybrid perovskite $CH_3NH_3PbI_3$ [144]. Note that $Ba\ 6s$, $Sr\ 5s$, $Ti\ 4s$ and $3d$, and $O\ 2s$ and $2p$ electrons are treated as valence electrons in the present LS3DF calculations.

In order to test the accuracy of the LS3DF method on ferroelectrics, we first decided to choose two supercells having the same size as our investigated nanocomposite (i.e., $12 \times 12 \times 4$) but made either of *pure* BTO or *pure* STO material with all the different atoms being at their ideal cubic positions. The LS3DF method within local density functional approximation (LDA) [17] yields a value of 1.81 eV and 1.98 eV for the band gap of these paraelectric $BaTiO_3$ and $SrTiO_3$ pure materials, respectively. These values are identical or very close to the 1.81 eV and 2.06 eV band gaps of ideal BTO and STO, respectively, obtained from direct DFT calculations using the PEtot code [148]. This comparison therefore demonstrates the capability of the LS3DF method to model the electronic structure of ferroelectric materials in their non-polar phases, especially once realizing that different DFT calculations can provide some range for these band gaps [149].

Electronic properties

Let us now use the numerical procedure described above to investigate electronic properties of our nanocomposite. For that, it is first important to know that the aforementioned effective Hamiltonian predicts that such system exhibits a ferrotoroidic and paraelectric state (to be denoted as FT-PE) for temperatures ranging between $T_C \simeq 105$ K and $T_t \simeq 215$ K. In other words, it possesses an electrical vortex but does not have any net spontaneous electrical polarization,

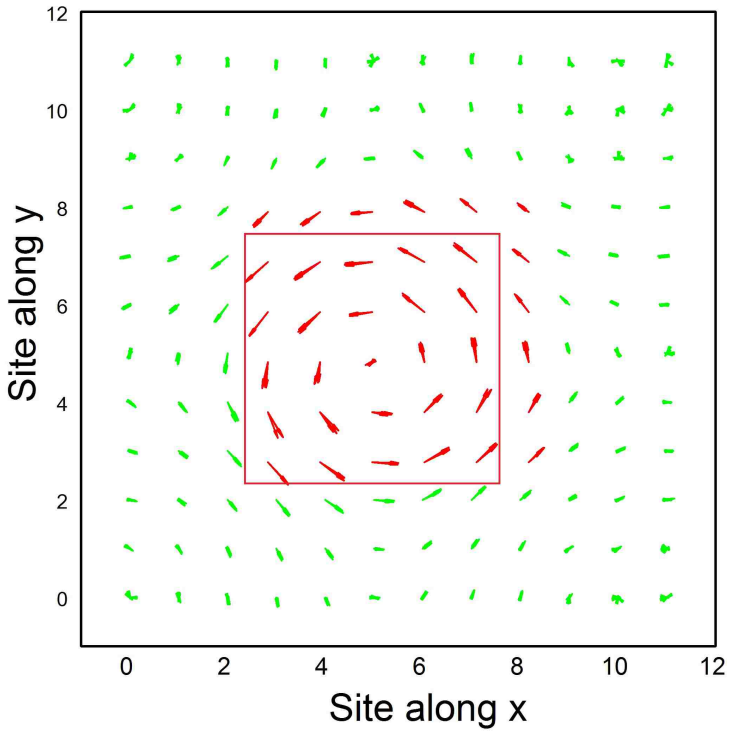

Figure 6.1: Top view (seen from negative z- direction) of the local mode configuration in the FT-PE state of the studied nanocomposite at 165 K, as predicted by the effective Hamiltonian technique. These local modes are centered on Ti ions, and are represented by arrows that have been amplified 20 times for a better view. The light red lines go through the Ba atoms that are located at the interface between the BTO nanowire and the STO matrix.

in this range of temperature. The resulting dipolar configuration is displayed in Fig. 6.1, which reveals that the FT-PE state consists of a *circular* electrical vortex forming in the (x,y) planes inside the $BaTiO_3$ nanowire. The driving force behind the formation of such electrical vortex is the depolarizing field arising from the existence of the $SrTiO_3$ matrix surrounding the nanowire. This vortex is numerically found to disappear for temperatures above T_t, therefore leading to a paratoroidic and paraelectric phase (that will be termed PT-PE). On the other hand, the studied system further acquires a spontaneous polarization along the z-direction, in addition to the vortex structure, when the temperature is below T_C. In the present study, we will focus on two different temperatures: a first temperature $T_{PT-PE} = 425K$, as representative of the PT-PE state; and a second temperature $T_{FT-PE} = 165K$ which lies inside the region of stability of the FT-PE state. For each of these two temperatures, the atomic positions and lattice vectors of

the resulting $12 \times 12 \times 4$ nanocomposite supercell predicted by the H_{eff} technique are fed as inputs to the LS3DF method. Comparing the output electronic properties of these two different supercells will thus reveal the effect of electrical vortex on such properties.

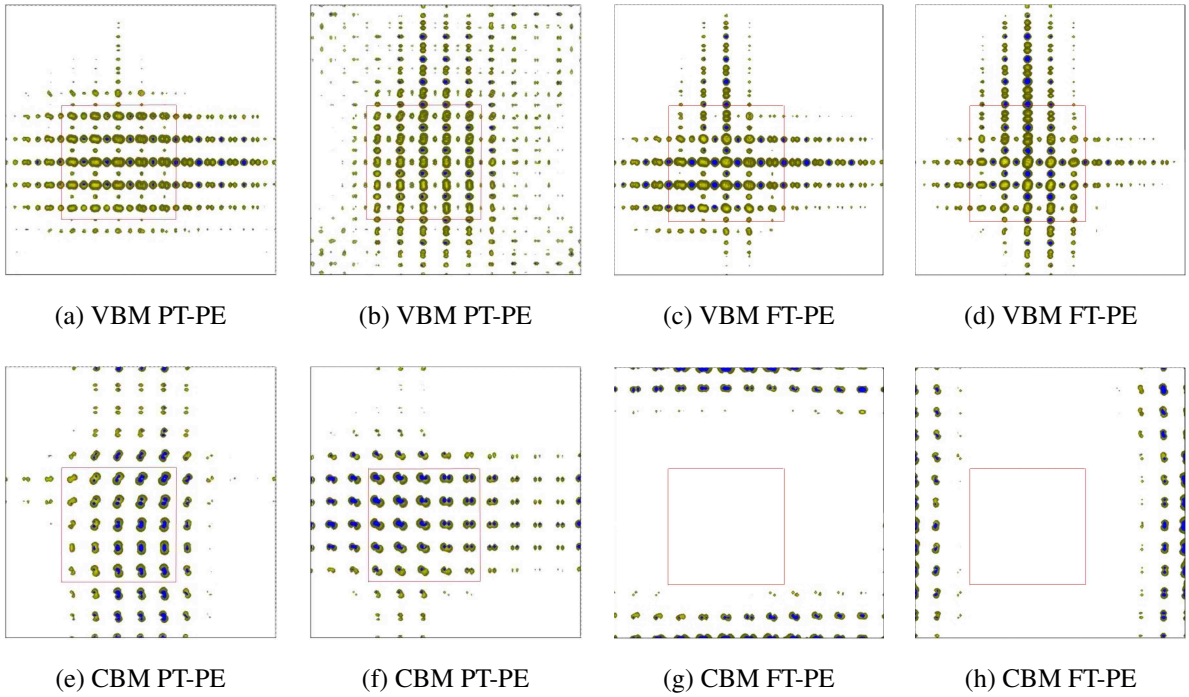

(a) VBM PT-PE (b) VBM PT-PE (c) VBM FT-PE (d) VBM FT-PE

(e) CBM PT-PE (f) CBM PT-PE (g) CBM FT-PE (h) CBM FT-PE

Figure 6.2: Top view (seen from negative z- direction) of the real-space charge density distribution of the band edge states of the investigated system, as predicted by the LS3DF method. Panels (a) and (b) show the VBM states in the PT-PE phase, while Panels (e) and (f) display the CBM states of that PT-PE phase. Panels (c-d) and (g-h) report the same information than Panels (a-b) and (e-f), respectively, but for the FT-PE phase. The light red lines go through the Ba atoms that are located at the interface between the BTO nanowire and the STO matrix.

Figures 6.2a and 6.2b display the top view of the charge densities of the two degenerate valence band maximum states for the PT-PE phase. Figures 6.2e and 6.2f show similar information but for the two degenerate conduction band minimum states of that PT-PE phase, respectively. For the VBM states, the charge density is distributed mainly inside the $BaTiO_3$ nanowire (which is delimited by light red lines there), specifically around oxygen ions. This is consistent with the fact that the valence band of pure $BaTiO_3$ is known to be formed by oxygen $2p$ orbitals [150]. The charge density of the CBM states of the PT-PE phase is also mostly localized inside the $BaTiO_3$ nanowire, however, specifically around titanium ions, which is also in-line with the known fact that the conduction band of pure $BaTiO_3$ is made of Ti d orbitals [150]. As schematized on the left part of Fig. 6.5, the PT-PE phase can thus be considered to

possess a type-I band alignment since both its VBM and CBM are localized in the confined quantum object (i.e., the $BaTiO_3$ nanowire here) [151]. The resulting band gap is numerically found to be 1.87 eV (note that we also performed a similar calculation in this phase but with ions put at their ideal positions and obtained the same band gap value, i.e., 1.87 eV, which thus shows that thermally induced randomly-oriented dipoles have no effect on the band gap). This latter value is *larger* than the aforementioned value of 1.81 eV obtained for pure paraelectric $BaTiO_3$, which is consistent with the fact that the BTO wire is quantum mechanically confined by the STO medium in the (x, y) plane of the nanocomposite [152]. However, the difference between these two band gaps is only of the order of 0.06 eV, implying that the quantitative effects of this quantum confinement is not that large, likely because the band offset between $BaTiO_3$ and $SrTiO_3$ is rather small as indicated by their similar band gaps.

For comparison, Figures (6.2c-6.2d) and (6.2g-6.2h) show the same top view of the charge densities of the two degenerate VBM and CBM states but for the ferrotoroidic and paraelectric (FT-PE) phase, respectively. One can see that the charge density of the VBM states of FT-PE is very similar to that of PT-PE, and is thus also mainly localized on the oxygen atoms belonging to the $BaTiO_3$ nanowire. The main difference between electronic properties of FT-PE and PT-PE, in fact, resides in their CBM: as shown in Figs. 6.2g and 6.2h, the occurrence of the electrical vortex inside the nanowire makes the charge density of the CBM going outside this nanowire towards the matrix.

From the local density of states calculations shown in Fig. 6.3, we numerically found that the lowest-in-energy conduction state localized within the BTO nanowire is $\simeq 0.22\ eV$ higher than the CBM state shown in Figs (6.2g-6.2h), which results in a difference in energy of 2.12 eV between the band edge states localized within the BTO nanowire. The enlargement of this transition by 0.25 eV within the BTO nanowire, as compared to 1.87 eV in the PT-PE phase, can therefore have two different origins: it is either due (i) to the fact that *individual* dipoles are rather significant in the FT-PE phase, or (ii) to the *collective* vortex organization of these dipoles in this phase. We numerically found that scenario (ii) holds, as evidenced by the fact that considering significant but randomly oriented dipoles inside the nanowires did *not* result in such large band lifting of 0.25 eV (note that collective organization of dipoles can indeed

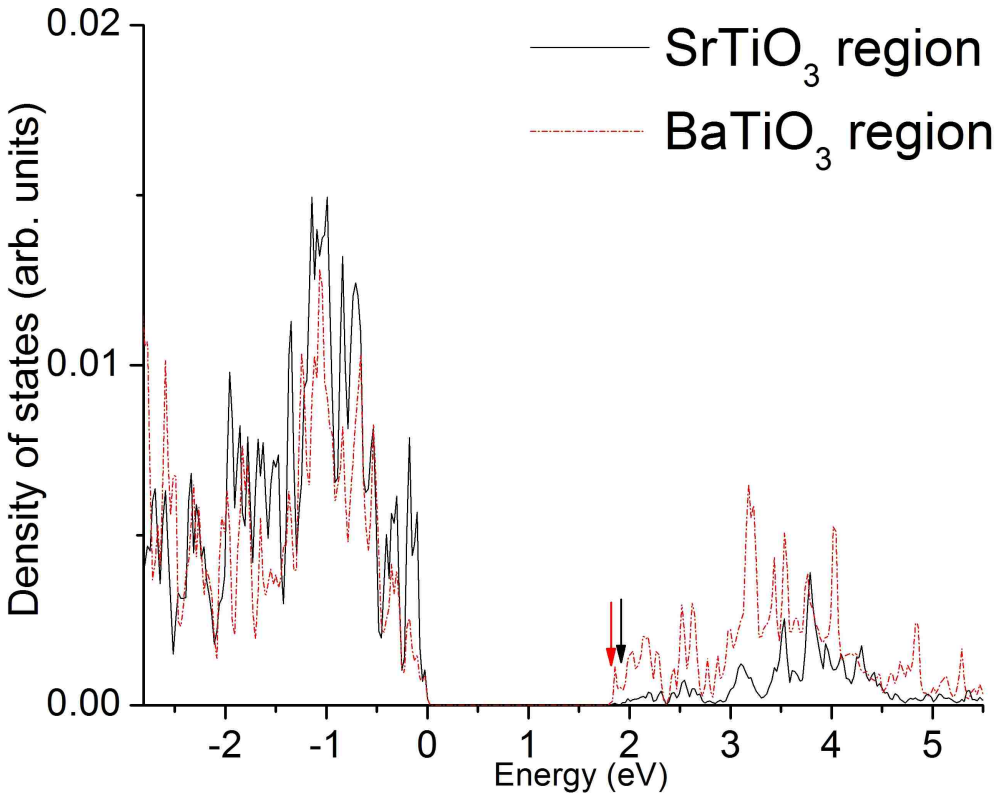

(a) PT-PE

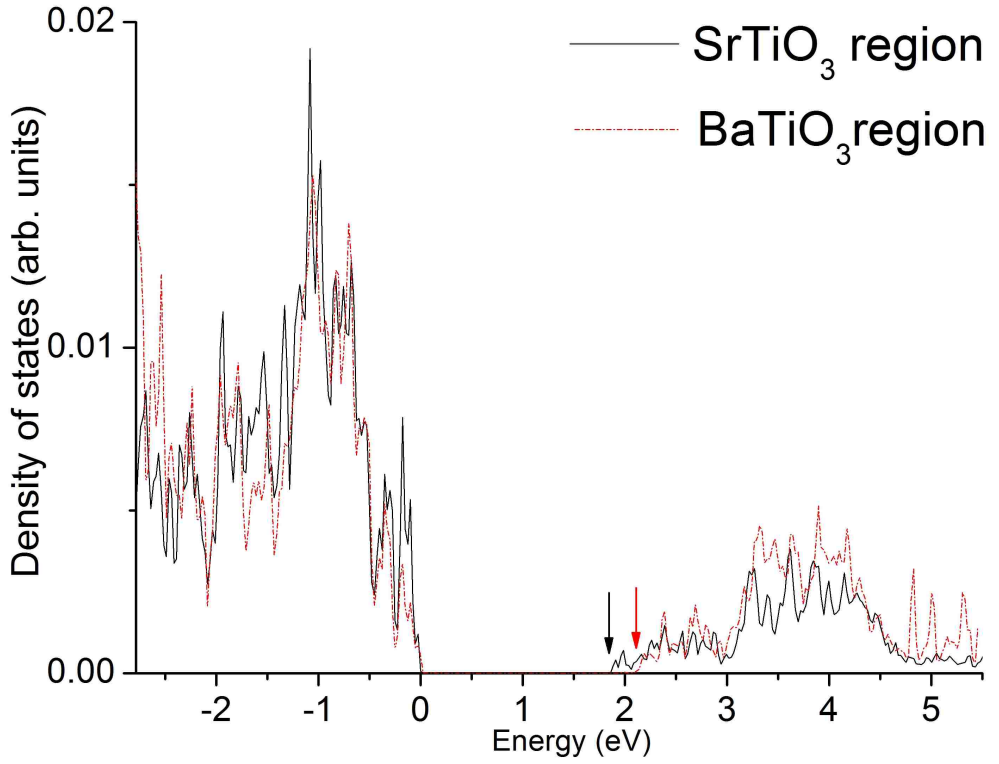

(b) FT-PE

Figure 6.3: The local density of states (LDOS) for (a) the PT-PE phase and (b) the FT-PE phase. The black solid lines denote LDOS within the $SrTiO_3$ region, while the red dash lines show LDOS within the $BaTiO_3$ region. The arrows provide a guide for the eyes regarding the lowest-lying conduction states.

have a large impact on the band gap, as further illustrated by additional calculations we performed for which the dipoles inside the wire are all oriented along the same direction and have the same magnitude, therefore leading to a ferroelectric state: in that case, the band gap was found to increase by 0.40 eV (mainly from the uplifting of the CBM state) with respect to the paraelectric state, as consistent with, e.g., Ref. [153]). Specifically, such enlargement of 0.25 eV is found to be related to the larger electrostatic potential (due to the dipole arrangements) in the FT-PE phase than in the PT-PE phase. We numerically found that scenario (ii) holds, as evidenced by the fact that considering significant but randomly oriented dipoles inside the nanowires did *not* result in such large band lifting of 0.25 eV (note that collective organization of dipoles can indeed have a large impact on the band gap, as further illustrated by additional calculations we performed for which the dipoles inside the wire are all oriented along the same direction and have the same magnitude, therefore leading to a ferroelectric state: in that case, the band gap was found to increase by 0.40 eV (mainly from the uplifting of the CBM state) with respect to the paraelectric state, as consistent with, e.g., Ref. [153]). Specifically, such enlargement of 0.25 eV is found to be related to the larger electrostatic potential (due to the dipole arrangements) in the FT-PE phase than in the PT-PE phase. This larger electrostatic potential "pushes up" the conduction band edge state of the BTO nanowire, as a result of the more organized dipolar (vortex) configuration in the FT-PE phase. As a result of this push, Figures 6.2g and 6.2h show that the charge density of the CBM states of the FT-PE case prefers to localize *inside* $SrTiO_3$, more specifically around Ti atoms belonging to stripes being oriented along the x- or y-axis. In contrast with the PT-PE state and as schematized in Fig. 6.5, the FT-PE state therefore adopts a type-II alignment since the VBM localizes in the confined quantum object while its CBM prefers to lie outside of it [151]. Varying temperature can therefore lead to a control of the band alignment type (i.e., type-I *versus* type-II), since temperature is the thermodynamical parameter driving the transition from the PT-PE to FT-PE state in the presently studied nanocomposite. Interestingly, we are not aware of any previous study reporting the possibility of having both types of band alignment within the *same* system when varying a physical factor. Such possibility may lead to the development of original devices exploiting the advantage of both types of alignments, that are, e.g., light emitting devices for type-I band

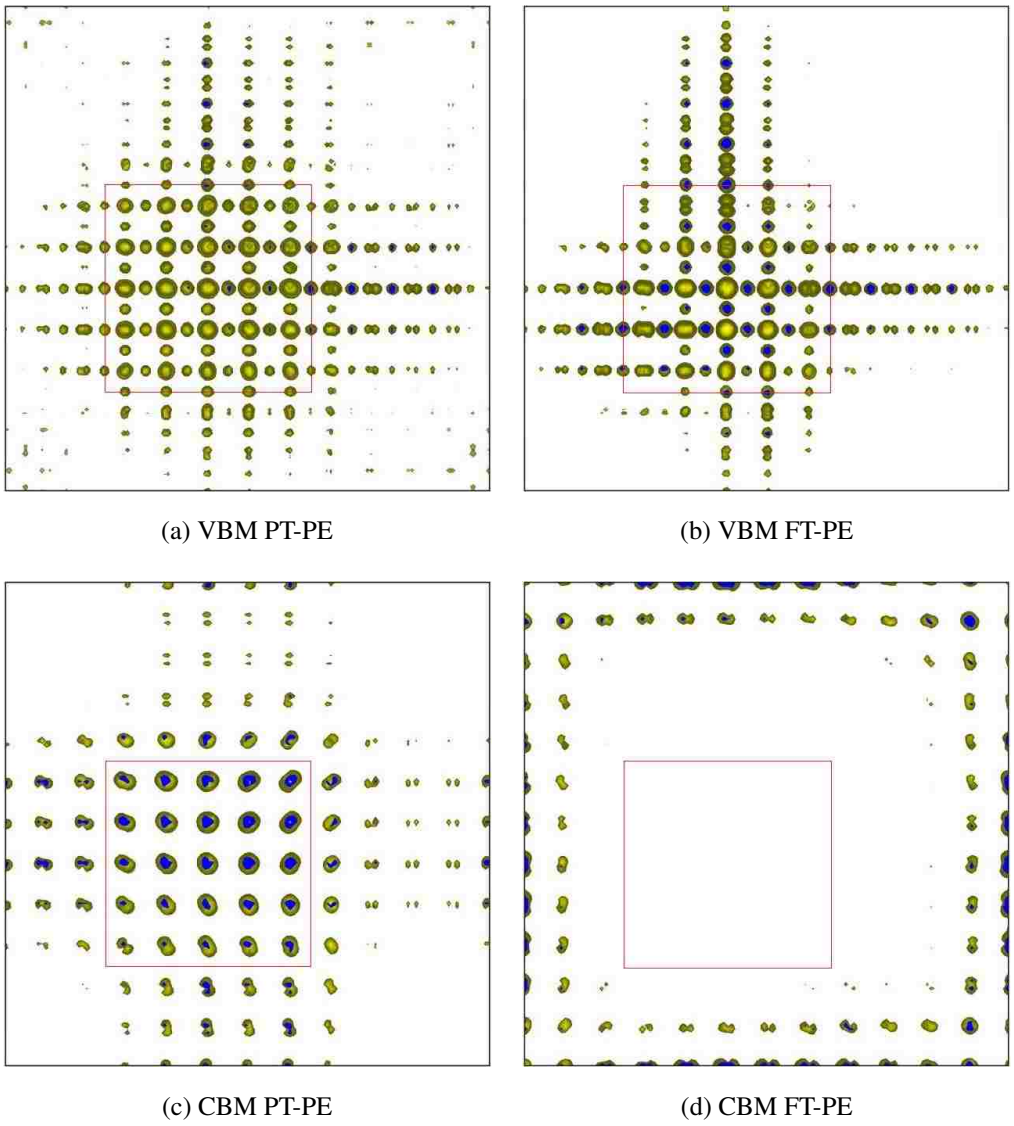

(a) VBM PT-PE (b) VBM FT-PE

(c) CBM PT-PE (d) CBM FT-PE

Figure 6.4: (Color online) Top view (seen from negative z-direction) of the real-space charge density distribution of the band edge states of the investigated system from the linear mixture of degenerate states, as predicted by the LS3DF method. Panels (a) and (c) show the VBM and CBM states in the PT-PE phase, respectively. Panels (b) and (d) display the VBM and CBM states of the FT-PE phase. The light red lines go through the Ba atoms that are located at the interface between the BTO nanowire and the STO matrix.

alignment *versus* photovoltaic devices and detectors for type-II band alignment [154]. These hypothetical original devices may even be functionalized to operate at room temperature by varying the sizes of, and separation between, the BTO wires. This is because playing with these two latter physical parameters can make the T_t critical temperature at which the PT-PE–to–FT-PE occurs being near 300K, as demonstrated in Ref. [85].

It is also worth mentioning the fact that these stripes can be along the x- *and* y-axis, which

is consistent with the symmetry of the studied system. Due to the overall symmetry of the studied nanocomposite system, the x- and y- directions are equivalent. The charge densities of the *two degenerate* valence band minimum state (VBM) and conduction band minimum states (CBM) are shown in Figs. 6.2 for both the PT-FE and FT-PE phases. One can linearly combine the charge densities of these two degenerate states to have a global state that will better display the overall system's symmetry. Such combination is reported in Fig. 6.4 for both the VBM and CBM states, in the PT-PE and FT-PE phases.

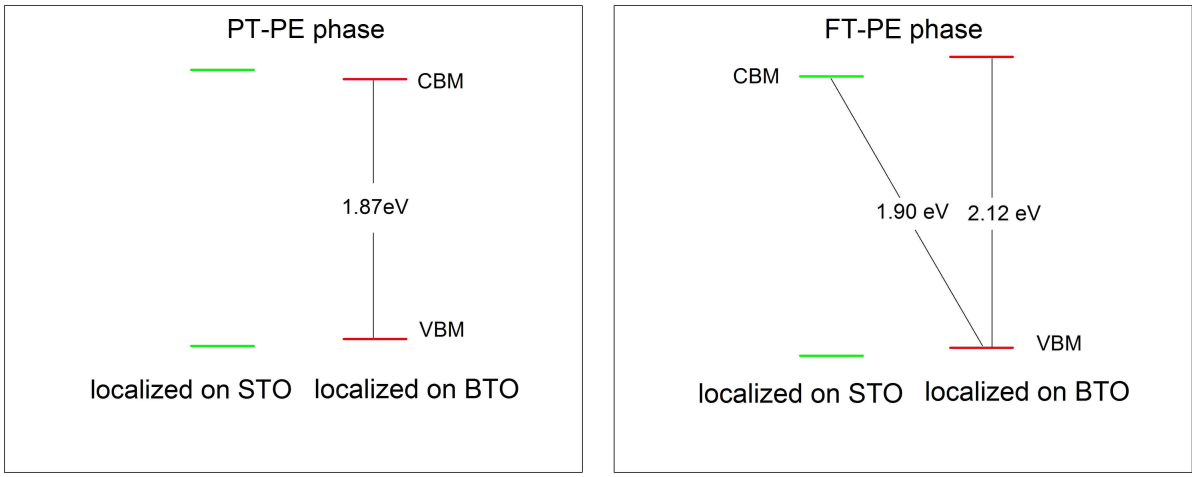

(a) (b)

Figure 6.5: (Color online) Schematization of the band alignment for the PT-PE (Panel a) and FT-PE (Panel b) phases, respectively.

Moreover and as shown on the right part of Fig. 6.5, the band gap of the FT-PE state (that is, the difference in energy between its CBM and VBM states) is about 1.90 eV, that is of the same order than the band gap of 1.87 eV of the PT-PE state. Such numerical finding, altogether with the aforementioned difference in energy of 2.12 eV between the highest occupied and lowest unoccupied states localized within the BTO nanowire, therefore resolve an important current issue: the formation of an electrical topological defect does *not* intrinsically imply a significant decrease of the band gap. In particular, our finding strongly suggests that the remarkable current experimentally found for voltage corresponding to energy being 2 eV below the band gap of $BiFeO_3$ bulk, when electrical vortices form inside $BiFeO_3$ films [60], is an extrinsic rather than intrinsic effect. It is likely caused by the fact that vortices are a natural place for structural

defects (e.g., oxygen vacancies) to form or migrate to. The results also imply that the "true" band gap of both the FT-PE and PT-PE states should be close to 3.2 eV (which is at the border between violet and ultraviolet lights) based on the facts that (1) the *predicted* band gaps of both these states are close to each other and within the 1.87–1.90 eV range; and (2) the LDA method used here was found above to lead to an underestimation of the band gap by nearly 1.3 eV with respect to experiments in pure BTO and STO systems [155, 156, 157].

In summary, we have combined the effective Hamiltonian method with the LS3DF scheme to study electronic properties of structurally-relaxed ferroelectric nanocomposites. This combination reveals that the formation of electrical vortex (i) does *not* intrinsically decrease the magnitude of the band gap (in fact, it rather significantly increases by $\simeq 0.25$ eV the transition between band-edge states localized within the BTO nanowires); and (2) dramatically modifies the type of band alignment. We hope that the present study helps in better understanding the role of topological defects on electronic properties of ferroelectrics, and may be put into some use to design novel devices with original capabilities. We are also confident that the proposed combination of these two different techniques will be taken advantage of, in order to investigate other non-trivial electrical, electronic and optical properties of ferroelectric systems in the future.

Conclusion

In conclusion, we have elaborated several different studies that focus on static, dynamical, magnetic and electronic properties of ferroelectrics and multiferroics.

For (110) BaTiO3 (BTO) films, we discovered (i) the existence of low-symmetry phases (including three monoclinic ones and an unusual triclinic phase), (ii) that, near room temperature, there are a series of novel phase transitions: starting from an aa state (orthorhombic phase) in the far compressive strain region, then passing through an ab state (monoclinic phase) and an abc state (triclinic phase) by second order transitions in the near region of zero strain, and finally turning into a r_c state (which is another different monoclinic phase) by a first order transition, (iii) that the fast strain-induced rotation of the polarization associated with these latter transitions results in huge dielectric and piezoelectric responses, which is very promising to design efficient miniaturized lead-free devices; (iv) that one can easily switch between different polarized states by applying in-plane and out-of-plane electric fields, which is promising for the design of novel memory devices, and (v) that the Curie temperature in the compressive strain region is nearly independent of the epitaxial strain. Items (i)-(v) all differ from features previously seen in (001) BTO films. We also proposed an alternative procedure with respect to the usual way of growing (001) films on top of *various* substrates, i.e., to grow ferroelectric films on a single, amply available and economic substrate (such as $SrTiO_3$), but vary the crystallographic direction (away from the pseudo-cubic [001] direction) of the growth axis. Our findings include: (i) an original temperature-versus-growth angle phase diagram possessing different structural states, (ii) a tuning of the Curie temperature, T_c, by more than 450K, (iii) a minimal value of T_c being *near room temperature*, (iv) optimization of important physical responses at room temperature, such as dielectric and piezoelectric coefficients, for some specific growth directions; (v) explanations of the origin of these features, including the finding of a simple law correlating T_c with the growth direction. Items (i) clearly shows that the alternative procedure equivalently offers a phase diagram possessing different structural states. Items (ii)-(v) demonstrate the advantages of our proposed method by offering a rather "continuous" tuning of T_c (including near room temperature) and other properties (e.g., substantial *room-temperature* dielectric and piezoelectric responses), which are obviously of technological

importance.

For the dynamical properties of electrical vortices in ferroelectric nanocomposites, our study shows that in addition to "usual" dielectric modes that are associated with the fluctuation of the electrical polarization, novel toroidic modes, resulting from the electric toroidal moment fluctuations, are also discovered in the THz regime. Some of these toroidic modes have the same dynamics as the dielectric modes because of the inherent connection between electric toroidal moment and individual electric dipoles. Strikingly, there is also one toroidic mode whose dynamical characteristics significantly differ from those of dielectric modes, and that softens via a square-root law when the temperature approaches T_t – implying that the toroidal moment is the right (static and dynamical) order parameter to characterize the formation of electric vortices. Our simulations further demonstrate that the dynamics of this toroidic mode originates from the fluctuation of the azimuthal component of electric dipoles. This toroidal mode can thus be thought as a pendulum associated with rotational displacements in contrast to classical springs that are associated with polarization dynamics.

For the coupled magnetic orders in perovskites, we show that there is indeed a "universal" law which has a quite simple analytic form that correlates explicitly coupled magnetic orders with the oxygen octahedral rotations. First-principles calculations confirm its validity for any tested structural paraelectric and even ferroelectric phase, and for any chosen direction of any selected predominant magnetic vector. As what is predicted by our proposed law, (i) when anti-phase oxygen octahedral tiltings only exist, a magnetization can be generated through its spin canting by a predominant G-type AFM structure and may be maximized if the predominant G-type AFM vector is perpendicular to the oxygen tiltings and vice versa; and for a given G vector, the magnitude of the magnetization should be directly proportional to the magnitude of the anti-phase tilting angle; (ii) when there is only in-phase oxygen octahedral tiltings, a magnetization can be also created by a predominant C-type AFM structure and may be maximized if the predominant C-type AFM vector is perpendicular to the oxygen tiltings and vice versa; (iii) when only both anti-phase and in-phase oxygen octahedral tiltings exist, there is a possibility that A-type, C-type, F-type and G-type magnetic orders can coexist in a structure and their corresponding vectors lie along the directions imposed by our proposed universal law; (iv) for

polar phase, the existence of the polarization has no effect on the directions of the coupled magnetic orders, but does weakly alter the strength of the interaction parameter K.

For the electronic properties of electrical vortices in ferroelectric nanocomposites, our calculations shows (i) undoubtedly that the original reason behind the reduction in critical voltage in I-V curves experimentally measured across electrical vortices is extrinsic in nature, (ii) an interesting electronic phenomena is further discovered and reported here, that is the temperature-driven transition from a type-I to type-II band alignment when electrical vortices form inside the nanocomposite, which has its potential in designing novel electronic devices, exploiting the advantage of both types of alignments.

Bibliography

[1] J. F. Scott, *Annu. Rev. Mater. Sci.* **28**, 79 (1998).

[2] D. Dimos and C. H. Mueller, *Annu. Rev. Mater. Sci.* **28**, 397 (1998).

[3] W. Zhong, D. Vanderbilt and K. M. Rabe, *Phys. Rev. Lett* **73**, 1861 (1994); *Phys. Rev. B* **52**, 6301-6312 (1995).

[4] L. Walizer, S. Lisenkov and L. Bellaiche, *Phys. Rev. B* **73**, 144105–144111 (2006).

[5] Igor A. Kornev, L. Bellaiche, P.-E. Janolin, B. Dkhil and E. Suard, *Phys. Rev. Lett* **97**, 157601 (2006).

[6] Igor A. Kornev, S. Lisenkov, R. Haumont, B. Dkhil and L. Bellaiche, *Phys. Rev. Lett* **99**, 227602 (2007).

[7] H. Fu and L. Bellaiche, *Phys. Rev. Lett* **91**, 257601 (2003).

[8] S. Prosandeev, and L. Bellaiche, *Phys. Rev. Lett* **97**, 167601 (2006).

[9] W. Ren and L. Bellaiche, *Phys. Rev. B* **82**, 113403 (2010); *Phys. Rev. Lett* **107**, 127202 (2011).

[10] I. Ponomareva and L. Bellaiche, *Phys. Rev. Lett* **101**, 197602 (2008).

[11] A. Garca and D. Vanderbilt, *Appl. Phys. Lett.* **72**, 2981 (1998).

[12] K. M. Rabe and E. Cockayne, "in First-Principles Calculations for Ferroelectrics: Fifth Williamsburg Workshop", edited by R. E. Cohen (AIP, Woodbury, New York, 1998), p. 61.

[13] L. Bellaiche, Alberto Garcia, and David Vanderbilt, *Phys. Rev. Lett* **84**, 5427 (2000).

[14] J. C. Slater, *Phys. Rev.* **34**, 1293 (1929).

[15] P. Hohenberg and W. Kohn, *Phys. Rev.* **136** B864 (1964).

[16] W. Kohn and L. Sham, *Phys. Rev.* **140** A1133 (1965).

[17] L. Hedin and B. I. Lundqvist, *J. Phys. C* **4**, 2064 (1971).

[18] J. P. Perdew and A. Zunger, *Phys. Rev. B* **23**, 5048 (1981).

[19] D. M. Ceperley and B. J. Alder, *Phys. Rev. Lett* **45**, 566 (1980).

[20] A. D. Becke, *Phys. Rev. A* **38**, 1098 (1988).

[21] J. P. Perdew and K. Burke, *Int. J. Quant. Chem* **57**, 181 (1996).

[22] J. P. Perdew and Y. Wang, *Phys. Rev. B* **33**, 8800 (1986).

[23] J. P. Perdew, K. Burke, and M. Ernzerhof, *Phys. Rev. Lett* **77**, 3865 (1996).

[24] A. D. Beche, *J. Chem. Phys* **98**, 1372 (1993); *J. Chem. Phys* **98**, 5648 (1993).

[25] J. P. Perdew, M. Ernzerhof, and K. Burke, *J. Chem. Phys* **105**, 9982 (1996).

[26] V. I. Anisimov, J. Zaanen, O. K. Andersen, *Phys. Rev. B* **44**, 943 (1991).

[27] V. I. Anisimov, I. V. Solovyev, M. A. Korotin, M. T. Czyzyk, G. A. Sawatzky, *Phys. Rev. B* **48**, 16929 (1993).

[28] A. I. Liechtenstein, V. I. Anisimov, J. Zaanen, *Phys. Rev. B* **52**, R5467 (1995).

[29] V. I. Anisimov, F. Aryasetiawan, A. I. Lichtenstein, *J. Phys.: Condens. Matter* **9**, 767 (1997).

[30] U. von Barth and L. Hedin, *J. Phys. C: Solid State Phys.* **5**, 1629 (1972).

[31] Elisabeth Sjöstedt and Lars Nordström, *Phys. Rev. B* **66**, 014447 (2002).

[32] Warren E. Pickett, *Computer Physics Reports* **9**, 115-197 (1989).

[33] N. A. Pertsev, A. G. Zembilgotov, and A. K. Tagantsev, *Phys. Rev. Lett* **80**, 1988 (1998).

[34] Y. Yoneda, T. Okabe, K. Sakaue, and H. Terauchi, *Appl. Phys.* **83**, 2458 (1998).

[35] C. H. Ahn, K. M. Rabe, and J.-M. Triscone, *Science* **303**, 488 (2004).

[36] O. Dieguez *et al.*, *Phys. Rev. B* **69**, 212101 (2004).

[37] B.-K. Lai, I. Kornev, L. Bellaiche, and G. Salamo, *Appl. Phys. Lett.* **86**, 132904 (2005).

[38] I. B. Misirlioglu, S. P. Alpay, F. He, and B. O. Wells, *J. Appl. Phys.* **99**, 104103 (2006).

[39] S. Bin-Omran, I. Ponomareva, and L. Bellaiche, *Phys. Rev. B* **77**, 144105 (2008).

[40] J. H. Haeni et al., *Nature (London)* **430**, 758-761 (2004).

[41] N. A. Pertsev, A. K. Tagantsev, and N. Setter, *Phys. Rev. B* **61**, 825(R) (2000).

[42] I. Ponomareva and L. Bellaiche, *Phys. Rev. B* **74**, 064102 (2006).

[43] R. Oja, K. Johnston, J. Frantti and R. M. Nieminen, *Phys. Rev. B* **78**, 094102 (2008).

[44] K. Sone et al, *Jpn. J. Appl. Phys.* **49**, 09MB03 (2010).

[45] G. Makov and M. C. Payne, *Phys. Rev. B* **51**, 4014 (1995).

[46] Zhigang Gui, S. Prosandeev and L. Bellaiche, *Phys. Rev. B* **84**, 214112 (2011).

[47] Zhigang Gui and L. Bellaiche, *Phys. Rev. B* **91**, 020102(R) (20015).

[48] O. Nakagawara, T. Shimuta, T. Makino, S. Arai, H. Tabata and T. Kawai, *Appl. Phys. Lett.* **77**, 3257 (2000).

[49] K. Johnston, X. Huang, J. B. Neaton and K. M. Rabe, *Phys. Rev. B* **71**, 100103(R) (2005).

[50] I. C. Infante, S. Lisenkov, B. Dupé, M. Bibes, S. Fusil, E. Jacquet, G. Geneste, S. Petit, A. Courtial, J. Juraszek, L. Bellaiche, A. Barthélémy, and B Dkhil, *Phys. Rev. Lett.* **105**, 057601 (2010).

[51] R. J. Zeches, M .D. Rossell, J. X. Zhang, A. J. Hatt, Q. He, C.-H. Yang, A. Kumar, C. H. Wang, A. Melville, C. Adamo, G. Sheng, Y.-H. Chu, J. F. Ihlefeld, R. Erni, C. Ederer, V. Gopalan, L. Q. Chen, D. G. Schlom, N. A. Spaldin, L. W. Martin and R. Ramesh, *Science* **326**, 977 (2009).

[52] A. D. Bruce, *Adv. Phys.* **29**, 111 (1980).

[53] Jorge Íñiguez and L. Bellaiche, *Phys. Rev. Lett* **87**, 095503 (2001).

[54] P.-E. Janolin *et al.*, *J. Phys.: Condens. Matter* **26**, 292201 (2014).

[55] B. L. Liang, Z. Wang, Y. Mazur, V. V. Strelchuck, K Holmes, J. H. Lee and G. J. Salamo, *Nanotechnology* **17**, 2736 (2006).

[56] T. Shimizu, D. Suwama, H. Taniguchi, T. Taniyama and M. Itoh, *J. Phys.: Condens. Matter* **25** 132001 (2013).

[57] J. Weerasinghe, D. Wang and L. Bellaiche, *J. Phys.: Condens. Matter* **25**, 252202 (2013).

[58] L. Bellaiche, A. Garcia and D. Vanderbilt, *Ferroelectrics*, **266**, 41-56 (2002).

[59] I. I. Naumov, L. Bellaiche, and H. Fu, *Nature* **432**, 737–740 (2004).

[60] N. Balke *et al.*, *Nature Physics* **8**, 81–88 (2012).

[61] A. Gruverman, D. Wu, H.-J. Fan, I. Vrejoiu, M. Alexe, R. J. Harrison, and J. F. Scott, *J. Phys.: Condens. Matter* **20**, 342201 (2008).

[62] L. J. McGilly, A. Schilling and J. M. Gregg, *Nano Lett.* **10**, 4200 (2010).

[63] L. J. McGilly, and J. M. Gregg, *Nano Lett.* **11**, 4490 (2011).

[64] R. G. P. McQuaid, L. J. McGilly, P. Sharma, A. Gruverman and J. M. Gregg, *Nat. Comm.* **2**, 404 (2011).

[65] Y. Ivry, D. P. Chu, J. F. Scott and C. Durkan, *Phys. Rev. Lett.* **104**, 207602 (2010).

[66] N. Balke, S. Choudhury, S. Jesse, M. Huijben, Y. H. Chu, A. P. Baddorf, L. Q. Chen, R. Ramesh, and S. V. Kalinin, *Nat. Nanotechnol.* **4**, 868 (2009).

[67] C. L. Jia, K. W. Urban, M. Alexe, D. Hesse and I. Vrejoiu, *Science* **331**, 1420 (2011)

[68] C. T. Nelson *et al.*, *Nano Lett.* **11**, 828 (2011).

[69] R. K. Vasudevan *et al.*, *ACS Nano* **5**, 879 (2011).

[70] B. J. Rodriguez, X. S. Gao, L. F Liu, W Lee, I. I. Naumov, A. M. Bratkovsky, D. Hesse, M. Alexe, *Nano Lett.* **9**, 1127 (2009).

[71] L. Onsager, Statistical hydrodynamics. *Nuovo Cimento* **6** (Suppl. 2), 249 (1949).

[72] R. P. Feynman, Progress in Low Temperature Physics (ed. C. G. Gorter) **Vol. 1**, 17–51 (North-Holland, Amsterdam, 1955).

[73] A. Hubert, R. and Schäfer, Magnetic Domains (Springer, Berlin, 1998).

[74] T. Shinjo, T. Okuno, R. Hassdorf, K. Shigeto and T. Ono, *Science* **289**, 930–932 (2000).

[75] K. Y. Guslienko, B. A. Ivanov, V. Novosad, Y. Otani, H. Shima and K. Fukamichi, *J. Appl. Phys.* **91**, 8037–8039 (2002).

[76] S.-B. Choe, Y. Acremann, A. Scholl, A. Bauer, A. Doran, J. Stöhr, H. A. Padmore, *Science* **304**, 420–422 (2004).

[77] K. Yamada, S. Kasai, Y. Nakatani, K. Kobayashi, H. Kohno, A. Thiaville, and T. Ono, *Nature Materials* **6**, 270–273 (2007).

[78] K. Y. Guslienko, *J. Nanosci. Nanotech.* **8**, 2745–2760 (2008).

[79] I. Ponomareva, L. Bellaiche, T. Ostapchuk, J. Hlinka and J. Petzelt, *Phys. Rev. B* **77**, 012102 (2008).

[80] J. Hlinka, T. Ostapchuk, D. Nuzhnyy, J. Petzelt, P. Kuzel, C. Kadlec, P. Vanek, I. Ponomareva, and L. Bellaiche, *Phys. Rev. Lett.* **101**, 167402 (2008).

[81] J. F. Scott, *Rev. Mod. Phys.* **46**, 83 (1974).

[82] G. Shirane, *Rev. Mod. Phys.* **46**, 437 (1974).

[83] D. Rapaport, The Art of Molecular Dynamics Simulation (Cambridge University Press, Cambridge, 2001).

[84] M. E. Tuckerman, Yi Liu, G. Ciccotti, and G. J. Martyna, *J. Chem. Phys.* **116**, 1678 (2001).

[85] L. Louis, I. Kornev, G. Geneste, B. Dkhil and L. Bellaiche, *J. Phys. Cond. Mat.* **24**, 402201 (2012).

[86] V. M. Dubovik and V. V. Tugushev, *Physics Reports* **187**, 145–202 (1990).

[87] J. Caillol, D. Levesque and J. Weis, *J. Chem. Phys.* **85**, 6645 (1986).

[88] D. Wang, J. Weerasinghe and L. Bellaiche, *Phys. Rev. B* **83**, 020301(R) (2011).

[89] S. Prosandeev, I. Ponomareva, I. Kornev, I. Naumov and L. Bellaiche, *Phys. Rev. Lett.* **96**, 237601 (2006).

[90] I. I. Naumov and H. Fu, *Phys. Rev. Lett.* **101**, 197601 (2008).

[91] J. Wang and M. Kamlah, *Phys. Rev. B* **80**, 012101 (2009).

[92] Zhigang Gui and L. Bellaiche, *Phy. Rev. B* **89**, 064303 (2014).

[93] R. Comes, M. Lambert and A. Guinier, *Solid State Commun.* **6**, 715 (1968).

[94] S. Prosandeev, A. R. Akbarzadeh and L. Bellaiche, *Phys. Rev. Lett.* **102**, 257601 (2009).

[95] D. Sando *et al.*, *Nature Materials* **12**, 641–646 (2013).

[96] G. Catalan and J. F. Scott, *Adv. Mater.* **209**, 1 (2009).

[97] O. Auciello, J. F. Scott, and R. Ramesh, *Phys. Today* **51**, No. 7, 22 (1998).

[98] M. E. Lines and A. M. Glass, *Principles and Applications of Ferroelectrics and Related Materials* (Clarendon Press, Oxford, 1977).

[99] S.-W. Cheong and M. Mostovoy, *Nature Materials* **6**, 13 (2007).

[100] R. Ramesh and N. A. Spaldin, *Nature Materials* **6**, 21 (2007).

[101] B. Keimer, *Nature Materials* **5**, 9333 (2006).

[102] R. J. Cava *et al*, *Nature* **332**, 814 (1998).

[103] H. Béa *et al*, *Appl. Phys. Lett.* **87**, 072508 (2005); H. Béa *et al*, *Philos. Mag. Lett.* **87**, 165 (2007).

[104] C. Ederer and N. A. Spaldin, *Phys. Rev. B* **71**, 060401 (2005).

[105] D. Albrecht, S. Lisenkov, Wei Ren, D. Rahmedov, Igor A. Kornev and L. Bellaiche, *Phys. Rev. B* **81**, 140401(R) (2010).

[106] B. Dupé, S. Prosandeev, G. Geneste, B. Dkhil, and L. Bellaiche, *Phys. Rev. Lett.* **106**, 237601 (2011).

[107] D. Wardecki *et al*, *J. Phys. Soc. Jpn.* **77**, 103709 (2008).

[108] E. O. Wollan and W. C. Koehler, *Phys. Rev.* **100**, 545 (1955).

[109] H. Lutgemeier, H. G. Bohn and M. Brajczewska, *J. Magn. Magn. Mater.* **21**, 289 (1980).

[110] V. P. Plakhty, Yu. P. Chernenkov and M. N. Bedrizova, *Solid State Commun.* **47**, 309 (1983).

[111] A. S. Moskvin and I. G. Bostrem, *Sov. Phys. -Solid State* **19**, 1532 (1977).

[112] E. Bousquet and N. Spaldin, *Phys. Rev. Lett.* **107**, 197603 (2011).

[113] F. Keffer, *Phys. Rev.* **126**, 896 (1962).

[114] A. S. Moskvin, *Sov. Phys. -Solid State* **12**, 2593 (1971).

[115] A. S. Moskvin, *J. Exp. Theor. Phys.* **104**, 913 (2007).

[116] I. Dzyaloshinsky, *J. Phys. Chem. Solids* **4**, 241 (1958).

[117] T. Moriya, *Phys. Rev. Letters* **4**, 228 (1960).

[118] A. M. Glazer, *Acta Crystallogr. Sect. A* **31**, 756 (1975).

[119] H. T. Stokes, E. H. Kisi, D. M. Hatch, and C. J. Howard, *Acta Cryst. B* **58**, 934 (2002); C. J. Howard and H. T. Stokes, *Acta Cryst. B* **54**, 782 (1998).

[120] G. Kresse and J. Hafner, *Phys. Rev. B* **47**, 558(R) (1993); G. Kresse and J. Furthmüller, *Phys. Rev. B* **54**, 11169 (1996).

[121] S. Lisenkov, Igor A. Kornev and L. Bellaiche, *Phys. Rev. B* **79**, 012101 (2009); *Phys. Rev. B* **79**, 219902(E) (2009).

[122] L. Bellaiche, Zhigang Gui and Igor A. Kornev, *J. Phys.: Condens. Matter* **24**, 312201 (2012).

[123] R. M. Hornreich, S. Shtrikmann, B. M. Wanklyn and I. Yaeger, *Phys. Rev. B* **13**, 4046 (1976).

[124] S. Venugopalan and M. M. Becker, *J. Chem. Phys.* **93**, 3833 (1990).

[125] J. Bartolomé *et al*, *Phys. Rev. B* **55**, 11432 (1997).

[126] H. Katsura, N. Nagaosa and A. V. Balatsky, *Phys. Rev. Lett.* **95**, 057205 (2005).

[127] R. de Souza and J. E. Moore, *Appl. Phys. Lett.* **92**, 022514 (2008).

[128] N. D. Mermin, *Rev. Mod. Phys.* **51**, 591648 (1979).

[129] U. Ruediger, J. Yu, S. Zhang, A. D. Kent, and S. S. P. Parkin, *Phys. Rev. Lett.* **80**, 5639 (1998).

[130] J. Seidel *et al.*, *Phys. Rev. Lett.* **105**, 197603 (2010).

[131] M. Grujicic, G. Cao, and R. Singh, *Appl. Surf. Sci.* **211**, 166-183 (2003).

[132] N. W. Aschcroft and N. D. Mermin, *Solid State Physics* (Philadelphia, PA: Saunders), page 600.

[133] E. Durgun, Ph. Ghosez, R. Shaltaf, X. Gonze, and J.-Y. Raty, *Phys. Rev. Lett.* **103**, 247601 (2009).

[134] G. Kresse and D. Joubert, *Phys. Rev. B* **59**, 1758 (1999).

[135] V. Stepkova, P. Marton, N. Setter, and J. Hlinka, *Phys. Rev. B* **89**, 060101(R) (2014).

[136] Zhigang Gui, Lin-Wang Wang, and L. Bellaiche, submitted to *Nano Letters*, 2015.

[137] Lin-Wang Wang, Zhengji Zhao and Juan Meza, *Phys. Rev. B* **77**, 165113 (2008).

[138] L. Bellaiche and D. Vanderbilt, *Phys. Rev. B* **61**, 7877 (2000).

[139] N. J. Ramer and A. M. Rappe, *J. Phys. Chem. Solids* **61**, 317 (2000).

[140] N. Choudhury, L. Walizer, S. Lisenkov and L. Bellaiche, *Nature* **470**, 513–517 (2011).

[141] S. Lisenkov and L. Bellaiche, *Phys. Rev. B* **76**, 020102(R)–020106 (2007).

[142] Q. Zhang and I. Ponomareva, *Phys. Rev. Lett.* **105**, 147602–147606 (2010).

[143] L. W. Wang, A. Zunger, *J. Chem. Phys.* **100**, 2394(1994).

[144] J. Ma, L. W. Wang, *Nano Lett.* (in press).

[145] B. Lee, L. W. Wang, *Appl. Phys. Lett.* **96**, 071903 (2010).

[146] S. Dag, S. Z. Wang, L. W. Wang, *Nano Lett.* **11**, 2348 (2011).

[147] J. Kang, J. Li, S.-S. Li, J.-B. Xia, L. W. Wang, *Nano Lett.* **13**, 5485 (2013).

[148] http://cmsn.lbl.gov/html/PEtot/PEtot.html

[149] Our LS3DF predictions for the value of the band gaps of ideal BTO and STO are similar to those obtained in previous computational works (see, e.g., Ref. [150] that provides an indirect band gap of 1.92 and 2.04 eV for paraelectric BTO and STO, respectively).

[150] S. Piskunov, E. Heifets, R. I. Eglitis and G. Borstel, *Comput. Mater. Sci.* **29**, 165 - 178 (2004).

[151] Edward T. Yu, James O. McCaldin, and Thomas C. McGill, *Solid State Physic* **46**, 1-146 (1992).

[152] Riccardo Rurali, *Rev. Mod. Phys.* **82**, 427 (2010).

[153] Fenggong Wang, Ilya Grinberg, and Andrew M. Rappe, *Appl. Phys. Lett.* **104**, 152903 (2014).

[154] Steven A. McDonald, Gerasimos Konstantatos, Shiguo Zhang, Paul W. Cyr, Ethan J. D. Klem, Larissa Levina and Edward H. Sargent, *Nature Materials* **4**, 138-142 (2005).

[155] K. van Benthem, C. Elsässer, R. H. French, *J. Appl. Phys.* **90**, 6156 (2001).

[156] S. H. Wemple, *Phys. Rev. B* **2**, 2679 (1970).

[157] Giancarlo Cappellini, Sophie Bouette-Russo, Bernard Amadon, Claudine Noguera, and Fabio Finocchi, *J. Phys. Cond. Mat.* **12**, 3671 (2000).

Appendix A

Permission to reuse published articles in dissertation

For articles in Chapters 3 and 4, American Physics Society copyright policies[1]:

1. As the author of an APS-published article, may I include my article or a portion of my article in my thesis or dissertation?

Yes, the author has the right to use the article or a portion of the article in a thesis or dissertation without requesting permission from APS, provided the bibliographic citation and the APS copyright credit line are given on the appropriate pages.

2. As the author of an APS-published article, may I give permission to a colleague or third party to republish all or part of the article in a print publication?

Yes, as the author you may grant permission to third parties to republish print versions of the article provided the APS-published version (e.g., the PDF from the online journal, or a copy of the article from the print journal) is not used for this purpose. The article may not be published in another journal, and the third party may not charge a fee. The appropriate bibliographic citation and notice of the APS copyright must be included.

[1] https://journals.aps.org/copyrightFAQ.html#thesis

For the article in Chapter 5, Institute of Physics copyright policies:

Permission to use a coauthored article in my doctoral dissertation

Permissions <permissions@iop.org> Tue, Feb 10, 2015 at 6:02 PM
To: Zhigang Gui

Dear Zhigang Gui

Thank you for your email and for taking the time to seek this permission

When you assigned the copyright in your article to IOP we granted back to you certain rights including the right to include the article within any thesis or dissertation

Therefore please go ahead and make what use you wish of the content of the article

The only restriction is that if at a later date your thesis were to be published commercially further permission would be required

Please let me know if you have any further questions

In the meantime I wish you the best of luck with the completion of your dissertation

Kind regards

Lucy Evans

Publishing Assistant

IOP Publishing

Please note: We do not usually provide signed permission forms as a separate attachment Please print this email and provide it to your publisher as proof of permission

From: Zhigang Gui
To: permissions@iop.org
Date: 9 :
Subject: Permission to use a coauthored article in my doctoral dissertation

[Quoted text hidden]

For the article in Chapter 6, American Chemical Society copyright policies[2]:

The following wording is from the ACS Thesis/Dissertation Policy and the ACS Journal Publishing Agreement: Reuse/Republication of the Entire Work in Theses or Collections: Authors may reuse all or part of the Submitted, Accepted or Published Work in a thesis or dissertation that the author writes and is required to submit to satisfy the criteria of degree-granting institutions. Such reuse is permitted subject to the ACS Ethical Guidelines to Publication of Chemical Research (http://pubs.acs.org/page/policy/ethics/index.html); the author should secure written confirmation (via letter or email) from the respective ACS journal editor(s) to avoid potential conflicts with journal prior publication*/embargo policies. Appropriate citation of the Published Work must be made**. If the thesis or dissertation to be published is in electronic format, a direct link to the Published Work must also be included using the ACS Articles on Request author-directed link.

* Prior publication policies of ACS journals are posted on the ACS website.

** Reprinted with permission from [COMPLETE REFERENCE CITATION]. Copyright [YEAR] American Chemical Society. Insert the appropriate wording in place of the capitalized words. This credit line wording should appear on the first page of your ACS journal article.

[2]http://pubs.acs.org/page/copyright/permissions otherpub.html